

FY20 JRT FINAL REPORT / DIII-D MILESTONE 2020-3 REPORT CONTENT

By

**JRT team: N. Howard, T. Abrams, F. Scotti, B. Grierson,
A. Jaërvinen, T. Odstrcil, F. Sciortino, W. Guttenfelder, B. Victor,
S. Haskey, J. Nichols, S. Zamperini, A. Bortolon, F. Effenberg**

This is a preprint of a paper to be submitted to *DOE FES*, and possibly published online.

**Massachusetts Institute of Technology (MIT)*

This material is based upon work supported by the U.S. Department of Energy, Office of Science, Office of Fusion Energy Sciences, using the DIII-D National Fusion Facility, a DOE Office of Science user facility, under Award(s) DE-FC02-04ER54698.

DISCLAIMER

This report was prepared as an account of work sponsored by an agency of the United States Government. Neither the United States Government nor any agency thereof, nor any of their employees, makes any warranty, express or implied, or assumes any legal liability or responsibility for the accuracy, completeness, or usefulness of any information, apparatus, product, or process disclosed, or represents that its use would not infringe privately owned rights. Reference herein to any specific commercial product, process, or service by trade name, trademark, manufacturer, or otherwise, does not necessarily constitute or imply its endorsement, recommendation, or favoring by the United States Government or any agency thereof. The views and opinions of authors expressed herein do not necessarily state or reflect those of the United States Government or any agency thereof.

**GENERAL ATOMICS PROJECT 30200
OCTOBER 2020**

DIII-D Milestone 2020-3 : Test Impurity Transport Models and Control Solutions in Reactor Relevant Plasma Conditions

N. Howard¹, T. Abrams², C. Samuell³, B. Grierson⁴, F. Scotti³, A. Jarvinen³, T. Odstrcil², F. Sciortino¹, W. Guttenfelder⁴, R.E. Bell⁴, B. Victor³, S. Haskey⁴, J. Nichols⁵, S. Zamperini⁵, A. Bortolon⁴, F. Effenberg⁴

¹MIT Plasma Science and Fusion Center, Cambridge, Massachusetts, USA

²General Atomics, San Diego, California, USA

³Lawrence Livermore National Lab, Livermore, California, USA

⁴Princeton Plasma Physics Lab, Princeton, New Jersey, USA

⁵University of Tennessee - Knoxville, Knoxville, Tennessee, U

Milestone Statement

Accumulation of impurities, ranging from light ions (helium ash) to high-Z (such as tungsten) can adversely impact the reactivity of the fusion core through fuel dilution and excessive radiation. To inform the operation of ITER and beyond, DIII-D will study the transport and accumulation of impurities from the divertor to the core in regimes relevant to ITER and steady-state reactor operation. Work will employ the new DIII-D laser blow-off system and flexible impurity delivery to introduce a wide range of low to high Z impurities into reactor-relevant plasma conditions. Impurity profile evolution will be tracked using the full suite of DIII-D spectroscopic measurements. DIII-D's flexible heating systems will be leveraged to probe mechanisms of impurity control in ELMy and ELM-suppressed scenarios such as the ITER Baseline, QH-mode and advanced tokamak configurations. The dependence of divertor screening on SOL flows and closure will also be tested, exploiting visible/UV/VUV spectroscopy, 2D coherence imaging and reciprocating and collector probes. Cutting-edge statistical methods, comprehensive DIII-D fluctuation diagnostics, and integrated modeling tools will be used to validate the theoretical models implemented in NEO, TGLF and (C)GYRO and interpret physical mechanisms of transport in the core. Modeling using Monte Carlo transport for neutrals and 2D fluid equations for ions will be used to determine divertor and SOL impurity transport. Completion of this milestone will advance our understanding of impurity transport mechanisms, assess methods of impurity control, and help understand the potential impacts on reactor performance.

Table of Contents

Milestone Summary	3
Section 1. Introduction	4
Section 2. Core Impurity Transport	6
Section 3. Pedestal Impurity Transport	33
Section 4. Edge/Divertor Sourcing and Impurity Transport	43

Summary of Milestone Results

The DIII-D milestone 2020-3 made significant progress in advancing our understanding of impurity transport of low, mid, and high-Z impurities in the core region of tokamak plasmas. Core impurity transport data from DIII-D was used to provide insight into the neoclassical or turbulent nature of impurity transport in tokamaks spanning from the magnetic axis to the pedestal. A database of carbon profiles measured by charge exchange recombination spectroscopy were assembled that span a large part of the operational spaces of DIII-D. Additionally, the role of electron heating on core impurity accumulation was investigated for low, mid, and high-Z impurities in a range of DIII-D operational scenarios (inductive, hybrid, high qmin). All devices reported that near axis levels of impurity transport are in reasonable agreement with neoclassical expectations. This was determined through comparison of inferred transport coefficients and database trends with NEO simulations of impurity transport. Furthermore, application of a neoclassical pinch versus screening proxy, defined as $a/L_{n,D} - 0.5 a/L_{Ti}$ was found to be an effective indicator for the accumulation of impurities regardless of the impurity Z in all of the DIII-D operational regimes studied. This work indicates that carbon can be used as an effective proxy for the tendency of plasma conditions to experience impurity accumulation and that only a small amount of Electron Cyclotron Heating (ECH) heating is effective at reducing or eliminating impurity accumulation, a positive outcome as burning plasma conditions will be dominated by alpha particle generated electron heating. Outside of the deep core, the nature of the transport was often found to deviate from neoclassical expectations. A DIII-D database study was able to correlate the measured carbon profiles with a wide range of transport relevant parameters, providing insight into the nature of the transport. Transport at mid radius is clearly turbulent, with strong correlations observed with a/L_{ne} and a/L_{Ti} and only a weak dependence on collisionality. DIII-D results reveal a systematic discrepancy between gyrokinetic modeled and measured carbon profiles for conditions dominated by ITG turbulence. Explained previously by the possible role of rotodiffusive processes, the DIII-D beam co & counter capabilities have now allowed this possibility to be ruled out and the origin of this discrepancy remains an open question.

In pedestal impurity transport research we investigate the temporal dynamics of the inter-ELM particle transport for comparisons between DIII-D, NSTX and previous results from Alcator C-Mod pedestals [Rice 1997, Sunn Pedersen 2000]. On DIII-D, using direct measurements of the main-ions, in addition to the commonly measured electron and fully-stripped carbon densities, we have revealed the dynamic recovery and inter-ELM evolution which bears striking resemblance in many details observed in NSTX. Most notably, a phased onset of an inward impurity pinch that occurs early in the ELM cycle, and produces an edge-peaked impurity density profile. Values of an edge neoclassical inward impurity pinch exceeding 10 m/s are calculated and consistent with these and previous observations. In associated publications by contributors to this milestone, detailed study of the impurity transport found that the application of 3D fields (with or without complete ELM suppression) are consistently beneficial to impurity transport by increasing the impurity diffusion of high-Z impurities [Victor 2020] and increasing

helium exhaust [Hinson 2020]. These positive results are favorable for ensuring high plasma purity and fusion reactivity while mitigating ELMs.

Low-Z and high-Z SOL impurity transport studies on DIII-D utilize the DiMES and MiMES probe capabilities to rapidly change out collection witness samples during an experimental run day. This allows shot-by-shot resolved information on the evolution of impurity deposition/re-erosion to be obtained. Tungsten deposition profiles were measured on a Collector Probe (CP) located in the far-SOL near the outer midplane during W tracer experiments in DIII-D. Growth of boron layers in the far SOL region were observed via removable witness samples in the lower divertor on the DiMES probe. The empirical results from these experiments are used as input for state-of-the-art interpretive modeling tools in order to gain physics insight into the dominant physical processes regulating the transport and accumulation of high-Z and low-Z impurities in the SOL. High-Z deposition patterns in the far-SOL are reproduced by 3DLIM, a new 3D Monte Carlo far-SOL impurity transport code. Assuming purely diffusive radial transport ($10 \text{ m}^2/\text{s}$) results in the best agreement with experimental measurements of W deposition on the outer-target facing (OTF) sides of the CP. However, a purely convective radial transport model (125 m/s) is shown to have better agreement with the inner-target-facing (ITF) high-Z deposition profiles. Deposition profiles show peaking in W content along the length of the CP edges that is also reproduced in 3DLIM, but only when assuming a convection-dominated SOL plasma parallel transport prescription for the background plasma. The degree of the peaking is shown to be a secondary indicator of the effective location of the W source in the near-SOL. Detailed in-situ spectroscopic measurements of the re-deposition fraction of tungsten plasma-facing components were also performed. The W net erosion near the outer strike-point (OSP) is observed to be nearly equal to the gross erosion when the neutral W ionization length is large compared to the W gyro-radius and the width of the magnetic sheath. As the W ionization length decreases, the rate of tungsten net erosion also decreases relative to W gross erosion, with a strong inflection point when the W ionization length is several times the sheath width. These results were compared to two different analytic models, which assume that the W re-deposition physics is dominated by either the gyro-orbit trajectories of sputtered W ions or electrostatic forces within the magnetic pre-sheath. The measurements agree well with both models when the W ionization length is large relative to the sheath and W gyro-orbit length scales, but substantially more W net erosion is measured than predicted by the analytic models when the ionization length is small. This indicates that W re-deposition from charge states higher than W^+ are likely also important in regulating the balance between high-Z sourcing, leakage, and re-deposition. Low-Z powder injection in DIII-D plasmas at rates as low $1\text{-}5 \text{ mg/s}$ was observed to be sufficient to cause measurable changes in wall conditions, notably reducing the deuterium fueling from wall desorption. Growth of the boron layers in the far SOL region can be strongly affected by non-axisymmetric plasma footprint at the targets, resulting in striation patterns with alternating regions of erosion/deposition. The first 3D simulations of boron transport in the SOL with the EMC3-EIRENE code using a localized source of boron atoms show that the boron flux at the target can be toroidal asymmetric. However, the spatial scales are not compatible with the striations observed on DiMES, indicating that the latter cannot be ascribed to the source localization but are rather associated with uncompensated error fields. Parametric scans of

background plasma parameters indicate that plasma density plays an important role in determining the inboard-outboard asymmetry of the B fluxes to the targets. In particular, while low plasma density favors a more uniform distribution, high plasma density results in boron fluxes directed to the inner target. This difference appears to be primarily due to the role of the parallel friction force, which drags a greater fraction of B impurities to the high-field-side (inner target) at high plasma density. EMC3-EIRENE simulations also show that injection at high rates can perturb the background plasma fluid equilibrium, affecting SOL flows and consequently the spatial distribution of the boron flux at the targets.

Section 1. Introduction:

During the DIII-D Milestone, datasets were utilized to study the dynamics of impurity transport spanning from the deep core of fusion devices to the edge and divertor regions. This analysis allows us to better answer questions such as: What is the scaling of impurity transport with charge?, Is pedestal transport neoclassical or turbulent in nature?, and Do our divertor and core models contain sufficient physics to interpret existing experiments and ultimately predict future performance?

The research results are organized to present the study's conclusions moving from the plasma core to the edge and divertor region. This organization helps emphasize the similarities in the complementary datasets and points to robust conclusions about impurity transport using mature theory-based models and simulations. The very nature of D-T fusion necessitates an unavoidable core source of low-Z impurities (He-ash) to be present in any fusion device. Along with the mid and high-Z impurities, introduced deliberately or generated by plasma material interactions at the first wall and divertor, these impurities play a potentially dangerous role in affecting reactor power balance by reducing plasma performance through fuel dilution and radiative losses. Leading models of turbulent and neoclassical transport were validated during this study and were used to interpret a wide range of data spanning both large databases of impurity measurements and highly diagnosed individual discharges. Cross-machine impurity transport is predominately neoclassical in nature in the deep core, with turbulence playing a crucial role in the confinement and near-edge region. The results of experimental comparisons with models have also exposed some discrepancies that point to future work and potential model development.

The favorable energy confinement associated with H-mode operational regimes projected for fusion reactors, is often accompanied by correspondingly unfavorable impurity accumulation. Suppression of edge turbulence in the plasma pedestal region and the resulting extreme gradient scale lengths drives neoclassical transport that can result in strong inward convection of impurities. Detailed experiments that leveraged the main ion charge exchange capabilities on

DIII-D and STRAHL modeling were used to understand the dynamics of pedestal formation and the role that impurities play. These results are found to be largely consistent with similar work from NSTX, further displaying unifying features of impurity transport across distinctly different fusion devices.

In many ways the plasma edge represents the greatest opportunity to address impurity accumulation in the core. Interaction of energetic plasma with material surfaces occurs with the first wall and divertor region leading to erosion of mid and high-Z materials, and low-Z impurities are often seeded in the divertor in order to manage heat loads. Both of these events lead to the eventual introduction of low, mid and high-Z materials into the main plasma. To provide improved insight into the generation of impurities as well as their transport to the closed flux surfaces, research focused on the identification of potential impurity sources, erosion and deposition of materials in the divertor, and the migration of impurities through the SOL. Using DIII-D data, new experimental measurements in the divertor and SOL were used to validate models of PMI and SOL flows. Although in many cases less mature than the core transport models, comparison of new experimental evidence with these models represents an important step to the development of edge predictive models of impurity generation and transport.

Although historically each plasma region has been studied separately, the interconnected nature of impurity transport makes it an area where core/edge integration is necessary and where there is a clear path for future research. Successful operation of a burning plasma will require conditions that simultaneously balance the needs of power exhaust with a high performance pedestal and minimal core accumulation. Impurities play a crucial role in enabling and maintaining these conditions. The need for such integrated understanding motivated the US fusion community to advocate for the development of a New Tokamak User Facility (NTUF) for enabling exploration of innovative divertor concepts and demonstration of high performance core conditions with reactor-relevant edge conditions [CPP Report 2020]. Development of validated models in the core, pedestal, and the edge/divertor is the first piece of the puzzle. However, the ultimate goal of impurity transport is to couple validated models, enabling a simulation of the entire impurity chain from generation and sources at the edge to transport into and out of the deep core. The experimental data collected as part of the current JRT represents one the first attempts to gather the data that can enable a more holistic study of impurity transport and that will push us closer to the development of a core to edge predictive model of impurities in a tokamak.

Section 2. Core Impurity Transport:

Introduction

As the world fusion program pushes into an era of burning plasmas, the role of impurities in fusion reactors will be pushed to the forefront. Reactors based on the fusion of deuterium and tritium inevitably lead to the generation of impurities. The alpha particles created through D-T fusion reactions are simultaneously essential and determinantal the success of the fusion reactor. Extremely energetic fusion alphas need to be sufficiently confined such that they can transfer their energy to the bulk fusion plasma, allowing for the conditions needed for fusion to be sustained. However, after transferring their energy to the plasma, these alpha particles become He “ash”, which is unable to fuse and only serves to dilute the fusion fuel and reduce the overall performance of the device. It is essential that burning plasmas are able to expel this He-ash and it is therefore critical that we understand the nature of impurity transport to best inform the use of external actuators that produce impurity expulsion, and use this knowledge to create operational scenarios that have inherently good impurity confinement properties.

However, He-ash only represents one challenge of impurities in the core of fusion devices. Interaction of the confined plasma with the wall leads to erosion of wall materials and the generation of a range of mid and high-Z impurity species. These impurities can be transported from the edge to the core through a variety of transport mechanisms and unlike low-Z He-ash, can lead to issues beyond that of just fuel dilution. In addition to significant dilution, these impurities are efficient radiators at fusion relevant temperatures, leading to significant loss of energy from the plasma and degraded energy confinement. The heat exhaust challenge in future fusion devices will lead to another challenge with impurities, as it will likely be required to introduce low or medium-Z impurities in the divertor and main-chamber to reduce power loading to material surfaces. One unfortunate consequence of this is another source of impurities that can accumulate in the core, diluting the fuel and radiating energy. However, the introduction of low-Z impurities, when kept at sufficiently low levels, can also have benefits to energy confinement by stabilizing turbulence and reducing heat transport. The challenge is to find the appropriate balance.

These issues have motivated years of research into core impurity transport, where we seek both operational regimes and actuators that can reduce core impurity accumulation and to understand the physical mechanisms that are responsible for this accumulation. Significant progress has been made. Worldwide research has now established that core electron heating is an effective means to reduce accumulation of impurities in the core [Angioni2017], we have established a set of operational regimes that we believe display sufficient energy confinement and low enough impurity confinement to enable steady operation [Grierson2015][Petty2017][Nazikian2018], and we have validated [Angioni 2011] [Howard 2012] [Grierson 2015] and advanced or modeling capabilities to the point that we can now interpret

and even predict the behavior of core impurity transport in current, and even future devices. The work below addresses some of the outstanding questions in core impurities transport, providing valuable insight into the origins of impurity transport and pushing us closer to operational scenarios that we can extend to future burning plasmas.

Effect of rotation on low-Z (Carbon) impurities in DIII-D

Analysis Lead(s) : Tomas Odstrcil

Important conclusions from research in the effect of rotation on low-Z impurities on DIII-D include:

- A database of carbon profiles was assembled using > 150 DIII-D H-mode discharges that span the operational space of DIII-D H-modes
- Strong correlations of impurity peaking were found with a/L_{Ti} and a/L_{ne} . Weaker but non-negligible correlation was also observed with u' , Te/Ti and magnetic shear.
- Quasilinear modeling of the database was used to simulate the carbon peaking, revealing a systematic discrepancy between experimental and modeled a/L_{nC} in ITG dominated discharges. Thirteen nonlinear CGYRO simulations were performed that demonstrate that this discrepancy is not resolved by more comprehensive modeling.
- A detailed investigation of rotation scans suggests that the previous explanation for this discrepancy (rotodiffusion) [Angioni 2011][Casson 2013] does not apply to the DIII-D results; the theory/experiment discrepancy may be the result of overestimated pure pinch or underestimated thermodiffusive contributions to the impurity pinch.
- Since these terms exhibit a different ion charge dependence, a systematic study of this discrepancy for a wider range of impurities could be used to shed light on its origin.

Previous research on the ASDEX-Upgrade (AUG) [Angioni 2011][Casson 2013] and JET [Manas 2017] tokamaks demonstrated a small ($\Delta R/L_{nC} \sim 1$), but systematic discrepancy between the modeled zero-flux gradients of low-Z impurities and experimentally measured steady state gradient. These works proposed that this discrepancy is partially explained by rotodiffusion. Rotodiffusion is a part of the particle flux linearly proportional to the normalized rotation gradient of the impurity. Since this flux is outward in fast rotating ITG plasmas, it would tend to decrease the gyrokinetic zero flux gradient and thus reduce the discrepancy. The aim of this research was to use the unique capabilities provided by DIII-D's counter current neutral beam injection (NBI) to perform dedicated rotation scans capable of disentangling the effect of rotation on the impurity flux and as a result, more completely investigate this hypothesis.

An experimental database of H-mode discharges was assembled for the validation of multichannel transport in gyrokinetics codes over a large extent of the parameter space accessible by DIII-D tokamak. The database consists of discharges from campaigns between 2013 and 2019 after the upgrade of the high-resolution Thomson scattering (TS) system and the charge exchange recombination (CER) diagnostics to allow for the accurate determination

of the intrinsic carbon profiles. To ensure that high quality data is present in the database, we have included steady-state parts of the discharges, where the kinetic profiles and current profile show only a limited variation due to unavoidable ELM or sawtooth activity. To avoid issues in modeling or cases where 1D modeling is not applicable, we have excluded all discharges with a significant MHD activity or impurity contamination. Finally, since many discharges were very similar and clustered in a small volume of the parameter space, we have used the k-means clustering algorithm to identify these clusters and select ~ 150 representative points considered further for modeling.

Kinetic profiles for each of these cases were fit using Gaussian processes regression and the quality of each fit was assessed. The available profiles allowed us to draw out conclusions about the carbon profile peaking. The largest variation in R/L_n is found at $\rho = 0.3$ and spans a range between -4 and 5 . At $\rho = 0.6$ there is significantly smaller variation and R/L_n varies between -2 and 2.5 . Most analysis of this dataset was focused on $\rho=0.6$ due to the highest reliability of the measured carbon density gradients at this location. Correlations of the measured scale lengths with local plasma parameters are depicted in Fig. 2.3.1. The gradient is positively correlated with R/L_{n_e} and negatively with R/L_{T_i} , R/L_{T_e} , T_e/T_i and toroidal rotation of the plasma. However, all these parameters are also strongly mutually correlated and it is therefore difficult to identify the major parameters determining carbon gradient.

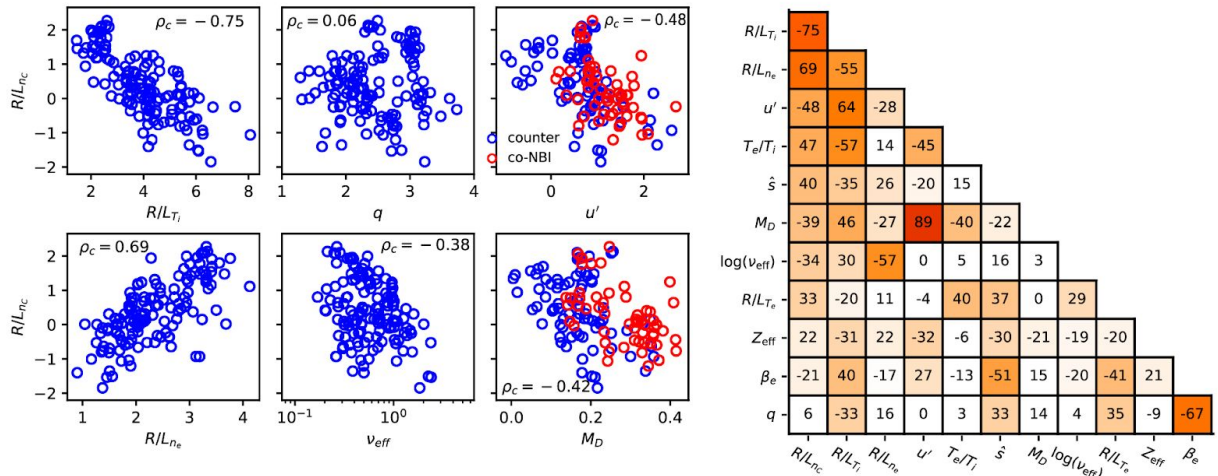


Figure 2.3.1. (Left) Measured carbon gradient scale lengths are plotted versus a potentially important local plasma parameters at $\rho = 0.6$. The correlation coefficients are shown in each panel. (Right) A correlation table is shown for all parameters considered in this analysis and color indicates absolute value of the correlation (with red representing the highest and white the lowest correlation values).

Power balance analysis using the TRANSP code was completed for the entire set of discharges in the database and linear gyrokinetic simulation was also performed using the CGYRO [Candy 2016] code.

As the primary objective of this work is to investigate the strong correlation between rotation and carbon density, reported in the previous studies on AUG and JET, the database was populated preferentially by discharges with counter-current NBI, which aim to decorrelate the relation between the input torque and NBI heating power and thus decorrelate the plasma rotation and ion temperature profile. The database includes several dedicated rotation scans that were investigated in more detail. A set of linear CGYRO simulations was used to perform quasilinear modeling of the entire database. The gyrokinetic impurity flux can be decomposed as:

$$\frac{R\Gamma_C}{n_C} = D_C \left(\frac{R}{L_{nC}} + C_T \frac{R}{L_{TC}} + C_u u'_C + C_p \right)$$

In this equation, first term in the brackets represent diffusive flux, the second term proportional to impurity temperature gradient R/L_{TC} is thermodiffusion, third term proportional to normalised rotation gradient of impurity $u'_C = R^2 \frac{\partial \omega}{\partial r} / v_{th,C}$ is rotodiffusion and the last is a pure pinch C_p . In steady state the carbon flux Γ_C is zero and R/L_{nC} approaches value when the diffusive flux is canceled by thermodiffusion, rotodiffusion and by pure pinch. However, neither in experiment, nor in CGYRO is it possible to vary rotation of one species independently of the others, therefore we will calculate a proxy for rotodiffusion as difference between carbon gradients with and without rotation.

$$C_u u'_C \approx \frac{R}{L_{nC}} - \frac{R}{L_{nC}} \Big|_{u'=0, M=0}$$

Results of the database modeling are summarized in Fig. 2.3.2. In this figure the impurity flux is broken into contributions from different pinch terms and plotted versus the real frequency of the most unstable linear model present at $k_{y,p_s}=0.3$. This poloidal wavenumber is generally near the peak in the spectrum of the long wavelength turbulence and is therefore considered a good proxy for the type of turbulence present. The convention is such that negative values of the real frequency indicate modes in the electron direction and will be classified as Trapped Electron Modes (TEM) whereas positive real frequency corresponds to modes in the ion direction and are therefore classified as Ion Temperature Gradient (ITG) driven modes. In Figure 2.3.2a & b, it is seen that a large inward pure pinch is nearly cancelled in ITG dominated plasmas ($\omega_r > 0$) by thermodiffusion of the same magnitude but opposite sign. In these conditions it might be expected that rotodiffusion should significantly affect carbon gradients although it is smaller than both of the other pinch terms. In Figure 2.3.2d, we see that the the experimental R/L_{nC} is found to be systematically below (less peaked or more hollow) the gyrokinetic model for ITG dominated cases. In contrast, TEM dominated conditions plasma exhibit good agreement between the simulated and measured impurity gradient scale lengths.

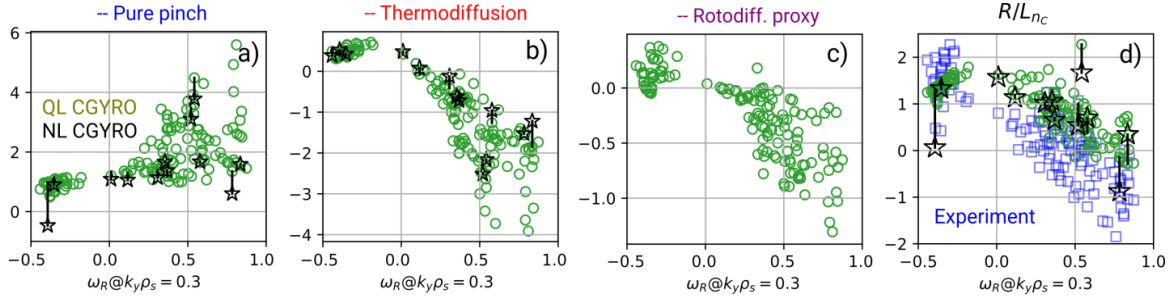


Figure 2.3.2. Quasilinear simulations (green open circles) are connected with associated nonlinear simulations (black open stars) by a black line and experimental data are plotted by blue squares. Carbon convection is decomposed in a pure pinch a), thermodiffusion b) and rotodiffusion c) estimated from a difference between simulation with and without rotation. The actual carbon density gradient is contrasted with modeling in d).

To examine whether the quasilinear approximation utilized in this work may be responsible for the disagreement in ITG dominated conditions, a series of nonlinear CGYRO simulations were performed. These simulations were performed with higher physics fidelity capturing plasma turbulence occurring at the ion-scale ($k_y \rho_s < 1.0$) using multiple impurity species (including trace carbon), collisions, ExB shear and rotation effects. A total of 13 nonlinear runs were performed that span the TEM and ITG range of plasmas covered by the database. As demonstrated in Figure 2.3.2a, b, & d., where nonlinear simulations are plotted using black stars and are connected to the corresponding quasilinear prediction with a line, nonlinear simulations do not appear to resolve the systematic disagreement and are found to generally produce similar impurity gradients to the quasilinear approximation which is significantly less computationally demanding.

The effect of rotodiffusion on the experimentally measured impurity gradients was more directly examined by focusing on analysis of 12 rotation scans identified in the database. The modeled contribution of rotodiffusion in these scans was generally found to be small and often within experimental uncertainties. Most promising results are identified in a high density phase of Super H-mode rotation scan shown in Fig. 2.3.3. These discharges are deep in the ITG regime (strongly positive real frequency in Figure 2.3.2.) and the carbon density profiles are significantly hollow and profile shape is fixed in the range of $\rho = 0.4 - 0.8$ as is illustrated by Fig. 2.3.3b. During this scan the rotation gradient increased from $u' = 0.5$ to 1.7 at $\rho = 0.6$ as shown in Fig. 2.3.3c. While the gyrokinetic zero flux gradient without rotation (red line) is nearly constant in the scan, outward rotodiffusion indicated by the blue line 6 reverses the sign of carbon convection and approaches experimental results. This significant dependence on rotation is a clear disagreement with experimental gradient (blank line in Fig. 2.3.3c) which remains constant.

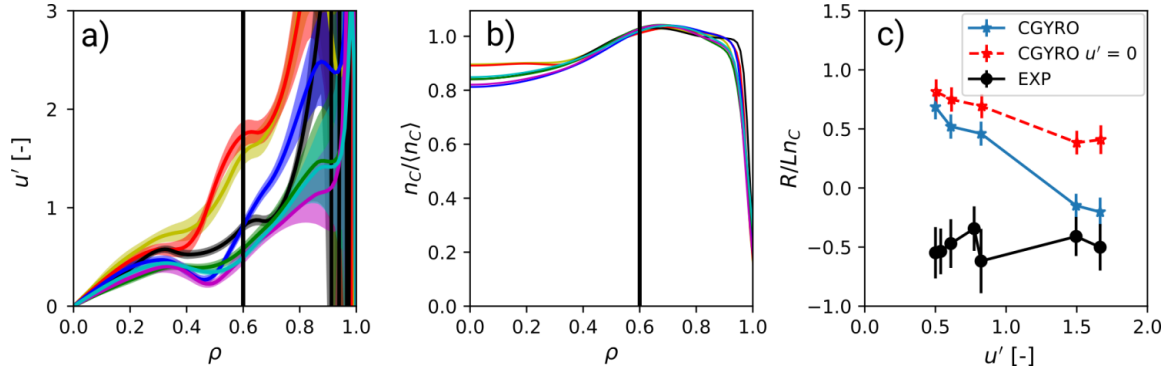


Figure 2.3.3 Rotation scan performed in Super H-mode scenario, where is a) normalized rotation gradient of deuterium, b) carbon density profile rescaled to the same average value c) experimental carbon gradient and modeled gradient with and without rotation evaluated at $\rho = 0.6$, indicated by black vertical lines in a) and b)

Results from all twelve rotation scans captured in the DIII-D database are shown in Fig. 2.3.4. Scans with $R/L_{n_c} > 0$ are in TEM regime or the weak ITG regime, while the scans with negative R/L_{n_c} are in ITG dominated plasmas. No systematic decrease of carbon density gradient with rotation is found in this database.

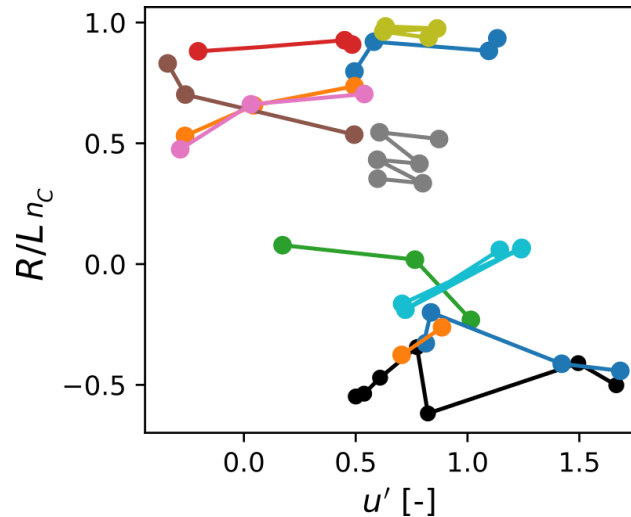


Figure 2.3.4 Carbon density gradient at $\rho = 0.65$ observed in 12 rotation scans as a function of normalized rotation gradient. Each individual scan is connected with lines.

In conclusion, DIII-D measurements confirmed the discrepancy in low-Z impurity gradients observed on JET and AUG. Systematic discrepancy is observed in all ITG dominated discharges that increases with mode frequency and for low rotating plasmas. In contrast to the ITG dominated conditions, TEM dominated conditions show good agreement between experiment and quasilinear & nonlinear CGYRO modeling. The discrepancy between the gyrokinetic model and experiment decreases at fast rotation due to a rotodiffusive contribution.

However, the analysis of the DIII-D database and the dedicated rotation scans captured within it, indicate a negligible role of rotation on the carbon density gradient, and a negligible role of rotodiffusion in contrast to previous explanations proposed on both ASDEX-Upgrade and JET. The discrepancy is therefore likely caused either by the underestimated contributions of thermodiffusion or to overestimated contributions from the pure pinch. Since these terms exhibit a different charge dependence, a systematic study of this discrepancy for a wider range of impurities could be used to shed light on the origin of this discrepancy.

Core Multi-Z Impurity Transport in Advanced Regimes with Varying ECH Deposition Location

Responsible individual(s): Brian Victor & Brian Grierson

Important conclusions from research on core multi-Z impurity transport are as follows:

- A common feature all plasma discharges studied (inductive, hybrid, high q_{min}) is that central deposition of additional electron heating is an effective means of controlling impurity accumulation across all studied impurities (C, Ar, W), which is positive for a fusion reactor dominated by electron heating by alpha particles
- Intrinsic carbon is found to be an effective proxy for the tendency of a plasma to experience impurity accumulation; if the carbon density profile displays significant peaking in the deep core, then higher-Z impurities will accumulate. However, intrinsic carbon cannot reveal the individual impurity transport coefficients that require non-perturbative impurity injections.
- A neoclassical impurity pinch vs. screening proxy defined as $a/L_{nD} - 0.5 a/L_{Ti}$ is an effective indicator for the tendency of impurities to accumulate in DIII-D as measured by impurity density and impurity radiation measurements. This indicates that the deep core of DIII-D plasmas is exhibiting impurity transport that is consistent with neoclassical mechanisms.
- Future experimental studies and modeling that include measurements of the turbulent transport in the deep plasma core near the magnetic axis will shed light on the type of fluctuations and transport mechanisms that produce the favorable impurity transport properties associated with electron heating

In a burning plasma such as ITER, the dominant source of heating will be fusion alpha particles that produce a peaked heating source near the magnetic axis and impart more power to the electrons than ions. In contrast to neutral beams, fusion alphas will not provide a particle source, but rather a sink to the fuel ions and source of impurity (helium) and therefore not contribute directly to electron or fuel ion density peaking. Neoclassical theory [Hirschman1981] predicts that in the presence of a main-ion density gradient exceeding half of the main-ion temperature gradient (when the neoclassical pinch/screening proxy = $a/L_{nD} - 0.5 a/L_{Ti}$, is positive), then impurity transport will be inward (pinch) rather than outward (screening). This condition is commonly encountered in the deep plasma core near the magnetic axis when

neutral beam heating is used. Therefore, studying scenarios where a significant fraction or majority of the heating is imparted to the electrons deep in the plasma core (such as RF heating) can provide reactor-relevant actuator experience, albeit in a regime with dissimilar absolute (i.e. temperature) and dimensionless (ν^* , ρ^* , β_e , etc...) parameters relevant to the radiative power losses and transport mechanisms, respectively. When projecting to ITER and other large reactors, it has been argued that a number of unfavorable observations in current tokamaks with high-Z PFCs [Neu 2014] will extrapolate favorably, easing concerns that detrimental high-Z impurity accumulation will occur [Angioni 2017]. First, at the reactor scale, the role of neoclassical impurity transport will be reduced due to the high ion temperature, high field and low toroidal rotation, and more likely to be dominated by turbulence that does not possess a strong inward impurity particle pinch. Second, the drive for the neoclassical inward pinch may be reduced when there is little or no central fueling and weak centrifugal enhancement. Third, the radiation cooling curve of high-Z impurities such as tungsten become decreasing functions of the electron temperature [Putterich2019]. Previous studies on Alcator C-Mod [Loarte 2015] using tungsten (W) laser blow-off (LBO) were executed in a regime that mimics those expected in ITER, namely ITER-like mid-radius density peaking, and ion cyclotron resonance heating (ICRH). The results from Alcator C-mod did not identify tungsten accumulation, and indicate that accumulation of tungsten in the central plasma region is also unlikely to occur in stationary ITER H-mode plasmas. Quasilinear modeling indicates that a turbulent pinch will increase the density peaking in ITER, but not lead to a strong impurity pinch [Grierson 2018], in agreement with the above considerations. Advanced confinement regimes, however, present possible differences with baseline scenarios, including operation at lower plasma current, higher beta, core magnetohydrodynamic instabilities such as neoclassical tearing modes, and with enhanced confinement regions or internal transport barriers that coincide with weak or reversed magnetic shear. High performance hybrid scenarios on JET that operate with a number of factors known to increase the tendency for impurity accumulation (high neutral beam power, central fueling and toroidal rotation) were well described by modeling that included the relevant physics [Angioni 2014]. In this section we will connect DIII-D experiments during the tungsten metal rings campaign (MRC) [Unterberg 2020] to observations on other devices and establish the phenomenology of high-Z impurity accumulation using DIII-D diagnostics. Next, we will investigate the impact of ECH and ECCD on hybrid scenario plasmas with argon injection to assess the role of electron heating and tearing mode activity on impurity transport. Finally, we will contrast two steady-state scenarios identified as steady-state hybrid and high q_{min} , with on and off-axis ECCD, respectively, with the strike point placed on tungsten in the divertor.

Impurity accumulation in an inductive scenario

Impurity experiments from the DIII-D metal rings campaign (MRC) were examined to determine the scaling trends of central tungsten accumulation with ECH power based on the neoclassical pinch/screening proxy $= a/L_{nD} - 0.5 a/L_{Ti}$, which is expected to produce a dominant impurity

pinch when positive. A sequence of discharges was executed beginning with NBI-only auxiliary heating, followed by increasing levels of ECH including on-axis ($\rho < 0.1$) heating. These experiments inform the dedicated experiments on DIII-D in the ITER baseline and steady-state scenarios with electron heating and current drive from ECH and ECCD. The NBI-only discharge investigated is shown in Figure 2.4.1. In this discharge, at 1900 ms the strike point is placed on the W ring and tungsten is sourced from the outer metal ring in the divertor. Between 1900-3850 ms, the emission of the 13 nm tungsten “clusters” indicate accumulation, until a partial radiative collapse at 3850 ms. Shown in the figure is a spectrum from the SPRED spectrometer in wavelength and time, as well as the evolution of the plasma profiles during tungsten accumulation. Prior to the partial radiative collapse, transport analysis using NEO [Belli 2008] reveals that inside of $\rho = 0.3$ the ion thermal transport is at the neoclassical level, and an inward impurity pinch is predicted.

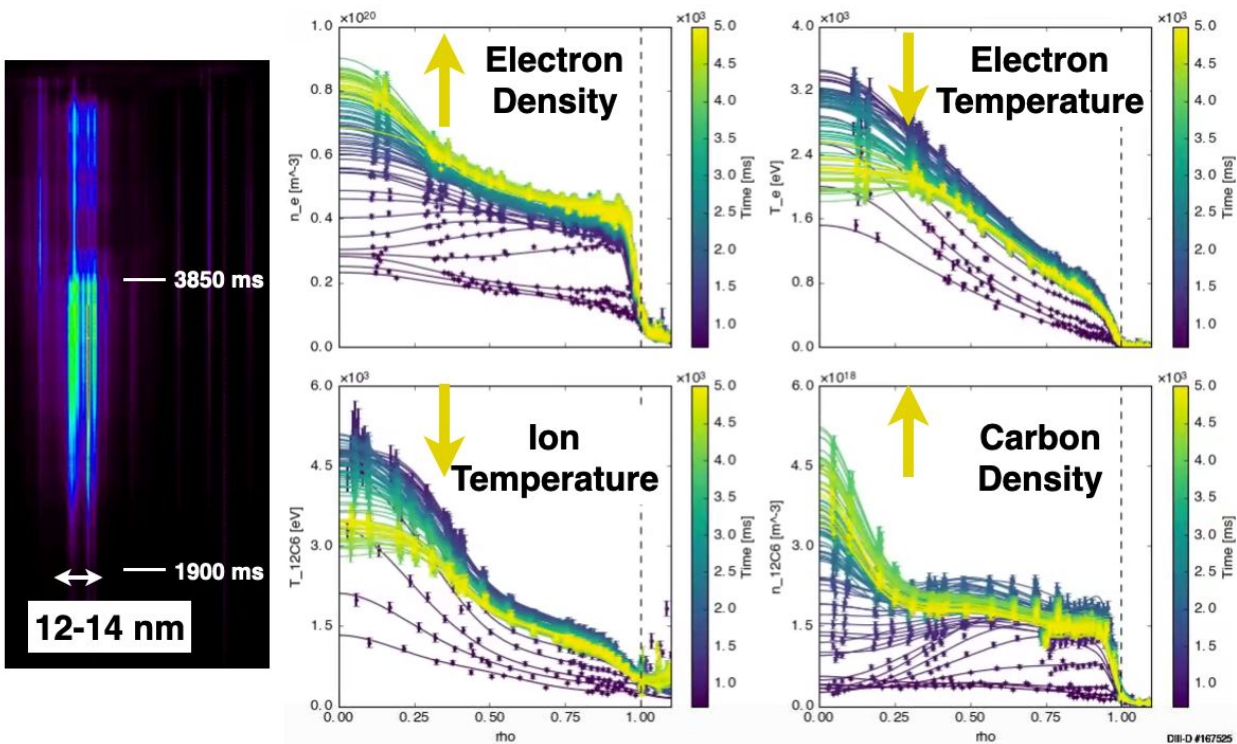


Fig. 2.4.1: (left) wavelength-time evolution of the ~ 13 nm “clusters” of tungsten emission from the SPRED spectrometer and (right) plasma profiles of n_e , T_e , T_i , and n_C . At 3850 ms the plasma undergoes a radiative collapse as the tungsten accumulates and cools the electron and ion temperatures.

Central ECH heating power was applied to this scenario in subsequent discharges using power steps of 1.1, 2.0, and 3.2 MW. By investigating the response of carbon, total radiated power and SXR emission, the response of the central impurity to ECH heating can be determined. In these cases, the central carbon density could be directly analyzed and a local gradient scale length at $\rho = 0.15$ formed as a/L_{nC} . For total radiation from bolometers and soft X-ray radiation, the ratio of a central to outer mid-radius channel was used. All accumulation indicators (a/L_{nC} , bolometer ratio and SXR ratio) are shown in Figure 2.4.2 We find that in general, accumulation

is occurring when the neoclassical proxy is more positive than 0.5, and that the use of even modest amounts of ECH (~ 1 MW) is effective at reducing or eliminating the impurity accumulation, reducing the radiation peaking to near unity.

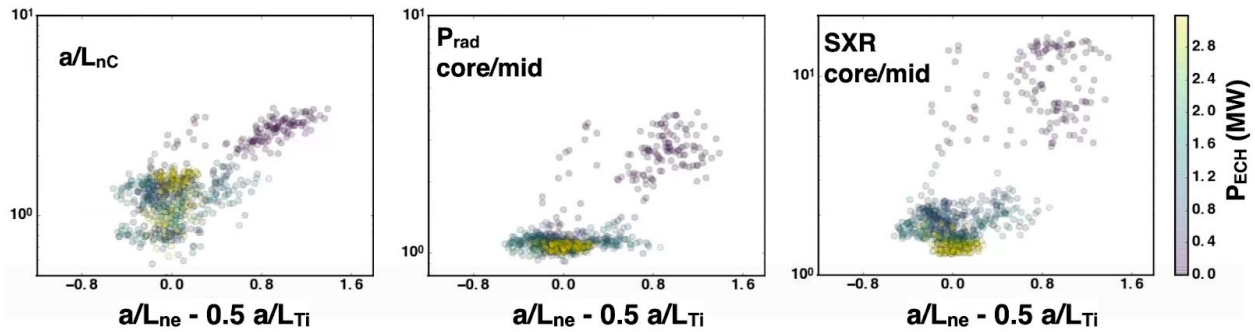


Fig. 2.4.2: (left) central carbon density inverse scale length a/L_{nC} . (middle) Ratio of central to outer bolometer channel. (right) Ratio of central to outer SXR channel. Data points are colored by ECH heating power.

These DIII-D H-mode scenarios confirm the need of using central ECRH to avoid central W accumulation, and even modest amounts of ECH ($P_{ECH}/P_{aux} \sim 0.2$) can be quite effective. The behaviors of intrinsic C and of W are similar, and are both consistent with neoclassical inward convection occurring in the deep core.

Impurity transport in hybrid scenario with ECH and ECCD

One potentially attractive operating regime is the hybrid scenario [Luce 2001, Wade 2001, Luce 2014], which is a stationary high confinement regime between the inductive baseline and steady state scenario. Operation in the hybrid regime benefits from achieving elevated confinement at high beta, while operating at reduced current and elevated safety factor to lower the risk from high current disruptions. Hybrid operation is typically accompanied by a lack of the central sawtooth oscillation which is beneficial to avoiding sawtooth-triggered $m/n=2/1$ tearing modes and disruptions, but possesses some other core MHD, such as a common $m/n=3/2$ NTM that can be controlled with ECCD, or fishbones. On DIII-D, JET and other devices the hybrid scenario is typically accessed through the use of high-power neutral beam injection to reach high beta. High power neutral beam injection is accompanied by both high T_i/T_e and high toroidal rotation and $\mathbf{E} \times \mathbf{B}$ shear, both of which are expected to reduce when moving to a reactor.

In order to study the effect of electron and ion heating on impurity transport in the hybrid regime a series of discharges were executed with short puffs of argon gas in order to observe the impurity transport characteristics by varying the radial profile of electron heating and type of core MHD present. A target NBI-only hybrid discharge with a core $m/n=3/2$ tearing mode was established at $q_{95} \sim 5$, $\beta_N \sim 3$, $H_{98(y,2)} \sim 1.5$ with $P_{NBI} \sim 6$ MW. This target discharge had a short 10 ms argon gas puff to assess the uptake and exhaust of the impurity, shown in Figure 2.4.3 This

discharge experienced the onset of a 2/1 tearing mode shortly after the impurity injection (~3200 ms), which has been seen to occur in neutral beam dominated hybrid plasmas [Petrie 2019], but the profiles and radiation prior to the mode onset is useful for comparison to the other conditions. The next two discharges for comparison use ECCD to suppress the 3/2 tearing mode and more central ECH to increase T_e/T_i . ECCD is used near the 3/2 rational surface to suppress the 3/2 tearing mode and results in a weaker 4/3 mode. From the plasma profile shapes and time evolution of the argon induced SXR emission a number of conclusions can be drawn. The NBI-only and ECCD hybrids possess the common features of more peaked central electron and impurity density, and longest impurity confinement. By fitting the plasma profiles and investigating the gradient scale lengths, we can see that the NBI-only discharge has both modest central density and temperature gradients, and evaluation of the neoclassical peaking proxy is positive and prone to accumulation. The discharge with ECCD has a noticeably peaked electron density profile and modest temperature peaking, and also evaluates to a positive peaking proxy and inward pinch. The discharge with central ECH has the weakest central density peaking, and produces a negative peaking proxy. Inspection of the carbon density profile is revealing, in that the conditions with positive peaking proxies (NBI, ECCD) possess modest or strongly peaked carbon densities, respectively. The condition with central ECH and a negative peaking proxy, possesses a hollow carbon density profile, consistent with neoclassical expectations. Similar observations were made in high beta hybrids with argon used for radiative divertor operation [Petrie 2019]. At the outer radii, additional thermal and momentum transport mechanisms are at play that show the impact of increased electron heating; namely the higher T_e/T_i is associated with both a flattening of the ion temperature profile, and reduction of the plasma angular momentum, which are both consistent with destabilization of ITG that enhances the ion heat and momentum transport through a reduction in the linear critical gradient. The response of the argon emission to these considerations is also quite revealing and consistent with the conclusions drawn from the carbon profiles, but with additional insights. By viewing the central SXR emission in Figure 2.4.3 we see that the uptake of the impurity density in the ECCD and ECH discharges is rapid (~100 ms), indicating that a higher level of impurity particle diffusivity exists in the outer region of these plasmas compared to the NBI-only conditions (~300 ms, black). Beyond the peak of emission, both the NBI-only and ECCD discharges exhibit a slow decay, indicating that the impurity has accumulated in the central region. However, the ECH discharge exhibits a rapid impurity exhaust, displaying the benefit of high impurity diffusion across the plasma profile.

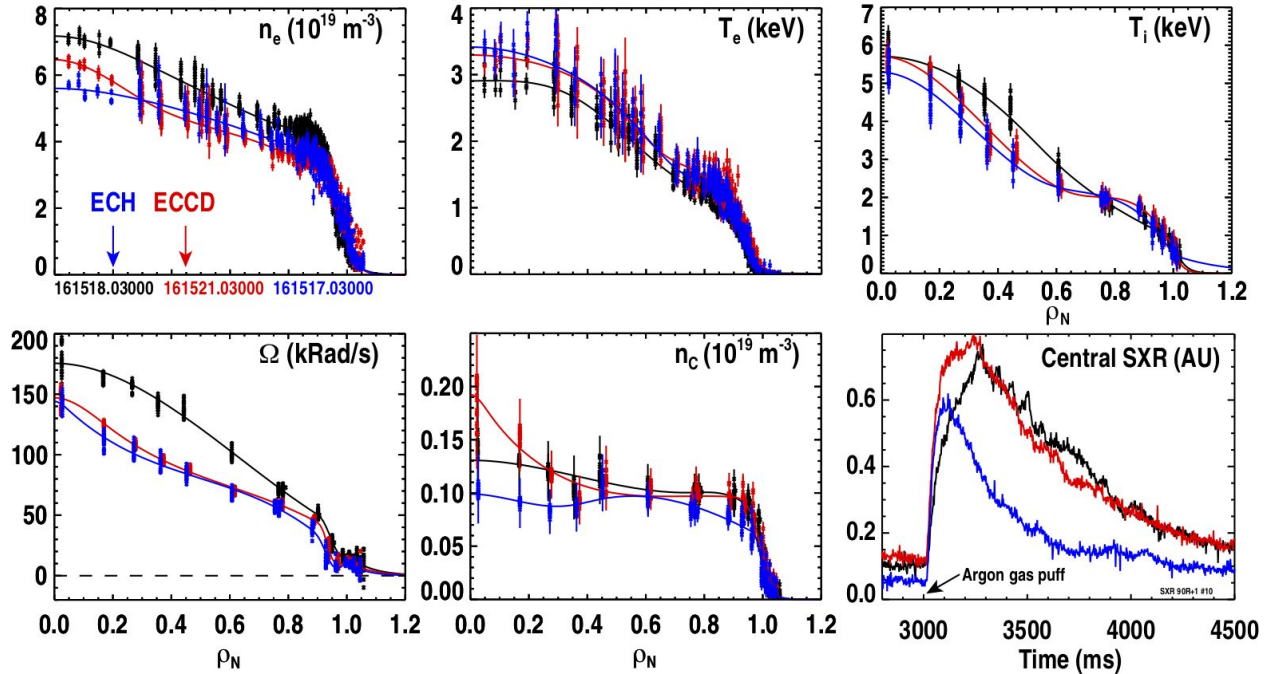


Fig. 2.4.3: Three hybrid discharges with NBI-only, additional 3.3 MW of off-axis ECCD aimed at 3/2 surface, or additional 3.3 MW of central ECH. Shown are electron density, electron temperature, ion temperature, toroidal rotation, impurity density and SXR emission during Ar injection.

Impurity transport in steady-state scenarios

Results from impurity transport studies in steady-state scenarios complete our study of multi-Z impurity transport in advanced regimes by returning to the DIII-D metal rings campaign, and investigating two candidate steady-state scenarios; steady-state hybrid, and high q_{\min} . Both conditions operate with the plasma configuration optimized for current drive, with reversed toroidal field and off-axis neutral beam injection. Both conditions use ECCD at an oblique angle, which provides both current drive and electron heating. The steady-state hybrid scenario [Petty 2016] is similar to the target hybrid plasma in the previous section, but operates with reduced plasma current, higher q_{95} , and central ECCD near the magnetic axis ($\rho \sim 0$). Central ECCD in the hybrid scenario maintains a broadened current profile and $q_{\min} \sim 1$ through anomalous current redistribution. The high q_{\min} scenario [Holcomb 2014] operates with off-axis ECCD ($\rho \sim 0.2-0.5$) to raise q_{\min} . Both discharges placed the strike point on the tungsten ring in the lower divertor to produce tungsten sourcing, and monitored the tungsten influx with SPRED, SXR and an x-ray and extreme ultraviolet spectrometer (XEUS) installed specifically for the metal rings campaign. Comparison of these two steady-state scenarios in the presence of tungsten revealed that only the hybrid scenario with central ECCD was able to avoid tungsten accumulation, and did not suffer any performance degradation in the presence of tungsten. In both the high q_{\min} scenario, and hybrid scenarios without ECCD, tungsten would accumulate and cause reductions of performance. Figure 2.4.4 reveals a number of telling indications that, similar to previous sections in this report, central electron heating is key to avoiding impurity accumulation. With

2.9 MW of central ECCD ($P_{EC}/P_{aux} \sim 0.3$) a clear enhancement to the central electron and ion temperature gradients and flattening of the near-axis electron density profile is observed; both conditions favor neoclassical screening. The tungsten emissivity in the steady-state hybrid plasma is broad and relatively low compared to the high q_{min} discharge and does not show strong accumulation. In the high q_{min} discharge with off-axis ECCD, both electron and ion temperature profiles are broad and flat in the central region, while the electron density profile is centrally peaked; both conditions favor neoclassical accumulation. The tungsten emissivity in the high q_{min} discharge is centrally peaked and a factor of ten higher than the steady-state hybrid plasma. It should be stressed that these observations do not render the high q_{min} scenario irrelevant for a steady-state fusion scenario, as any burning plasma will have strong central electron heating and weak near-axis fueling. There is no direct evidence that the current profile or elevated central safety factor in the high q_{min} scenario is contributing to the tungsten accumulation, as the neoclassical mechanism of inward impurity pinch may be dominating over other transport effects tied to the q -profile.

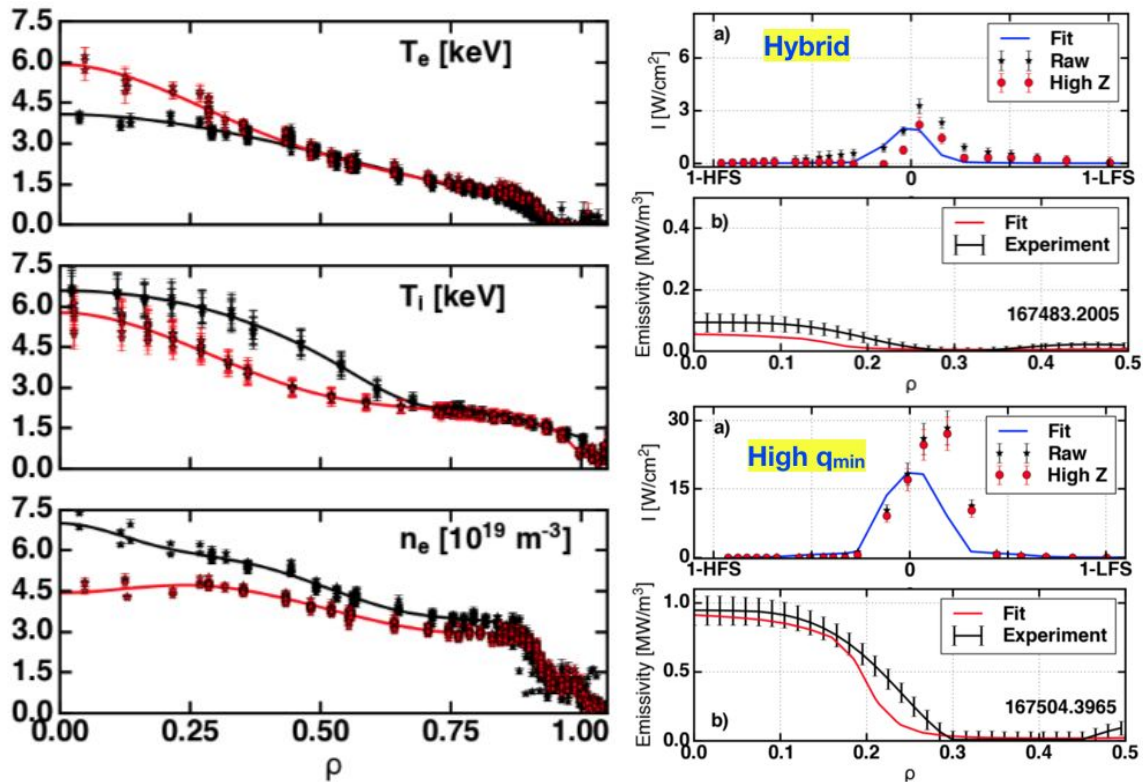


Fig. 2.4.4: Plasma profiles (left) for steady-state hybrid (red) with on-axis ECCD and high q_{min} (black) with off-axis ECCD. Tungsten emission (right) for steady-state hybrid (top) and high q_{min} (bottom) conditions showing ten times more tungsten emission in the high q_{min} scenario. Fit profiles used for inferring tungsten density from multiple diagnostics.

References for Section 2

Introduction

[Angioni 2017] C. Angioni *et al.* “A comparison of the impact of central ECRH and central ICRH on the tungsten behaviour in ASDEX Upgrade H-mode plasmas”, Nucl. Fusion 57 (2017) 056015

[Grierson 2015] B. Grierson *et al.* “Impurity confinement and transport in high confinement regimes without edge localized modes on DIII-D”, Physics of Plasmas 22, 055901 (2015)

[Petty 2017] C. Petty *et al.* “Advances in the steady-state hybrid regime in DIII-D—a fully non-inductive, ELM-suppressed scenario for ITER”, Nucl. Fusion 57 (2017) 116057

[Nazikian 2018] R. Nazikian *et al.* “Grassy-ELM regime with edge resonant magnetic perturbations in fully noninductive plasmas in the DIII-D tokamak”, Nucl. Fusion 58 (2018) 106010

[Angioni 2011] C. Angioni *et al.* “Gyrokinetic modelling of electron and boron density profiles of H-mode plasmas in ASDEX Upgrade” Nucl. Fusion **51**(2), 023006 (2011)

[Howard 2012] N. Howard *et al.* “Quantitative comparison of experimental impurity transport with nonlinear gyrokinetic simulation in an Alcator C-Mod L-mode plasma”, Nucl. Fusion **52**(6), 063002 (2012).

Effect of rotation on low-Z (Carbon) impurities in DIII-D

[Angioni 2011] C. Angioni *et al.* “Gyrokinetic modelling of electron and boron density profiles of H-mode plasmas in ASDEX Upgrade” Nucl. Fusion **51**(2), 023006 (2011)

[Casson 2013] F. Casson *et al.* “Validation of gyrokinetic modelling of light impurity transport including rotation in ASDEX Upgrade” Nucl. Fusion **53**(6), 063026 (2013)

[Manas 2017] P. Manas *et al.* “Gyrokinetic modeling of impurity peaking in JET H-mode plasmas” Phys. Plasmas **24**(6), 062511 (2017).

[Candy 2016] J. Candy *et al.* “A high-accuracy Eulerian gyrokinetic solver for collisional plasmas” J. Comput. Phys. **324**, 73 (2016)

Multi-Z with ECH

[Neu 2014] R.Neu et. al., “Experiences With Tungsten Plasma Facing Components in ASDEX Upgrade and JET” IEEE Trans. Plasma Sci., 42, 3, 522-562, 2014

[Angioni 2017] C. Angioni, et. al., “Gyrokinetic study of turbulent convection of heavy impurities in tokamak plasmas at comparable ion and electron heat fluxes”, Nucl. Fusion 57 022009, 2017

[Loarte 2015] A. Loarte, et. al., “Tungsten impurity transport experiments in Alcator C-Mod to address high priority research and development for ITERa)”, Phys. Plasma 22, 056117, 2015

[Grierson 2018] B. A. Grierson, et. al., “Multi-scale transport in the DIII-D ITER baseline scenario with direct electron heating and projection to ITER”, Phys. Plasmas 25, 022509, 2018

[Angioni 2014] C. Angioni, et. al., “Tungsten transport in JET H-mode plasmas in hybrid scenario, experimental observations and modelling”, Nucl. Fusion 54 083028, 2014

[Unterberg 2020] E.A. Unterberg, et. al., “Localized divertor leakage measurements using isotopic tungsten sources during edge-localized mode-y H-mode discharges on DIII-D”, Nucl. Fusion 60 016028, 2020

[Belli 2008] E A Belli and J Candy, “Kinetic calculation of neoclassical transport including self-consistent electron and impurity dynamics”, Plasma Phys. Control. Fusion 50 095010, 2008

[Luce 2001] T.C. Luce, et. al., “Long pulse high performance discharges in the DIII-D tokamak”, Nucl. Fusion 41 1585, 2001

[Wade 2001] M.R. Wade, et. al., “Progress toward long-pulse high-performance Advanced Tokamak discharges on the DIII-D tokamak”, Phys. Plasmas 8 2208, 2001

[Luce 2014] T.C. Luce et. al., “Development of advanced inductive scenarios for ITER” Nucl. Fusion 54 013015, 2014

[Petrie 2019] T.W. Petrie, et. al., “High performance double-null plasmas under radiating divertor and mantle scenarios on DIII-D”, Nucl. Fusion 59 086053, 2019

[Petty 2016] C.C. Petty, et. al., “High-beta, steady-state hybrid scenario on DIII-D”, Nucl. Fusion 56 016016, 2016

[Holcomb 2014] C.T. Holcomb, “Steady state scenario development with elevated minimum safety factor on DIII-D”, Nucl. Fusion 54 093009, 2014

Section 3. Pedestal Impurity Transport:

Introduction

Improved energy confinement in the H-mode, with a strong transport barrier and steep gradients at the plasma edge, is also associated with increased particle and impurity confinement. In the pedestal, edge localized modes (ELMs) act as both a pressure and particle relief valve to achieve stationary conditions, expelling both thermal energy and impurities that can improve the plasma purity. Time dependent measurements of the ELM event itself indicates that the ELM expels electrons, main-ions and impurities at similar rates [Wade 2005]. However, increasing the ELM frequency is well known to reduce the overall impurity concentration, which indicates the inter-ELM dynamics may be playing a role in determining the overall plasma purity. Due to the strong shear suppression of turbulence in the H-mode pedestal, ion and impurity transport may be reduced to neoclassical levels [Callen 2010, Kotschenreuther 2019]. Neoclassical theory [Hirshman 1981] predicts that in the presence of a main-ion density gradient exceeding half of the main-ion temperature gradient (when the neoclassical pinch/screening proxy $= a/L_{nD} - 0.5 a/L_{Ti}$, is positive), then impurity transport will be inward (pinch) rather than outward (screening). This condition is commonly encountered in the deep plasma core near the magnetic axis when neutral beam heating is used, and also commonly encountered in the H-mode pedestal. Operation in the L-mode and I-mode, which does not possess a density pedestal, broadly supports this physics principle [Rice 2015]. Previous work in H-mode on ASDEX-Upgrade [Putterich 2011] using trace multi-Z impurities indicates that the pedestal impurity pinch dominates over screening due to the strong density gradient, and largely follows the neoclassical expectations. However, the expectations in ITER of a relatively flat pedestal density gradient compared to temperature gradient due to the high neutral opacity of the ITER pedestal, indicate that ITER may be in a favorable regime that favors impurity screening [Dux 2014]. The nature of source vs. transport in determining the pedestal density profile was investigated in the 2019 JRT [Mordijck 2019]. It is noteworthy that operation with large natural type-I ELMs in H-mode will need to be avoided above a material limit for the ELM-induced heat flux. Previous studies in regimes devoid of ELMs such as QH-mode and RMP ELM-suppressed H-mode have demonstrated the applicability of these regimes to maintaining sufficiently low impurity confinement [Grierson 2015].

Recovery of the Main-ion and Impurity Density Profile Between ELMs

Analysis Lead(s): Brian Grierson and Shaun Haskey

Important conclusions from research on pedestal impurity transport during the 2020 JRT are as follows;

- Direct measurements of the main-ion, electron and impurity carbon density in low-frequency ELMy H-mode DIII-D pedestals reveal that a significant fraction of the inter-ELM electron density buildup can be attributed to impurity influx and ionization
- Time-resolved inter-ELM profile evolution reveals two distinct phases of inter-ELM evolution: (i) rapid initial recovery of main-ion and electron density followed by (ii) slower impurity and electron density buildup with primarily impurity fueling.
- The temporal dynamics and rate of impurity influx is consistent with the establishment of an impurity pinch early in the ELM cycle, which preferentially favors inward impurity transport over main-ion fueling in these conditions. By flattening the electron and main-ion density (by reduced recycling or increased opacity) it is predicted that the inward impurity pinch can be reduced, eliminated, or even reversed.
- These observations bear a striking resemblance to the 3D triggered ELMs reported in NSTX [Scotti 2016, Scotti 2013] where the impurity builds up and stagnates near the top of the pedestal due to competing neoclassical pinch and screening.
- Future studies that systematically vary the deuterium recycling flux and simultaneously measure lower charge-states of impurities to assess the ionization rate and electron particle source may shed light on the role of impurity ionization on the electron pedestal density structure

A series of low ELM frequency DIII-D discharges without auxiliary gas puffing were examined to determine the potential interplay of main-ion and impurity transport and impurity ionization on the ELM cycle, and hence total impurity content and core contamination. The goal of the analysis is to determine the process by which impurities cross the pedestal and enter the core by examining the spatial and temporal evolution of electrons, main-ions and impurities between ELMs, constrained by direct main-ion measurements [Haskey 2018]. Direct main-ion measurements greatly enhance the interpretation of the density pedestal recovery by avoiding complexities of the radial charge-state distribution of carbon (from neutral carbon to fully ionized C^{+6}). One clear observation made from direct main-ion measurements was that the total main-ion charge-exchange (CX) emission from the top of the pedestal, which is directly proportional to the deuterium pedestal ion density, does not directly track the evolution of the electron density pedestal. This observation is shown in Figure 3.1.1 where the inter-ELM main-ion emission is nearly constant in time, only showing a brief rise before saturation between each ELM. Similar observations were made during the profile buildup following an L-H transition [Haskey 2018]. Here in Figure 3.1.1(a) the red vertical bars obscure those times during the ELM where main-ion analysis is more challenging due signal saturation. When compared to Figure 3.1.1(b) we see that the electron density rise must be occurring because of an additional particle source (to satisfy quasineutrality) beyond the fuel neutral recycling. The

inter-ELM electron density pedestal recovery in this condition appears to be dominated by impurity influx and impurity ionization, and therefore the rate of impurity ionization should be included as a source when assessing electron particle transport in this H-mode pedestal.

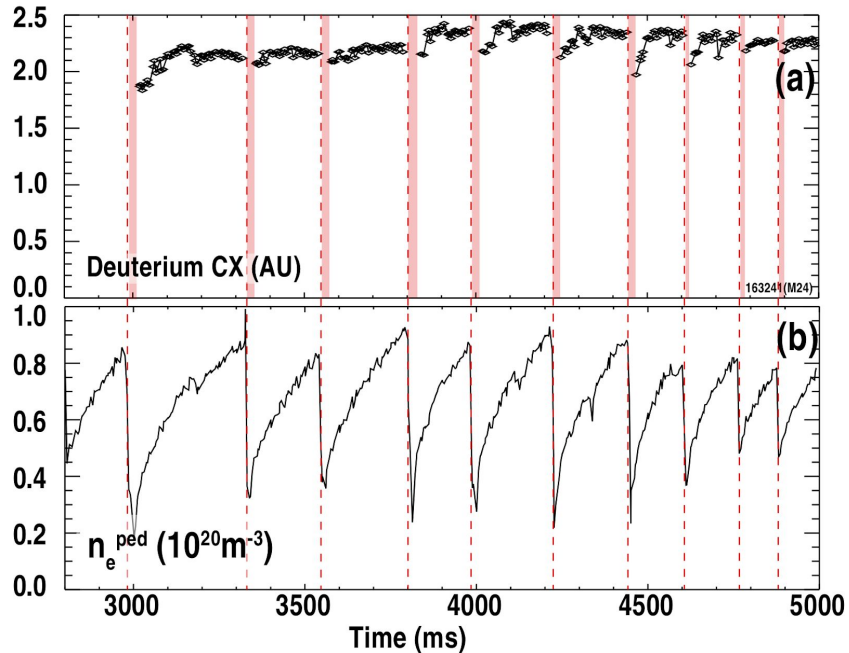


Fig. 3.1.1: (a) Direct measurement of the main-ion charge-exchange at the top of the pedestal (proportional to main-ion density) and (b) electron density at the top of the pedestal. Red regions indicate ELMs. After a short initial rise, the main-ion density saturates, while the electron density continues to rise until the next ELM.

By inspection of the time evolution in Figure 3.1.1, the main-ion measurements indicate that the establishment of the main-ion density profile may precede the impurity influx, consistent with the onset of an impurity pinch, followed by inward impurity transport. During 3.0 seconds of tokamak time the discharge displays multiple large ELMs with an inter-ELM period of 190 ms. This inter-ELM phase has been divided into 10 segments from 5-15% and 10-19% - 90-99% of the ELM cycle in 10% segments shown in Figure 3.1.2. For each segment, the electron profiles (n_e , T_e) have been aligned to 70 eV based on [Leonard 2017] with 3.0 MW of NBI heating and fit using a modified hyperbolic tangent. Ion profiles have been aligned with the occurrence of the radial electric field rising through zero at the separatrix, and fit with a modified hyperbolic tangent for carbon density, and splines for Ti and toroidal rotation Ω . During the inter-ELM period, the largest variations are in the particle transport channel, with the thermal and momentum transport displaying rapid profile establishment. These observations are expected from considerations of thermal transport being driven largely from the core outwards, whereas the particle transport is dominantly driven from the edge inwards by stronger edge sources than core fueling. One peculiarity that is observed in this analysis is a non-monotonic main-ion density feature near the top of the pedestal that arises due to enforcing quasineutrality. By

computing the main-ion density in the presence of a single, fully stripped impurity as $n_D = n_e - 6n_C$, we observe a localized peak in the main-ion density between $\psi_N = 0.95-0.98$. The existence of this feature is peculiar and unexpected from diffusive-like particle transport, because the locally positive deuterium density gradient should drive deuterium particle transport into the core. However, such features have been reported to be consistent with previous measurements [Haskey 2016] and observed inside the top of the pedestal in NSTX H-mode discharges [Delgado-Aparicio 2009] where the impurity transport was well-explained by neoclassical theory.

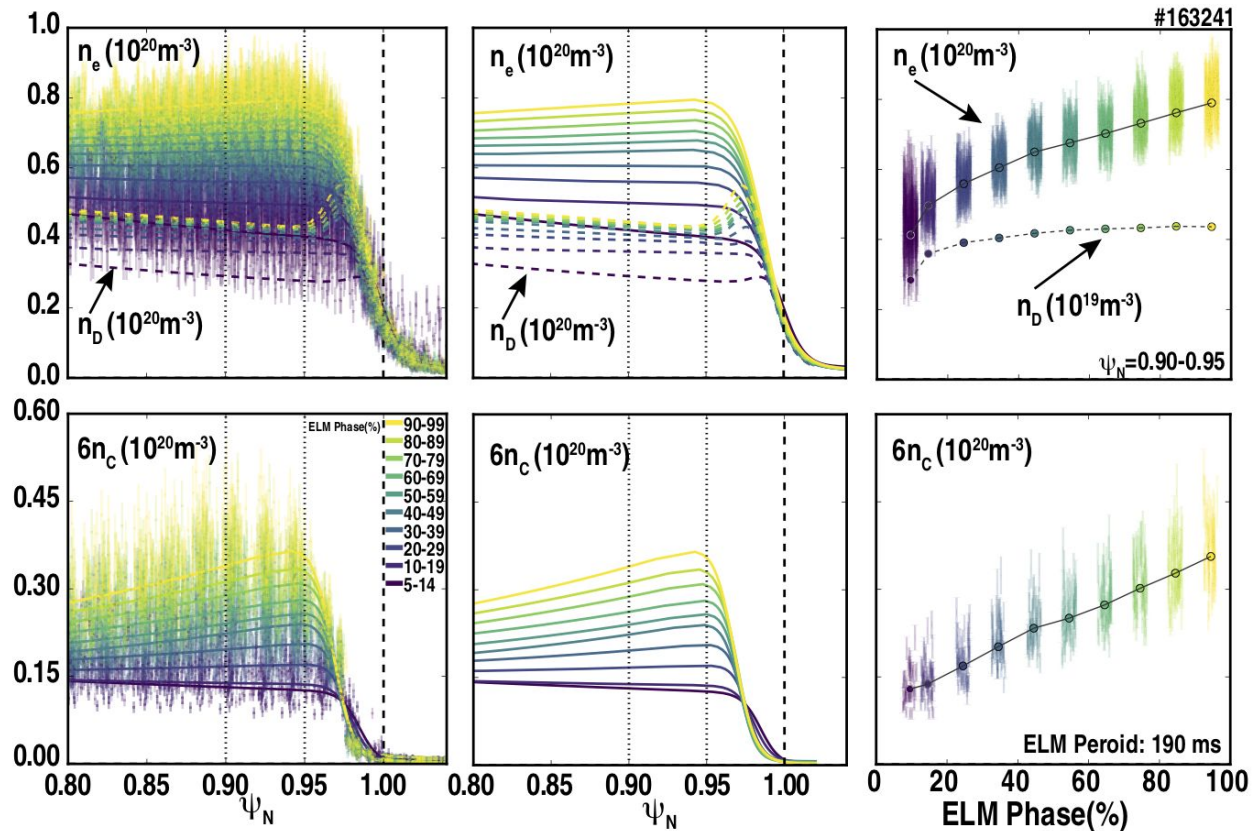


Fig. 3.1.2: ELM phase synchronized analysis of the pedestal recovery over 3.0 seconds of quasi-stationary conditions shown in space with (left) data and fits, (middle) fits only and (right) time evolution at top of pedestal. ELM phase has been divided into 10 segments and reveals dominance of carbon fueling beyond 20% into ELM cycle. Profile reconstruction and quasi-neutrality consistent with the time evolution in Fig. 3.1.1.

The impurity transport code STRAHL [Behringer 1987, Dux 2007] is designed to simulate multi-charge-state impurity transport in the tokamak by using theory-based neoclassical transport NEOART [Peeters 2000] or user-defined transport coefficients. For this investigation of dynamic pedestal recovery where the impurity produces significant main-ion dilution, the use of NEOART inside of STRAHL is a convenient tool for self-consistent evolution of the profiles and transport coefficients. Here we test STRAHL using NEOART to determine the existence

and magnitude of an edge impurity pinch, and the ability of neoclassical transport to capture key features of the dynamics. For impurity transport in the pedestal, the dominant neoclassical pinch originates from the high collisionality Pfirsch-Schlüter contribution. The inputs to the simulation are the experimental equilibrium and time evolution of the electron density, electron and ion temperature profiles. Given an impurity source, which is adjusted to match the observed level of carbon, and computed neoclassical transport with NEOART, STRAHL computes the influx of neutral carbon, ionization and transport of each charge state. For these simulations, a low level of anomalous diffusion ($0.01 \text{ m}^2/\text{s}$) at the separatrix and in the SOL was needed to accurately capture the time scale seen experimentally. As the impurity carbon enters the plasma, the background main-ion density is reduced appropriately to satisfy quasineutrality. The results of the simulation are shown in Figure 3.1.3, and reveal an inwardly directed impurity pinch in the steep gradient region, and weaker outward screening inside the top of the pedestal. These two competing effects produce the significant buildup of carbon near the top of the pedestal, consistent with the measurements in Figure 3.1.2 and seen in NSTX [Scotti 2013]. In time, the magnitude of the inward pinch increases slightly and shifts radially inward as the presence of the impurity modifies the main-ion density profile.

During the ELM cycle, STRAHL with NEOART predicts an edge peaked carbon density profile (C^{+6}) consistent with the shape of the measured profile in Figure 3.1.2. STRAHL contains the atomic physics to determine the radial charge-state distribution of lower ionization stages of carbon, and indicates that both hydrogen-like and helium-like carbon inside the separatrix, which can contribute to an electron particle source by collisional electron-impact ionization.

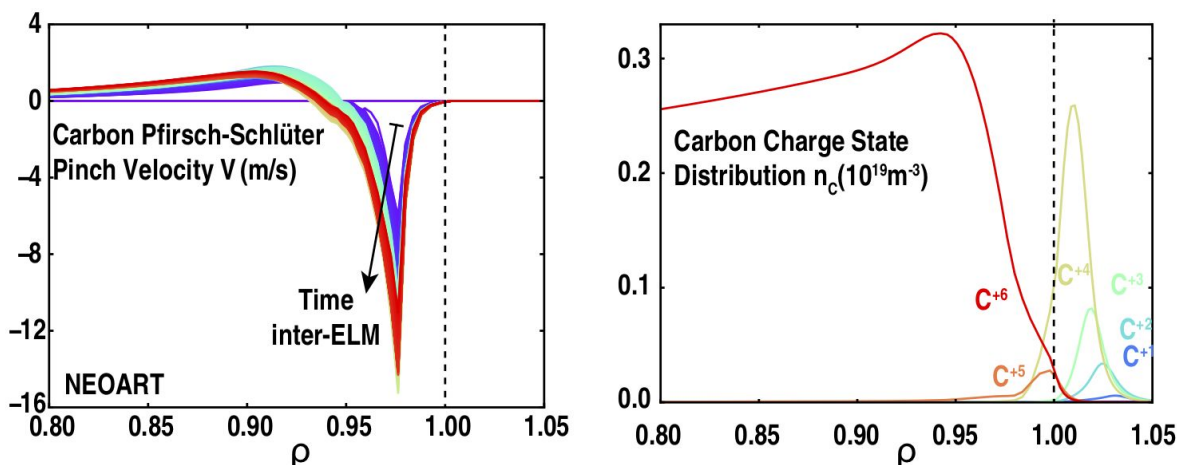


Fig. 3.1.3: (left) Impurity pinch velocity in the H-mode pedestal calculated from NEOART inside of STRAHL during the inter-ELM evolution and (right) radial charge-state distribution of carbon in the middle of the ELM cycle showing lower charge-states of carbon existing near the separatrix.

The STRAHL simulation points to an important role of the neoclassical pinch in producing the time evolution of the impurity density rise, consistent with H-mode results from Alcator C-Mod, as well as the shape of the carbon density profile near the top of the pedestal in NSTX. While

fully stripped carbon (C^{+6}) is the dominant charge state over much of the profile, a narrow region near the plasma separatrix is populated by lower charge states (C^{+5} , C^{+4}) that exist here where the electron temperature is low and near the ionization potential. Future studies that use charge-exchange spectroscopy of hydrogen-like and helium-like carbon may reveal the role of these carbon charge states on the electron density pedestal structure. In the conditions reported here, increasing the ELM frequency f_{ELM} will reduce the plasma impurity concentration and Z_{eff} since most of the main-ion fueling occurs shortly after the ELM. Similarly, increasing the gas puff and recycling flux will produce more direct relative main-ion fueling compared to impurity contamination by transport, also increasing the plasma purity. Ultimately, the combined use of main-ion, electron and impurity measurements provide unique constraints for interpreting the dynamic evolution during the ELM cycle with theory-based models.

References for Section 3

[Wade 2005] M.R. Wade, et. al., “Edge-Localized-Mode–Induced Transport of Impurity Density, Energy, and Momentum”, *Physical Review Letters*, 94, 225001, 2005

[Callen 2010] J.D. Callen, et. al. “Analysis of pedestal plasma transport” *Nucl. Fusion* 50 064004, 2010

[Kotschenreuther 2019] M. Kotschenreuther, et. al. “Gyrokinetic analysis and simulation of pedestals to identify the culprits for energy losses using ‘fingerprints’”, *Nucl. Fusion* 59 096001, 2019

[Hirshmann 1981] S. Hirshman and D. Sigmar “Neoclassical transport of impurities in tokamak plasmas” *Nucl. Fusion* 21 1079, 1981

[Rice 2015] J.E. Rice, et. al. “Core impurity transport in Alcator C-Mod L-, I- and H-mode plasmas” *Nucl. Fusion* 55 033014, 2015

[Pütterich 2011] T. Pütterich, et. al. “ELM flushing and impurity transport in the H-mode edge barrier in ASDEX Upgrade” *Journal of Nuclear Materials* 415 S334–S339, 2011

[Dux 2014] R Dux, “Transport of tungsten in the H-mode edge transport barrier of ITER” *Plasma Phys. Control. Fusion* 56 124003, 2014

[Mordijck 2019] S. Mordijck, et. al., “Role of transport versus fueling upon pedestal density”, *FES Joint Research Target*, 2019

[Grierson 2015] B. A. Grierson, et. al., “Impurity confinement and transport in high confinement regimes without edge localized modes on DIII-D”, *Phys. Plasmas* 22, 055901, 2015

- [SunnPedersen 2000] T. Sunn Pedersen, et. al., "Radial impurity transport in the H mode transport barrier region in Alcator C-Mod", Nuclear Fusion, Vol. 40, No. 10, 2000
- [Rice 1997] J.E. Rice, et. al., "Impurity transport in Alcator C-Mod plasmas", Phys. Plasmas, Vol. 4, No. 5, May 1997
- [Victor 2020] B.S. Victor, et. al. "Impurity transport in the pedestal of H-mode plasmas with resonant magnetic perturbations" Plasma Phys. Control. Fusion 62 095021, 2020
- [Hinson 2020] E.T. Hinson, et. al. "Enhanced helium exhaust during edge-localized mode suppression by resonant magnetic perturbations at DIII-D" Nucl. Fusion 60 054004, 2020
- [Scotti 2013] F. Scotti, et. al., "Core transport of lithium and carbon in ELM-free discharges with lithium wall conditioning in NSTX", Nucl. Fusion 53 083001, 2013
- [Belli 2008] E A Belli and J Candy, "Kinetic calculation of neoclassical transport including self-consistent electron and impurity dynamics", Plasma Phys. Control. Fusion 50 095010, 2008
- [Scotti 2016] F. Scotti, et. al. "Kinetic profiles and impurity transport response to 3D-field triggered ELMs in NSTX", IAEA-FEC 2016 EX/P4-36, 2016
- [Hulse 1983] R.A. Hulse, "Numerical Studies of Impurities in Fusion Plasmas", Nucl. Technol. Fusion, 3:2, 259, 1983.
- [Haskey 2018] S.R. Haskey, et. al. "Active spectroscopy measurements of the deuterium temperature, rotation, and density from the core to scrape off layer on the DIII-D tokamak", Rev. Sci. Instrum. 89 10D110, 2018
- [Haskey 2018] S.R. Haskey, et. al., "Main ion and impurity edge profile evolution across the L- to H-mode transition on DIII-D" Plasma Phys. Control. Fusion 60 105001, 2018
- [Leonard 2017] A.W. Leonard et. al. "Compatibility of separatrix density scaling for divertor detachment with H-mode pedestal operation in DIII-D" Nucl. Fusion 57 086033, 2017
- [Haskey 2016] S. R. Haskey, et. al. "Measurement of deuterium density profiles in the H-mode steep gradient region using charge exchange recombination spectroscopy on DIII-D" Review of Scientific Instruments 87, 11E553, 2016
- [DelgadoAparicio 2009] L. Delgado-Aparicio et. al. "Impurity transport studies in NSTX neutral beam heated H-mode plasmas" Nucl. Fusion 49 085028, 2009

[Behringer 1987] K. Behringer, "Description of the impurity transport code 'STRAHL'" JET Joint Undertaking Report No. JET-R(87)08, Abingdon, United Kingdom, 1987

[Dux 2007] R. Dux, "STRAHL User Manual" Max Planck Institut für Plasmaphysik Report No. jpp 9/82, Garching, Germany, 2007

[Peeters 2000] A.G. Peeters "Reduced charge state equations that describe Pfirsch Schlüter impurity transport in tokamak plasma" Phys. Plasmas 7, 268, 2000

Section 4. Edge/Divertor Sourcing and Impurity Transport

Introduction

Impurities in a tokamak edge plasma, both intrinsic due to wall erosion and actively introduced via methods such as gas puffing and powder dropping, are strongly beneficial for dissipating the high parallel heat fluxes in the SOL/divertor region but can also be strongly detrimental if their concentration becomes too high. High-Z impurities are particularly detrimental to the plasma core; reducing reactivity, diluting fuel ions, and eventually inducing radiative collapse -- all at minute concentrations. The Lawson parameter space in which to achieve ignition is calculated to shrink dramatically for a core tungsten concentration above 3×10^{-5} and disappears entirely above 2×10^{-4} [Putterich 2010].

ITER and other future devices will be operated with a (partially) detached divertor in order to suppress physical sputtering of high-Z material [Stangeby 2011], as well as to mitigate the heat flux to the targets to acceptable levels. It is commonly observed, however, that the divertor can “re-attach” during Type-I ELM events, i.e., a transient increase occurs in the divertor ion impact energy spectrum due to energetic ions free-streaming to the divertor targets from the hot plasma core [Brezinsek 2015]. Assuming that the complete suppression of ELMs will not be successful in next-step devices [Pitts 2019], a limit on the ELM size will likely be set by the *net* erosion of tungsten from the divertor surfaces, i.e., the *W* gross erosion rate minus the local *W* re-deposition rate. Recent ERO modeling has calculated redeposition fractions of *W* during ELMs up to 99% in the JET-ILW divertor [Kirschner 2019] but this study used an ELM-average approach with no time dependence and no validation exercises were performed.

At present there is also a limited understanding of how impurities are transported from different wall source locations, influenced by the SOL plasma conditions, and/or thereby influencing divertor performance. Codes such as DIVIMP, EMC3-EIRENE and SOLPS-ITER often predict a poloidally-localized accumulation of impurities in the near-SOL (near the separatrix) in the vicinity of the midplane and/or crown due to the parallel T_i gradient [Elder 2019, Senichenkov 2019]. However, such impurity accumulation is very difficult to directly confirm due to lack of an appropriate diagnostic, e.g., spectroscopic, that can measure the relevant intermediate charge states, though indirect methods provide insight into the accumulation mechanisms. Experimental evidence of impurity accumulation in the near-SOL between the X-points, obtained via more indirect methods, such as collector probes inserted into the far-SOL, is an important step towards controlling impurity levels in the main plasma. Additional comparisons are needed to optimize a variety of potentially attractive operational regimes, including radiative divertor seeding, advanced divertor performance (e.g. detachment onset), and high-Z material migration from the divertor.

Evidence of near-SOL W accumulation via reproduction of far-SOL W deposition profiles with 3DLIM

Analysis Lead: Shawn Zamperini

Important conclusions from research on high-Z material migration include:

- Tungsten deposition profiles measured on a graphite rod Collector Probe (CP) located in the far-SOL near the outer midplane during W tracer experiments in DIII-D are reproduced by 3DLIM, a new 3D Monte Carlo far-SOL impurity transport code.
- Assuming purely diffusive radial transport (10 m²/s) results in the best agreement with experimental measurements of W deposition on the outer-target facing (OTF) sides of the CP. However, a purely convective radial transport model (125 m/s) is shown to simultaneously have better agreement with the both inner-target-facing (ITF) and OTF high-Z deposition profiles.
- Deposition profiles show peaking in W content along the length of the CP edges that is also reproduced in 3DLIM, but only when assuming a convection-dominated SOL plasma parallel transport prescription for the background plasma. The degree of the peaking is shown to be a secondary indicator of the effective location of the W source in the near-SOL
- Identifying the location of the effective source provides insight into near-SOL impurity dynamics, including the existence and location of impurity accumulation near the outboard midplane OMP separatrix. Such accumulation typically occurs in SOLPS and other edge code modeling, but has hitherto been difficult to confirm experimentally.

Modelling impurity transport in the scrape-off-layer (SOL) usually focuses on the near-SOL. The near-SOL is commonly defined as the small region of ~2 mm from the separatrix, but for clarity it is defined in this section as within ~1-2 density falloff lengths (λ_{n_e}) of the separatrix, ~5 cm at the OMP for a typical L-mode shot. This better distinguishes the regions of potential impurity accumulation where T_i gradients are appreciable from the far/very-far SOL of a Collector Probe (CP) where T_i gradients are negligible. Examples relevant to this study include studies on the near-SOL W sourcing rate [Abrams 2017], and the relative contributions from a near vs far target W source [Unterberg 2020]. The far-SOL, which covers the rest of the SOL out to the wall and involves plasma-wall interactions, is generally less studied. Even when codes such as DIVIMP and SOLPS are used to model the region from the separatrix to the wall, they are 2D codes based on the assumption of toroidal symmetry and thus exclude 3D effects. As will be shown, even if 2D behavior is a reasonable assumption elsewhere, impurity transport to a CP in the far-SOL is a 3D problem, and thus motivates development of a new code. The first results using the far-SOL Monte Carlo impurity transport code 3DLIM are reported [Zamperini 2020], here applied to interpretive modeling of double-sided CP measurements taken during the DIII-D Metal Rings Campaign (MRC) [Donovan 2018].

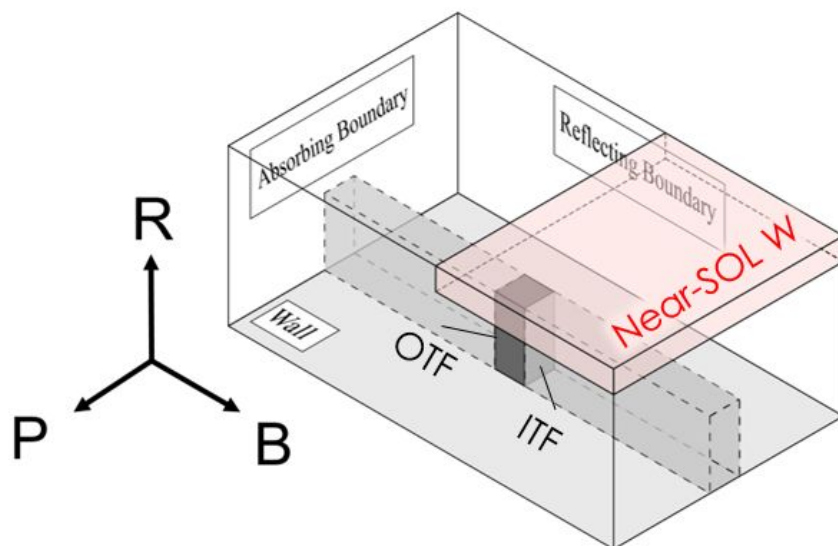


Fig. 4.1.1: 3DLIM geometry. The coordinate system is radial (R, or R-Rsep), parallel to the magnetic field (B) and poloidal (P). A double-sided collector probe is shown in dark grey with the flux tubes it intersects indicated. A specifiable impurity injection volume is shown in red representing a hypothesized impurity accumulation region in the near-SOL.

3DLIM is an upgrade of the LIM code, which itself was the predecessor to DIVIMP. It simulates the far-SOL in 3D, as shown in Figure 4.1.1, where the three directions use the naming convention radial (R), poloidal (P) and parallel to the magnetic field (B). A generic collector probe is shown in dark grey and can be placed anywhere in the volume. The region where parallel flux tubes intersect the probe is indicated by dashed lines. The poloidal direction is across the face of the probe, while the radial direction is along it. The parallel direction is normal to the faces. Absorbing boundaries are used to simulate the targets where field lines terminate and at the radially-outmost vessel wall. Reflecting boundaries are used at the poloidal computational boundaries at some specifiable distance from the CP; poloidal symmetry is assumed in the vicinity of the probe. The radially-innermost boundary is reflecting as well, though few, if any, particles ever reach this surface due to the radially outward nature of the ions in these simulations.

Electron density and temperature data from a plunging Langmuir probe is input into 3DLIM to generate various background plasma solutions to fill the computational region. The sink effect of the double-sided CP surfaces, which creates a zero-point effect in the background plasma flow midway between the CP surface and nearest absorbing boundary, is included in the background plasma modelling. The zero-point effect is such that the plasma flow on the half of the field lines nearest the probe are towards the probe face and on the other half are towards the absorbing boundaries. Shown in red in Fig. 4.1.1 is a specifiable 3D near-SOL impurity source volume that acts as a simplification for modeling the impurity ion source into the far-SOL. The code launches impurity ions from this region and applies various specifiable spatial steps at each time step,

such as but not limited to: radial, parallel and poloidal diffusion, inward/outward convective radial transport, and/or parallel transport due to the friction and T_{eli} gradient forces. The ions are followed until deposition on the simulation boundaries or on one of the two CP faces. Re-erosion of deposited impurities, which can be appreciable for probes close to the near-SOL, is neglected. The advantage of simulating only the far-SOL permits neglecting many of the other complicated aspects of impurity transport including sputtering, divertor leakage and near-SOL transport. By compartmentalizing the problem of SOL impurity transport with 3DLIM, it is possible to interpretively model the effective source of near-SOL W into the far-SOL and to broadly reproduce experimental CP measurements.

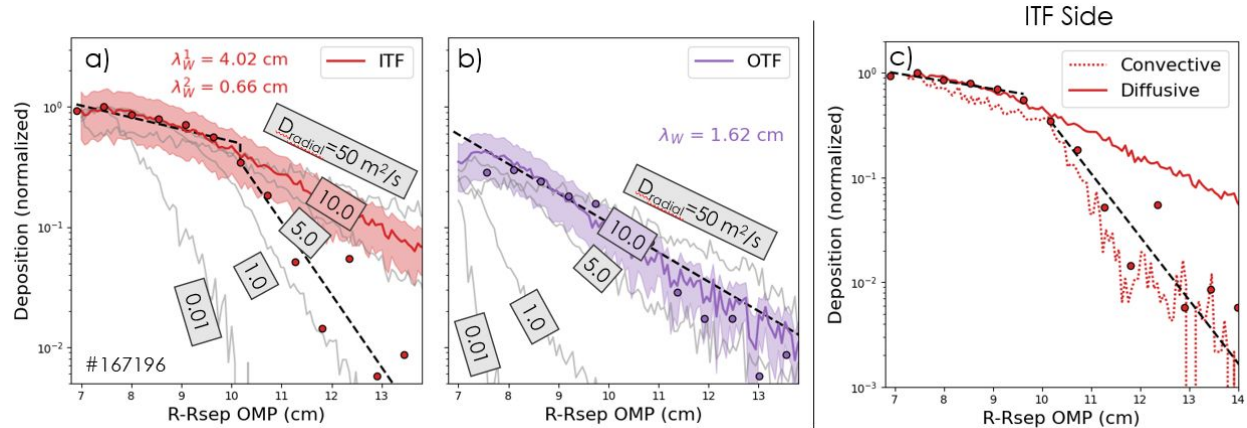


Fig. 4.1.2: Reproduction of measured radial deposition profiles by 3DLIM (note log y-scale). Dots are RBS measurements, and lines with uncertainty bands are from 3DLIM simulation. a)-b): Effect of varying D_{radial} from 0.01 to 50 m^2/s is shown in grey, with the optimal value of 10 m^2/s in color. c): The effect of diffusive versus convective radial transport is compared for ITF data.

The principal result of 3DLIM is the successful reproduction of the deposition profiles along the axial length of the probes under varying assumptions of radial transport, Fig. 4.1.2. The circles are Rutherford Backscattering (RBS) data from a CP inserted for 25 repeat L-mode shots. The anomalous radial diffusion coefficient, D_{radial} , is set for the entire simulation volume, thus we search for the value of D_{radial} that best matches both sides of the CP simultaneously. Results of a parameter scan from 0.1-50 m^2/s are shown in Figs. 4.1.2a and 4.1.2b. The optimal value of 10 m^2/s is the set of colored lines with uncertainty bands. The dotted lines are exponential fits to the RBS data and the corresponding λ values are the exponential fall-off lengths. In this simulation a 10x decrease in the connection length at $R - R_{sep} \geq 10$ cm on the ITF side is imposed to simulate the decrease in connection length with radial distance outwards in DIII-D. In Fig. 4.1.2c, the effect of diffusive versus convective radial transport on the ITF side is compared. The diffusive profile using $D_{radial} = 10$ m^2/s from Fig. 4.1.2a is reproduced, and for the convective profile W ions transport radially outwards at a constant speed of 125 m/s. The profiles at $R - R_{sep} \geq 10$ cm show that convective radial transport is more sensitive to a changing connection length than diffusive transport, as expected since $\lambda_{diff} \sim (LD_{radial})^{1/2}$, while

FY20 JRT FINAL REPORT / DIII-D MILESTONE 2020-3 REPORT CONTENT

By

**JRT team: N. Howard, T. Abrams, F. Scotti, B. Grierson,
A. Jaërvinen, T. Odstrcil, F. Sciortino, W. Guttenfelder, B. Victor,
S. Haskey, J. Nichols, S. Zamperini, A. Bortolon, F. Effenberg**

This is a preprint of a paper to be submitted to *DOE FES*, and possibly published online.

**Massachusetts Institute of Technology (MIT)*

This material is based upon work supported by the U.S. Department of Energy, Office of Science, Office of Fusion Energy Sciences, using the DIII-D National Fusion Facility, a DOE Office of Science user facility, under Award(s) DE-FC02-04ER54698.

DISCLAIMER

This report was prepared as an account of work sponsored by an agency of the United States Government. Neither the United States Government nor any agency thereof, nor any of their employees, makes any warranty, express or implied, or assumes any legal liability or responsibility for the accuracy, completeness, or usefulness of any information, apparatus, product, or process disclosed, or represents that its use would not infringe privately owned rights. Reference herein to any specific commercial product, process, or service by trade name, trademark, manufacturer, or otherwise, does not necessarily constitute or imply its endorsement, recommendation, or favoring by the United States Government or any agency thereof. The views and opinions of authors expressed herein do not necessarily state or reflect those of the United States Government or any agency thereof.

**GENERAL ATOMICS PROJECT 30200
OCTOBER 2020**

$\lambda_{conv} \sim (Lv_{radial})^1$, where λ signifies the radial exponential fall off length of the W density assuming either completely diffusive or convective transport.

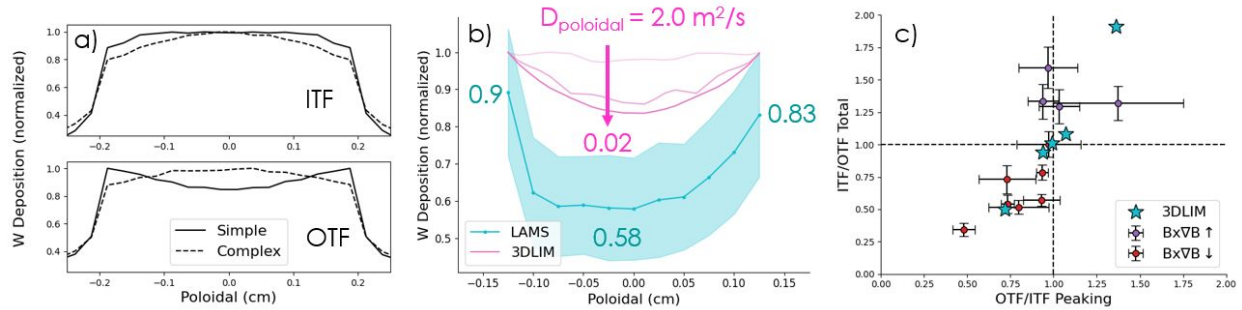


Fig. 4.1.3: a) Average poloidal profiles (across CP faces) from a set of 3DLIM simulations using either a simple or complex SOL prescription for the background plasma. b) Average poloidal profile from Laser Ablation Mass Spectrometry (LAMS) data in blue with a scan in $D_{poloidal}$ from 3DLIM in pink. c) Ratio of total W content plotted against the poloidal peaking ratio for 3DLIM and experimental data.

To obtain the average poloidal deposition profile from experiments and 3DLIM, each poloidal profile in the first 5 cm from the tip of the CP is averaged together. In Fig. 4.1.3a and 4.1.3b the left and right bounds correspond to the poloidal edges of the CP's deposition areas. Fig. 4.1.3a demonstrates that poloidal peaking of W deposition occurs only with a simple SOL plasma prescription, and only on the side opposite the effective source of W into the far-SOL (the OTF side). In Fig. 4.1.3b the blue line is the average poloidal profile from experimental LAMS data. The pink lines demonstrate the effect of a parameter scan in $D_{poloidal}$ from 2.0-0.2 m^2/s (light to dark pink). 3DLIM underestimates the degree of poloidal peaking compared to the experimental data.

To quantify the degree of poloidal peaking, the ratio between the amount of W on the edges to the center can be used. The LAMS data for an ITF probe in Fig. 4.1.3b measures $0.9/0.58=1.55$ times more W on the left edge, and $0.83/0.58=1.43$ on the right, for an average of 1.49 times more W deposited on the edges compared to the center. A similar process is performed for the CP's OTF face, and the ratio of these two computed numbers is dubbed the OTF/ITF Peaking Ratio for the CP. Fig. 4.1.3c is the ratio of the total amount of W deposited on the first 5 cm each CP face (ITF/OTF Total) plotted against the OTF/ITF Peaking Ratio. The circles are experimental RBS and LAMS data distinguished by the toroidal magnetic field direction the CP was inserted for (either ion $Bx \nabla B \uparrow$ or $Bx \nabla B \downarrow$, LSN), and the blue stars are from 3DLIM cases that reuse the simple SOL background from Fig. 4.1.2 with $D_{radial}=10 m^2/s$. These cases demonstrate the effect of a scan in the location of the effective W source into the far-SOL, all else held equal. The two 3DLIM points in the lower left quadrant assumed effective W sources in the OTF direction from the CP, where the lowest-left point's source is further away in the OTF direction compared to the other point in this quadrant. Similarly for the two points in the upper

right quadrant, except the sources are in the ITF direction. The point in the middle utilized a source with no preference to either direction.

The difference between diffusive versus convective radial transport in Fig 4.1.2c shows, as expected, that results for convective transport are more strongly affected by the shortened connection length beyond $R - R_{sep,OMP} = 10$ cm, namely shorter connection lengths result in a much smaller exponential decay in the deposition profiles (and thus a better match to the RBS data). The nature of each transport process may explain the difference between the two profiles. Convective transport is such that W ions travel radially at an approximately constant speed, ultimately depositing on the CP via parallel flow. Diffusive transport is a random process, (i.e. uses Monte-Carlo techniques in 3DLIM); a W ion can take a radial diffusive step outward from a point, but inward to that point as well. Thus, under the diffusive assumption, W that travels past a point could return to that point. This implies that, on average, there are more W ions at a specific point in the diffusive assumption compared to the convective assumption, resulting in generally flatter exponential decay profiles as shown in Fig. 4.1.2. This indicates that radial W transport in the far-SOL is most appropriately modelled as convective in this case and therefore can explain why the 3DLIM results under the assumption of diffusive transport lie above the ITF RBS data beyond 10 cm. Alternatively, if one assumes radial transport is some combination of convective and diffusive processes, then the corresponding values of $10 \text{ m}^2/\text{s}$ and 125 m/s for the diffusive and convective contributions can be considered to be upper bounds on their individual contributions. The convective transport speed of 125 m/s is close to the measured velocity of radial blob speed in the windowed region of DIII-D [Rudakov 2005] as well as the far-SOL of other tokamaks [Lipschultz 2005]. Finally, there are few (if any) measurements of $D_{poloidal}$ in the SOL, so in this study it is treated as a tunable parameter where $0.2 \text{ m}^2/\text{s}$ was found to give fair agreement with LAMS of the location (though not magnitude) of the poloidal peaking for a particular CP. It is possible that a detailed study on other CPs could reveal different trends perhaps in the location or severity of peaking.

In summary, the primary indicator of the location of the effective W source from the near-SOL into the far-SOL is the ITF/OTF Total ratio while the OTF/ITF peaking constitutes a supporting secondary indicator. Simulations that require near-SOL W source into the far-SOL from the ITF direction support the hypothesis of a near-SOL impurity accumulation. However, some simulations require an OTF directed source or one with no preference to either direction to reproduce CP deposition profiles. It is observed that when the ion $Bx \nabla B \uparrow$ (LSN, away from divertor), an ITF directed source into the far-SOL is required, while for $Bx \nabla B \downarrow$ (LSN, towards divertor) an OTF directed or non-preferential source is required. This possibly suggests a near-SOL impurity accumulation may indeed exist, though only when ion $Bx \nabla B \uparrow$. A possible explanation for this phenomena is empirically observed, strong inner target directed parallel SOL flow that may act to “flush out” impurities that would otherwise accumulate only when $Bx \nabla B \downarrow$. These observations are the topic of a future publication, and will be tested in a set of high-priority experiments on DIII-D in late 2020.

Migration and deposition of low-Z impurities injected for active wall conditioning in DIII-D

Analysis Lead(s): Alessandro Bortolon, Florian Effenberg

Important conclusions from research on migration and deposition of low-Z impurities injected for active wall conditioning during 2020 are as follows:

- Boron powder injection in DIII-D plasmas at rates as low 1-5 mg/s is sufficient to cause measurable changes in wall conditions, notably reducing the deuterium fueling from wall desorption.
- Growth of the boron layers in the far SOL region can be strongly affected by non-axisymmetric plasma footprint at the targets, resulting in striation patterns with alternating regions of erosion/deposition
- First 3D simulations of boron transport in the SOL with the EMC3-EIRENE code using a localized source of boron atoms show that the boron flux at the target can be toroidally asymmetric. However, the spatial scales are not compatible with the striations observed on DiMES, indicating that the latter cannot be ascribed to the source localization but are rather associated with uncompensated error fields.
- Parametric scans of background plasma parameters in LSN discharges indicate that plasma density plays an important role in determining the inboard-outboard asymmetry of the B fluxes to the targets. In particular, while low plasma density favors a more uniform distribution, high plasma density results in boron fluxes directly to the inner target. This difference appears to be primarily due to the role of the parallel friction force, which drags a greater fraction of B impurities to the high-field-side (inner target) at high plasma density.
- EMC3-EIRENE simulations also show that injection at high rates can perturb the background plasma fluid equilibrium, affecting SOL flows and consequently the spatial distribution of the boron flux at the targets.

The control of impurity concentration in the plasma starts at the wall, where impurities are sourced through the processes of chemical and physical sputtering. Since these processes affect only the first 100nm of plasma facing components (PFCs), it is possible to greatly affect the impurity sources by controlling the composition of the first layers. This concept is at the base of wall conditioning by deposition of low-Z coating materials, most prominently boron [Winter 1996]. Glow discharge boronization (GDB) is indeed a key element of the operation of present-day fusion devices [Buzhinskij 1997]. The technique allows the deposition of boron rich layers on the plasma facing components of thickness of 10-100nm, by executing prolonged glow discharges, with a carrier gas (He, D₂) and a boron rich gas (e.g. B₂D₂). In both carbon and tungsten wall machines, GDB is executed routinely and has been proven time and again to enable operation by reducing impurity sources and strongly reducing the wall particle source (wall fueling) associated with desorption of deuterium. While glow GDB represents a key tool for present-day devices to achieve low collisionality, low impurity concentration, and high

performance plasma, this technique requires frequent interruptions of tokamak plasma operation, when the vessel is free of magnetic fields, to allow effective glow discharges. As such, GDB does not extrapolate to a long pulse, superconductive fusion device, exposing a critical issue for impurity control strategies of next generation devices.

Recent experiments in DIII-D and other devices internationally have investigated the potential of in-situ, real-time growth of low-Z wall coatings by injection of low-Z materials as particulates [Bortolon 2019]. High purity boron powder is injected into tokamak plasma discharges gravitationally using the impurity powder dropper (IPD) [Nagy 2018]. Because of the low injection velocity $\sim 5\text{-}10$ m/s and the small particle size ($\sim 0.1\text{mm}$), most of the injected powder is ablated in the scrape-off layer and the ionized boron is transported to the PFC where it can accumulate forming boron-rich layers.

In the course of this milestone, two DIII-D experiments have been carried out investigating specifically real-time wall conditioning through injection of boron powder in tokamak plasmas. The main experimental goals were the following:

1. To establish the effectiveness of the technique and quantify the minimum amount of injected B to obtain measurable and favorable wall conditioning effects.
2. To study the physics of growth of the boron-rich layer on the wall, in particular in the near target regions using DiMES[Wong 1992] to collect and characterize the deposited coatings as a function of distance from the outer strike point

For both experiments, the plasma scenario chosen was a lower single null shape, with the outer strike point (OSP) located on the inner edge of the lower divertor “shelf” to provide full diagnostic access to the outer target. Boron powder injections were delivered at initially small and further increasing rates from 1-50 mg/s during the full length of the density flat top. Typically 1-50 mg of boron was injected per shot. The boron powder used in these experiments is isotopically enriched to have the percentage of $^{11}\text{B} > 95\%$.

The improvement of wall conditions with B powder injection has been quantified in a sequence of plasma discharges with progressively higher quantities of boron injected, from 2 up to 20 mg per discharge. Two parameters were chosen as figures of merit of the wall conditions, in terms of wall recycling/fueling (C_{wall}) and wall impurity source ($C\%$), respectively. The wall condition $C_{\text{wall}} = \Gamma_{\text{D}} / \langle n_e \rangle$ consists of the ratio of the gas fueling divided by the achieved plasma density for repeat shots with the same pre-fill and density target trajectory. Higher values indicate a reduction of wall fueling and improvement of wall conditions, as more gas puffing through the valve is required to achieve the target density. $C\%$ represents the carbon concentration (n_{C}/n_e) in the pedestal. An effort was made to achieve constant wall conditions by simple repetitions of the target discharge, allowing for the deconvolution of the active wall conditioning effect from the effect of baseline plasma cleaning. The results in Figure 4.2.1 indicate that injection of B powder results in a systematic increase of C_{wall} , i.e., a reduction of wall fueling. The execution of anomalously long helium glow discharge cleaning (He GDC) due to aborted discharge launch sequences resulted

in step-like increases of C_{wall} . This observation allows us to infer that ~ 25 mg of B can reduce the wall fueling similarly to 8 min He GCD.

A corresponding reduction of C concentration in the plasma is not clearly seen. This observation, presently under scrutiny, could be associated with a low purity of the B-rich layer associated with the low injection rates. It should be noted that the location of C source for DIII-D plasmas is still an open question. While it is intuitive that the C source would be dominantly from regions of strong PMI, i.e. the strike points, C concentration has been observed to depend weakly on strike point detachment, suggesting a dominant role of main chamber wall source [Groth, private communication]. In the situation where the intrinsic carbon concentration is driven by main chamber interactions, coating of the strike point targets would have a weak effect on the C concentration in the plasma.

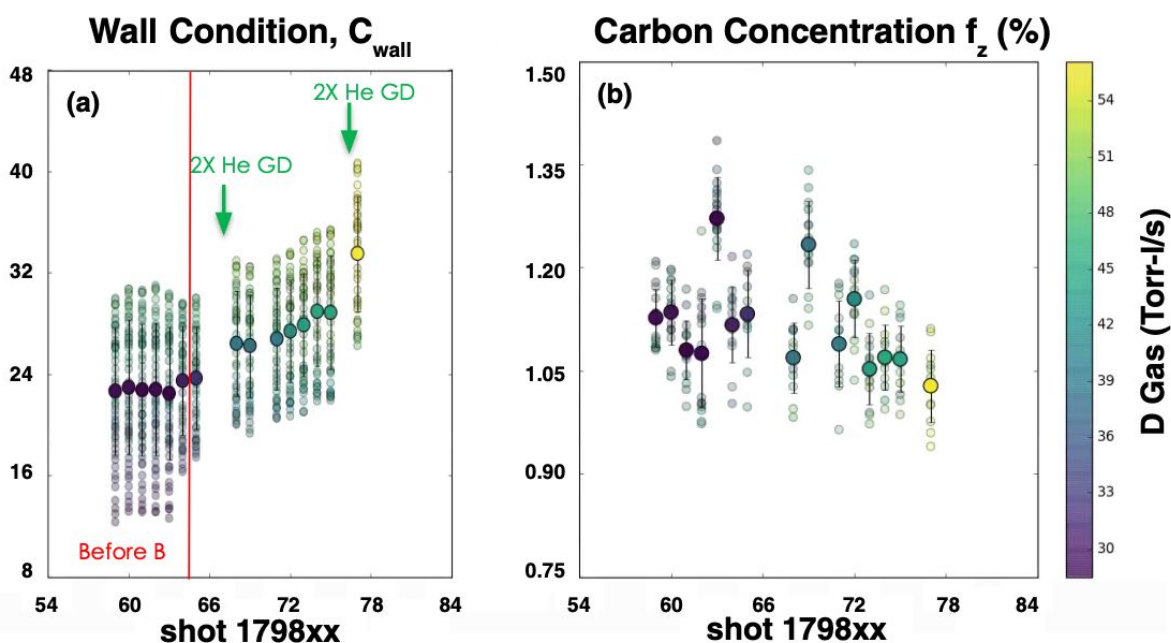


Fig. 4.2.1: Wall conditioning parameter C_{wall} (a) and carbon concentration in the pedestal (b) for a sequence of DIII-D discharges with B powder injection.

The DiMES probe was utilized to collect samples of the deposited B layer. DiMES consisted of a W-coated substrate inserted so as to be flush with divertor tiles. The OSP was located ~ 6 cm inboard of DiMES. Upon exposure to plasma with B injection, clearly visible striations were found on the DiMES surface, associated with non-axisymmetric error fields resulting in splitting of the strike point (Figure 4.2.2a). Notice that while these plasmas did include error field compensation, the error field compensation is used to minimize magnetic perturbation in the core, typically around $q=2$, and does not necessarily reduce the impact of error fields in the plasma edge. Analysis of the samples with Laser Ablation Mass Spectroscopy by J. Duran (UTK) has been carried out on a portion of the exposed DiMES substrate (Figure 4.2.2b,c). This

technique discerns the content of different isotopes and allows us to confirm that the striations result from alternating regions of clean W (regions of net B erosion) and regions with coatings of the injected B powder (net B deposition). The pattern of isotopes indicates that the plasma material interactions, in terms of erosion and re-deposition, are occurring in 3D with radial scales that can be as small as 0.5 cm.

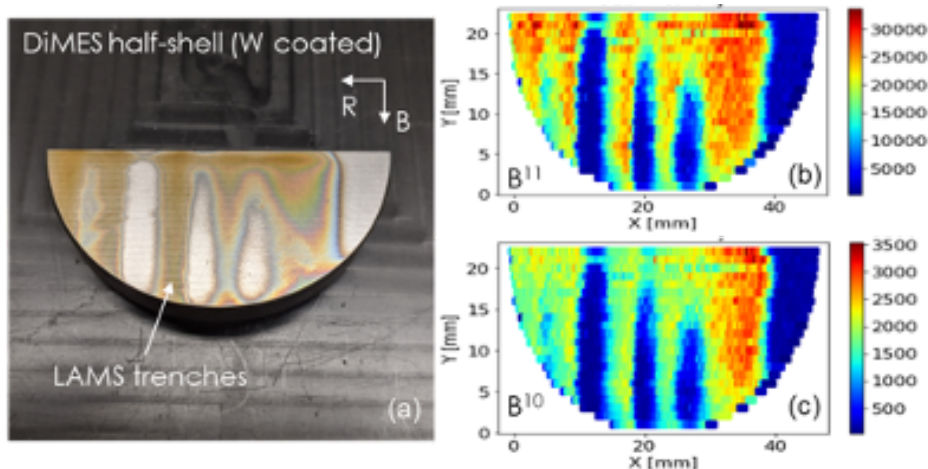


Fig. 4.2.2: (a) Surface of a portion of the DiMES sample exposed to plasma discharges with B powder injection. The field aligned striations result from deposition of B-rich coatings in presence of strike point splitting associated with error fields. (b,c) results of surface analysis with Laser Ablation Mass Spectroscopy, indicating that the coated regions contain B with isotopic composition consistent with the injected power. Intensity in (a.u.) but relative scale meaningful. (courtesy of J. Duran, UTK)

The fully 3D plasma-fluid and kinetic edge neutral transport Monte-Carlo code EMC3-EIRENE has been employed to model the SOL impurity transport and impurity fluxes onto the divertor, in order to investigate the role of the toroidally localized source of B from the IPD injection [Effenberg 2017]. The 3D transport simulations find that a localized B source introduces a localized perturbation in the SOL plasma pressure, due to localized radiative losses, which results in a spatial modulation of heat and particle fluxes and downstream electron temperature and density profiles. Generally, the simulations indicate that total impurity fluxes to the targets cover the full toroidal domain of the far SOL on the divertor targets.

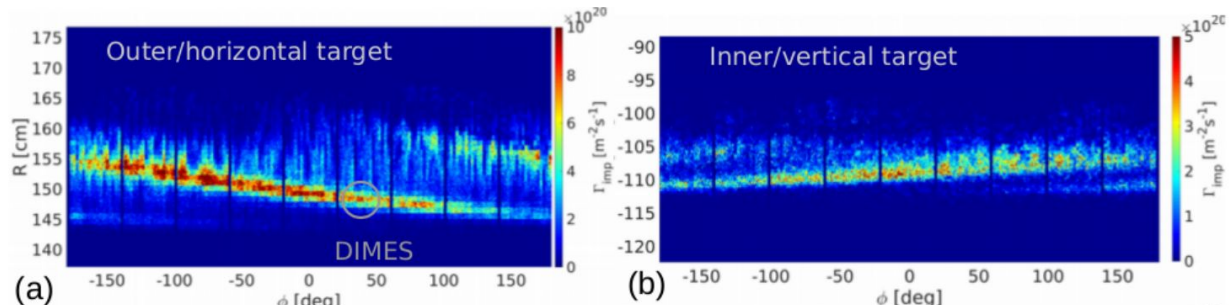


Fig. 4.2.3: Target plasma parameter obtained with 3D PWI modeling with EMC3-EIRENE for a case with B source $G=10^{21}$ atoms/s. (a) Boron impurity flux to the outer and (b) inner target.

However, as shown in Figure 4.2.3, the peak of the B impurity flux distribution moves radially across the inner and outer divertor targets when followed in the toroidal direction. This particular pattern is a result of the ionization and anomalous cross-field transport in competition with the fast parallel transport within the 3D transport model. While these 3D modeling results reveal a potential cause of striation patterns in the boron layer deposition, these are characterized by spatial scales larger than those observed on DiMES. We conclude that the latter are likely to be associated with uncompensated error fields and not with 3D transport phenomena.

The simulations show also strong inboard-outboard asymmetries in the B density distribution and parallel flux. These are determined by the competition between the ion thermal force associated with the parallel ion temperature gradient, and the friction force associated with the drag from the main ion flows. In particular, B transport shows a strong drag of B to the high field side for scenarios with separatrix densities around $1.5 \times 10^{19} \text{ m}^{-3}$ and heating of 2.2 MW (typical for the L-mode scenarios considered previously). This is visible in the 3D distribution of B for the case simulated, shown in Figure 4.2.3. The neutral B is introduced at $Z = 100.2$ mm with an influx rate of 10^{21} s^{-1} as shown in Figure 4.2.4 (a). The ionized B is dragged to the high field side by the far SOL flows (Figure 4.2.4(a-f)). The corresponding divertor B fluxes are shown in Figure 4.2.5. Notice that effects of macroscopic particle transport, sputtering, recycling, and ExB drift are not included in the current model.

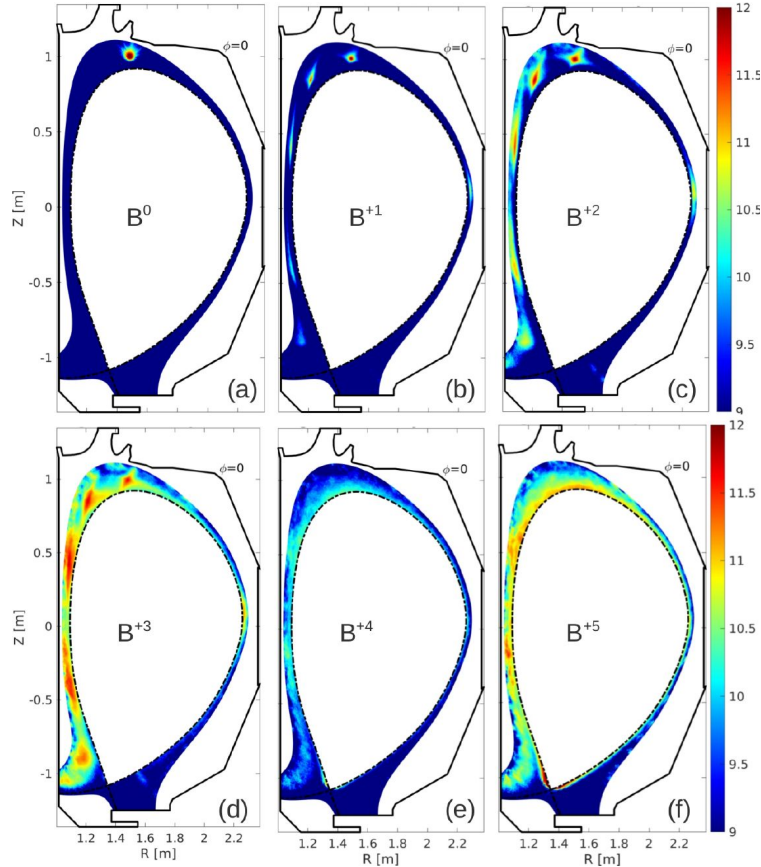


Fig. 4.2.4: B density distribution for (a) neutral B (source location), and (b - f) ionized Boron (B^{+1} - B^{+5}).

The simulation results reveal the role of the parallel impurity forces for the B distribution. The dominating terms of the impurity force balance equation are the ion thermal force F_{ith} and the friction force F_{fr} . The ion thermal force is induced by the ion temperature gradient and points to the upstream, while the frictional force is related to the main ion flow and points downstream. The impurity flow velocities caused by the leading terms in the impurity balance equation are shown in Figure 4.2.5 (a - c). Figure 4.2.5 (a) and (b) show the counter-streaming impurity flow velocities of the frictional (V_{fr}) and ion thermal forces (V_{ith}). The difference between these two counter-directed impurity flows ($V_{\text{fr}} - V_{\text{ith}}$) is shown in Figure 4.2.5 (c) and suggests the dominance of V_{ith} in the SOL region near the separatrix while V_{fr} is stronger in the rear SOL. A variation of the densities shows its effect on the competing forces (Figure. 4.2.4 (d-f)).

Importantly, the modeling shows that a decrease/increase of the plasma density weakens/strengthens the high field vs. low field B flux ratios. In particular a more uniform distribution of the B density is achieved at lower densities ($1.0 \times 10^{19} \text{ m}^{-3}$, Figure 4.2.5(d)) while the role of frictional flows is exacerbated at higher densities, resulting in more B dragged to the high field side ($2.0 \times 10^{19} \text{ m}^{-3}$, Figure 4.2.5(f)).

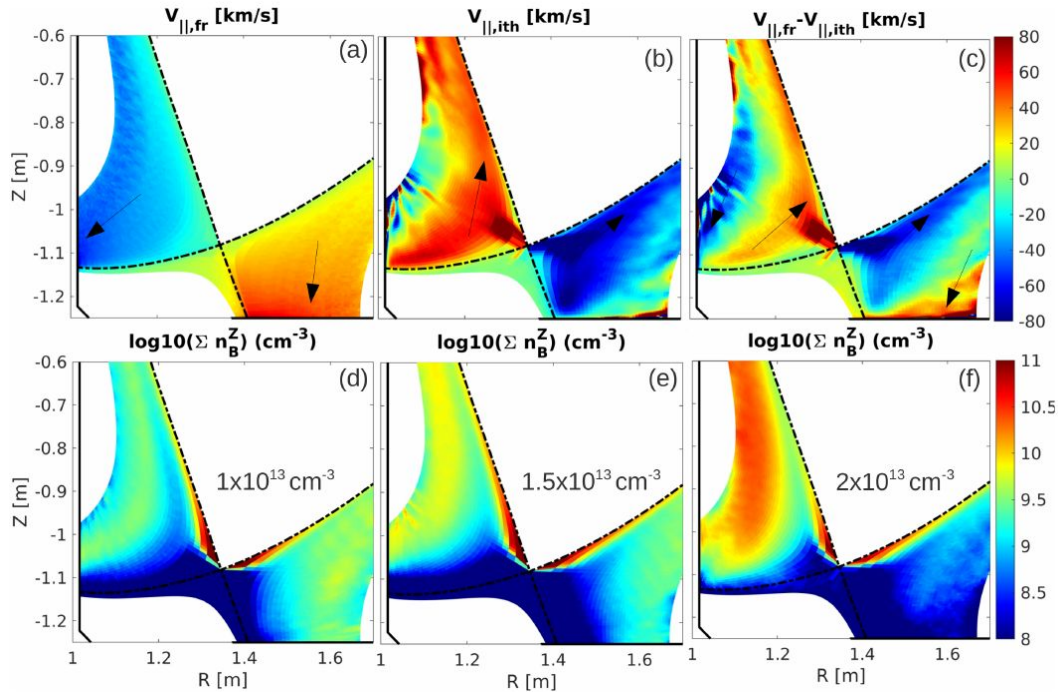


Fig. 4.2.5: (a) Ion thermal gradient force. (b) Frictional force. (c) Difference between F_{ith} and F_{fr} (d) Boron density for low (e) medium and high (f) upstream density.

Using parametric scans of parameters such as plasma density has been proven effective in delivering key information to:

1. Develop a better understanding of SOL impurity transport with local impurity sourcing
2. Guide the experimental optimization of the new technique of real-time boronization with B powder injection.

In particular, low density, low current scenarios appear to be more suitable for real-time boronization with boron powder injection, favoring a more uniform repartition of B flux between the inboard and outboard targets and more uniform toroidal distribution. More in general, the results show that a full 3D treatment is necessary to accurately resolve the B distribution in the SOL and on the divertor.

These key findings will guide future experiments for the development/application of RT-wall conditioning with B powder injection [Bortolon 2020].

Spectroscopic analysis of net vs. gross erosion of high-Z Plasma-Facing Components in DIII-D

Analysis Lead(s): Tyler Abrams

Important conclusions from research on spectroscopic analysis of net vs. gross erosion of high-Z plasma-facing components include:

- Leveraging new rate coefficients and a recently developed UV spectroscopy system for DIII-D [Johnson 2019], detailed *in-situ* spectroscopic measurements of the re-deposition fraction of tungsten plasma-facing components was performed.
- The W net erosion near the outer strike-point (OSP) is observed to be nearly equal to the gross erosion when the neutral W ionization length, λ_{iz} , is large compared to the W gyro-radius, ρ_W , and the width of the magnetic sheath, λ_{sh} . As the λ_{iz} decreases, the rate of tungsten net erosion also decreases relative to W gross erosion, with a strong inflection point near $\lambda_{iz}/\rho_W \approx \lambda_{iz}/\lambda_{sh} \sim 2-3$. At the lowest ionization lengths achieved, $\lambda_{iz}/\rho_W \approx \lambda_{iz}/\lambda_{sh} \sim 0.4$, W net erosion decreases to as little as $\sim 20\%$ of the gross erosion.
- These results are compared to two different analytic models, which assume that the W re-deposition physics is dominated by (a) the gyro-orbit trajectories of sputtered W ions or (b) electrostatic forces within the magnetic pre-sheath. Measurements of W net erosion are generally lower than the models predict when λ_{iz} is large. This discrepancy is attributed to non-local W re-deposition, which is not included in the models.
- Conversely, when λ_{iz} is small relative to ρ_W and λ_{sh} , substantially more W net erosion is measured than predicted by the analytic models. This indicates that W re-deposition from charge states higher than W^+ are likely also important.

This work develops and refines a method for measuring both the tungsten gross erosion and local re-deposition rate simultaneously [Abrams 2020]. Such measurements will eventually allow for models for the time evolution of W net erosion during the ELM cycle to be tested and validated. Time-resolved tungsten gross erosion and re-deposition can be inferred, using a few simplifying assumptions, from spectroscopic measurements of a neutral W line (WI) and a singly-ionized W line (WII).

In a simple picture of tungsten plasma-materials interactions (PMI), tungsten material is eroded with characteristic rate R_{gross} due to physical sputtering. Sputtered neutral atoms undergo ionization with characteristic rate coefficient S_0 and radiate (at a given spectral line) with characteristic excitation rate coefficient X_0 times branching ratio B_0 . The same volumetric atomic physics applies to singly-ionized W^+ atoms, with characteristic rates S_1 , X_1 , and B_1 , respectively. For W^+ atoms, there also exists a re-deposition flux R_{reddep} for ions that re-deposit on the W target surface. It is assumed that the divertor electron temperature is sufficiently high such that re-deposition is negligible. Thus the continuity equations for W^0 and W^+ can be written as follows:

$$\frac{dn_0}{dt} = \Gamma_{gross} - n_e n_0 S_0(n_e, T_e) \quad \frac{dn_1}{dt} = n_e n_0 S_0(n_e, T_e) - n_e n_1 S_1(n_e, T_e) - \Gamma_{redep}$$

where n_0 and n_1 are the density of neutral and singly ionized W atoms, respectively. Assuming equilibrium ($d/dt = 0$) and re-arranging terms, we obtain:

$$\Gamma_{gross} = \frac{S_0}{X_0 B_0} \Phi_0 \quad \Gamma_{redep} = \Gamma_{gross} - \frac{S_1}{X_1 B_1} \Phi_1$$

where the quantities $\Phi_0 \equiv n_e n_0 X_0 B_0$ and $\Phi_1 \equiv n_e n_1 X_1 B_1$ have been defined. Physically Φ_0 and Φ_1 correspond to the photon emission flux from a WI and WII line, respectively, quantities that can be directly measured in experiments.

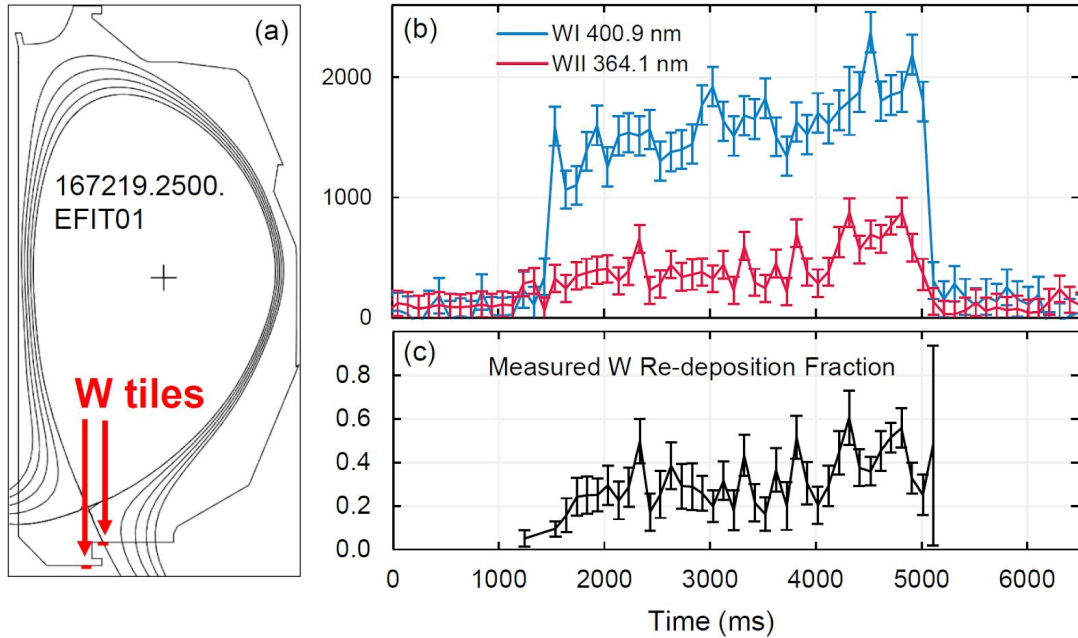


Fig. 4.9: (a) Magnetic equilibrium reconstruction showing the location of the outer strike-point on the W-coated tiles in the DIII-D divertor. (b) Time evolution of the WI and WII emission intensity (AU) measured on the W-coated tiles. (c) Inferred W re-deposition fraction based on the spectroscopic measurements.

Tests of this measurement technique were conducted by analyzing UV spectroscopic data [Johnson 2019] acquired in “piggyback” during the DIII-D Metal Rings Campaign [Wampler 2017]. 25 L-mode discharges were performed with the outer strike-point (OSP) placed on W-coated tiles in the DIII-D divertor. Variations in plasma conditions during these discharges enabled measurements of W gross and net erosion at a relatively broad range of values of W ionization lengths. The time evolution of the intensity of the WI and WII emission lines in the DIII-D divertor during one example discharge, along with the inferred W redeposition fraction,

$f_{redep} = (\Gamma_{redep}/\Gamma_{gross})$, are plotted in Figure 4.9. Because the plasma conditions are relatively constant in this discharge, the W re-deposition fraction is also relatively constant (within the error bars).

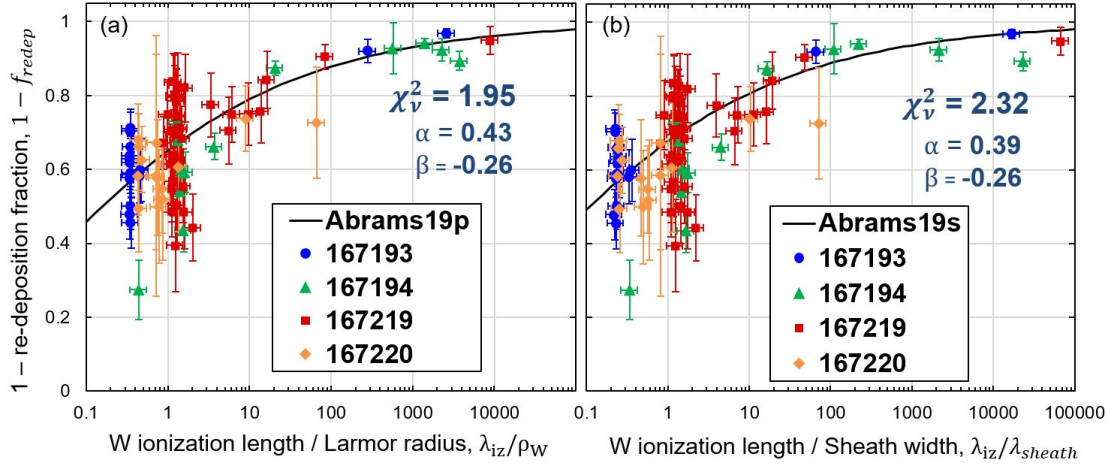


Fig. 4.10: Calculated W prompt re-deposition fraction as a function of (a) λ_{iz}/ρ_w and (b) $\lambda_{iz}/\lambda_{sh}$. The best-fit empirical scaling and the resulting parameters are overlaid in both cases.

This analysis, which was repeated for the entire database of discharges, can be tested against W re-deposition models. Naujoks [Naujoks96] has proposed an analytic model where f_{redep} varies with only the ratio of the neutral W ionization length to the W+ gyro-radius, λ_{iz}/ρ_w . Guterl [Guterl19] performed a set of simplified ERO simulations and concluded that W prompt re-deposition scales with the ratio of λ_{iz} to the width of the magnetic pre-sheath, λ_{sh} . The quantity $1 - f_{redep}$, which is proportional to the W net erosion rate, is plotted as a function of both of these ratios in Figure 4.10. In both cases a scaling law is overlaid of the form $1 - f_{redep} = \exp(-\alpha x^\beta)$, where α and β are empirical fitting parameters. A similar scaling with similar fitting parameters is produced in both cases. The reduced chi-square values of both fits are similar and of order unity, suggesting that both models may represent a good approximation to the W prompt re-deposition physics. The fit is slightly better for the Naujoks96 formulation.

In Figure 4.11, these measurement-derived empirical scalings are quantitatively compared to the Naujoks96 and Guterl19 predictions as a function of λ_{iz}/ρ_w and $\lambda_{iz}/\lambda_{sh}$, respectively. When the W ionization length is long relative to λ_{sh} and ρ_w , the re-deposition fractions predicted by the models are relatively close, but perhaps a bit lower, than the experimental measurements. This is the regime in which W atoms are ionized many Larmor radii away from the surface, suggesting that non-local re-deposition, which is not included in either model, may be an important physics mechanism. In contrast, at low values of λ_{iz}/ρ_w and $\lambda_{iz}/\lambda_{sh}$, the predicted re-deposition fractions are higher than the experimental measurements. This discrepancy may be due to the density drop within the presheath itself, which is also not included in the either

model. Neglecting this effect would result in an under-estimation of λ_{iz} and thus an over-estimation of f_{redep} . Preliminary ERO modeling results, however, indicates that neglecting the pre-sheath density drop produces a relatively small change to the W re-deposition fractions [Guterl 19].

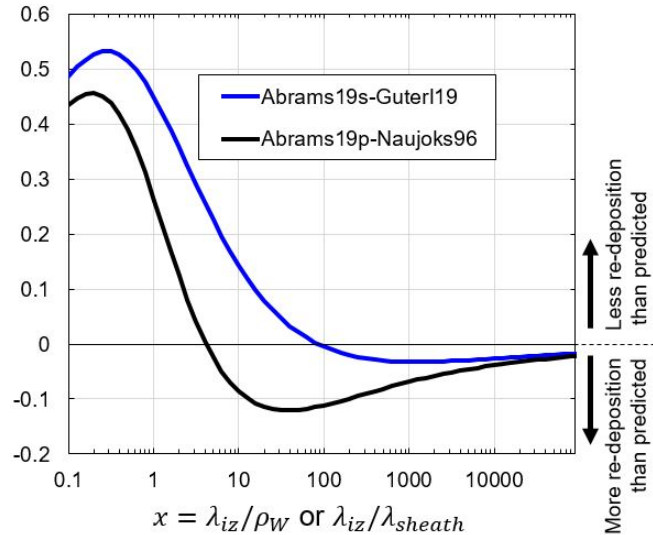


Fig. 4.11: Deviations of prompt re-deposition scalings from experimental measurements of W^+ re-deposition.

The experimental measurements also do not include re-deposition from W charge states higher than W^+ , which may be significant if a large fraction W is ionized within the pre-sheath, i.e., $\lambda_{iz}/\lambda_{sh} \ll 1$. Because the Guterl19 model does include this effect, it is perhaps not surprising that a deviation from the Abrams19s curve is observed in this regime. However, measured re-deposition fractions are lower than even the Naujoks96 model, which does not include these sheath effects. This discrepancy may be due to the fact that the Naujoks96 formulation also ignores decrease in the W ion gyro-radius at charge states higher than W^+ , which may cause W ions that would have re-deposited as W^+ ions to escape as ions of W^{2+} or higher. Dedicated experiments with well-controlled scans of λ_{iz} , λ_{iz} , and ρ_W , as well as supplemental measurements of W III lines are planned to deconvolve these effects, but unfortunately due to external factors could not be completed in time for this report.

Assessment of Carbon Impurity Content of QH-mode Experiments on DIII-D

Analysis Lead(s): Brian Grierson

Important conclusions from research on carbon content in QH-mode include:

- The highest carbon Z_{eff} observed in QH-mode experiments is with counter-current or near-zero neutral beam injected torque, and the lowest Z_{eff} is with co-current neutral beam injection
- A smaller outer gap generally increases the carbon Z_{eff} , and more so for operation in reversed plasma current (typically for high counter-current neutral beam injection)
- Erosion of around the bolt pattern in the upper divertor appears to be a source of enhanced carbon content, but is difficult to isolate due to frequent operation with the strike point at this position in the database
- For upcoming QH-mode experiments, high priority is placed on breaking the simultaneous occurrence of outer strike positioning on the bolt pattern together with balanced double null operation to isolate the roles of the source and magnetic topology on the impurity content.

A massive database of QH-mode experiments has been compiled with the goal of connecting the wall to the core plasma, identifying the operating conditions most prone to high levels of the intrinsic carbon impurity in preparation for an upcoming experiment on DIII-D in the Core-Edge Integration Task Force (CEITF). Although it has been shown previously that not all QH-mode plasmas have an intrinsically high (i.e. ELM-free like) impurity confinement [Burrell 2005, Grierson 2014, Grierson 2015, Chen 2020], it is worth understanding which conditions lead to the typically high carbon content of QH-mode plasmas to determine if the high Z_{eff} is a condition that eases access or sustainment. These conditions with high carbon content are being targeted for active wall conditioning with the PPPL boron powder dropper in experiments in FY20-21.

Discharges from all QH-mode experimental days since 2008 have been gathered, totalling 2,089 plasma shots of duration longer than one second with an accumulated 400,000 data points for each quantity ($I_p, B_T, q_{95}, \text{power}, \text{shape parameters}, Z_{\text{eff}}, \text{etc.}$) on a 20 ms time base. All discharges have been collected regardless of the discharge state (L- and H-mode phases, coherent EHO, broadband EHO, wide-pedestal, ELMs, etc...) for the broadest possible survey. In some cases, QH-mode experiments exhibit high levels of the intrinsic carbon, including Z_{eff} approaching 6, while at the same time do not exhibit rapid rises in radiation or metallic impurities levels. Dedicated impurity transport experiments have concluded that the high levels of impurities are not necessarily caused by long impurity confinement times, which may be comparable to ELMy H-modes. This indicates that a carbon source is the likely culprit for the high carbon content. The following operational parameters are suspected to influence the intrinsic carbon levels in DIII-D plasmas; (i) The ctr- I_p NBI fast-ion losses that are capable of producing strong wall erosion, identified by the injected torque, T_{inj} , in the toroidal direction multiplied by the sign of the toroidal plasma current, $\text{sgn}(I_p)$, and exacerbated by operation with low plasma current and large fast-ion orbits. (ii) The plasma-wall gap on the outboard midplane, which, when small, produces interactions of the plasma and fast ions with the outer bumper limiters, also exacerbated by low plasma current and large fast-ion orbits. (iii) The position of the

strike point with respect to regions of high erosion and damage surrounding the bolt holes that secure the graphite tiles in the upper divertor. Our database indicates that all of these factors may be at play in determining the carbon content of QH-modes, but not necessarily with the expected trends from physical principles. Counter-current NBI is broadly associated with higher carbon content, but does not scale with the magnitude of counter torque; rather the highest carbon content is at low net injected (near zero) torque. The outer wall gap may play a role in the carbon content, however a binary relationship with respect to the sign of plasma current is seen rather than a linear scaling. The upper divertor bolt holes may play a role in the carbon content, however the statistics remain low and insufficient to draw a conclusive answer. However, the variation with magnetic balance indicates that the balanced double null has the highest impurity content, which may be attributed to weak high-field-side impurity expulsion from the EHO and other fluctuations in this shape.

Counter-current Neutral Beam Injection

One known phenomenon that can increase the plasma-wall interaction is by injecting neutral beams in the direction opposite to the plasma current ($\text{ctr-}I_p$), producing fast-ions that are born with an orbit shift that is radially outwards with a higher probability of interacting with the first wall. A survey of all QH-mode experiments produces a trend that is consistent with this phenomenon, shown in Figure 4.4.1, whereby discharges that use $\text{ctr-}I_p$ NBI have, on average, a higher envelope of Z_{eff} observed. However, it is worth noting that the highest values of Z_{eff} are not at the maximum $\text{ctr-}I_p$ NBI, but rather at the lowest absolute torque. While reducing the plasma current also increases the fast-ion orbit width, which would likely produce a higher fast-ion loss with lower I_p , including the signed value of the plasma current scaling (T_{inj}/I_p) does not reveal a clear trend or change in the impact of this metric.

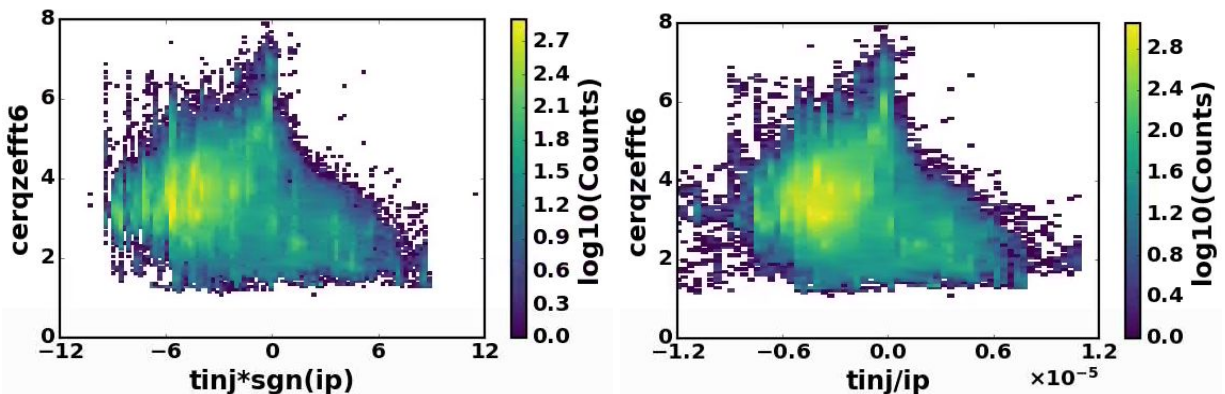


Fig. 4.4.1: Histogram showing carbon contribution to Z_{eff} as a function of torque w.r.t. I_p and torque scaled with $1/I_p$ (note factor of 10^{-5} on x-axis). The highest Z_{eff} is observed at low torque. The carbon Z_{eff} does not scale directly proportional to the amount of $\text{ctr-}I_p$ injection. Color scale is \log_{10} of counts in the database.

Outer Wall Gap

Close proximity to the plasma wall is beneficial for stability, but raises the level of plasma-wall interaction. Furthermore, outer gap variation in QH-modes has long been known to affect the interaction with coherent EHOs, producing a drag on the wall, and used for study of harmonic mode character. It is known that injection of midplane counter-current neutral beams into a plasma with a small plasma-wall gap will cause prompt losses to interact directly with the DIII-D bumper limiter. Therefore, we expect that as the plasma-wall gap is reduced, moving the plasma close to the wall, that the intrinsic carbon density will be raised due to sputtering. This database of QH-mode experiments shown in Figure 4.4.2 reveals a potential trend to increase with the smallness of the outer gap in isolation, however with a large range of outer gap associated with a large range of carbon Z_{eff} . When separated into operation with co- I_p and ctr- I_p NBI, a clearer trend emerges; when reversed plasma current is used and the outer gap is small, the carbon content is maximised as expected from the principles of ctr- I_p NBI producing direct wall interactions.

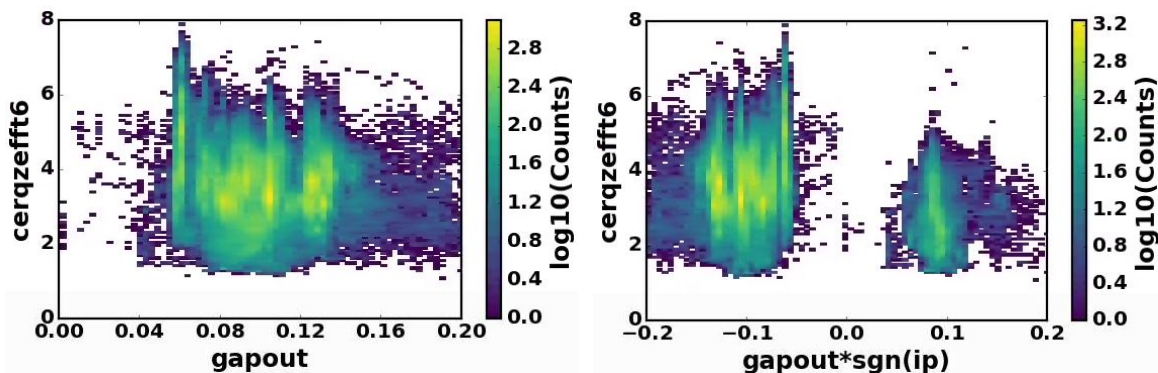


Fig. 4.4.2: Variation of carbon Z_{eff} with plasma-wall gap, and separated by positive and negative plasma current operation. Weak variation is seen with absolute wall gap, but a grouping with higher Z_{eff} is seen when the plasma current is taken into account. Color scale is \log_{10} of counts in the database.

Graphite Tile Bolt Holes

A final consideration for the impurity content of QH-mode plasmas comes from examination of the graphite tiles in the upper divertor and erosion around the bolt holes that has occurred over many years of DIII-D operation. QH-mode plasmas are often operated in a nearly balanced double null (DN) configuration with both the upper and lower strike points placed in a position to maximize pumping, which reduces the plasma density and facilitates robust QH-mode access at low collisionality. However, a balanced double null with the strike point at the entrance to the upper pumping plenum places the strike point and the heat and particle flux patterns directly on the 137 cm radius toroidal bolt pattern, seen in Figure 4.4.3. Furthermore, as with ELMs, MHD modes such as the EHO and turbulent fluctuations are predominantly ballooning-like transport phenomena, and operation in a balanced double null can isolate the high-field side (HFS) of the magnetic flux surface from SOL flows and perturbations. A quiescent inner scrape-off layer in

the balance double null can facilitate main-plasma and impurity fueling from the inboard, as seen with radiative divertor operation, and serve as a potential pathway for impurity contamination.

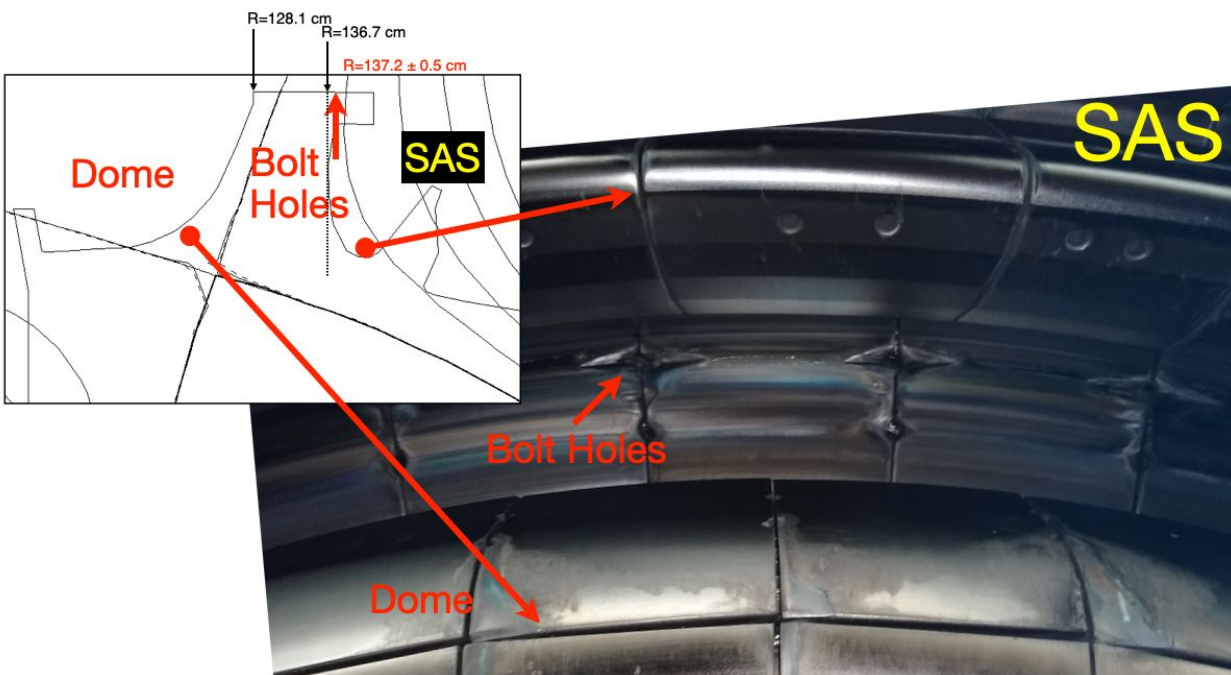


Fig. 4.4.3: Image of the DIII-D upper divertor showing the upper divertor outer bolt holes at 137.2 cm. The SAS and dome are also seen.

One clear example of the impact of moving the strike point across the bolt pattern has been identified that produced significant plasma-material interaction and carbon influx, shown in Figure 4.4.4. DIII-D discharge 153286 was begun as an upper single null (USN) plasma with the strike point near the dome, and moved radially outwards as the magnetic balance was changed to nearly balanced double null (DN). In this case, the transition to magnetic balance as the strike point is placed on the bolt pattern results in a rapid carbon influx, such as a solid piece of the graphite carbon being removed from the tile, or encountering a region of high erosion. Shown in Figure 4.4.4(a) is the magnetic balance, which approaches a double null (dR_{sep} within 1 cm of zero) near the same time that the upper outer strike point (Figure 4.4.4(b)) approaches and touches the bolt hole radius (137.2 cm). Upon reaching the bolt pattern, small C III emission spikes are visible in Figure 4.4.4(c) prior to 1.5 sec, followed by a massive increase in C II and C III emission and nearly instantaneous jump in the line averaged plasma density and core carbon Z_{eff} shown in Figure 4.4.4(d). This plasma nearly disrupts. The roles of magnetic balance and strike-point location are difficult to disentangle since an overwhelming number of QH-mode plasmas run with magnetic configuration similar to this case, which is generally considered to be advantageous for high performance plasmas with strong shaping in a pumping position. Progress on disentangling the dependence of Z_{eff} on dR_{sep} and the outer strike point position is a high priority and may motivate replacement of the upper divertor tiles.

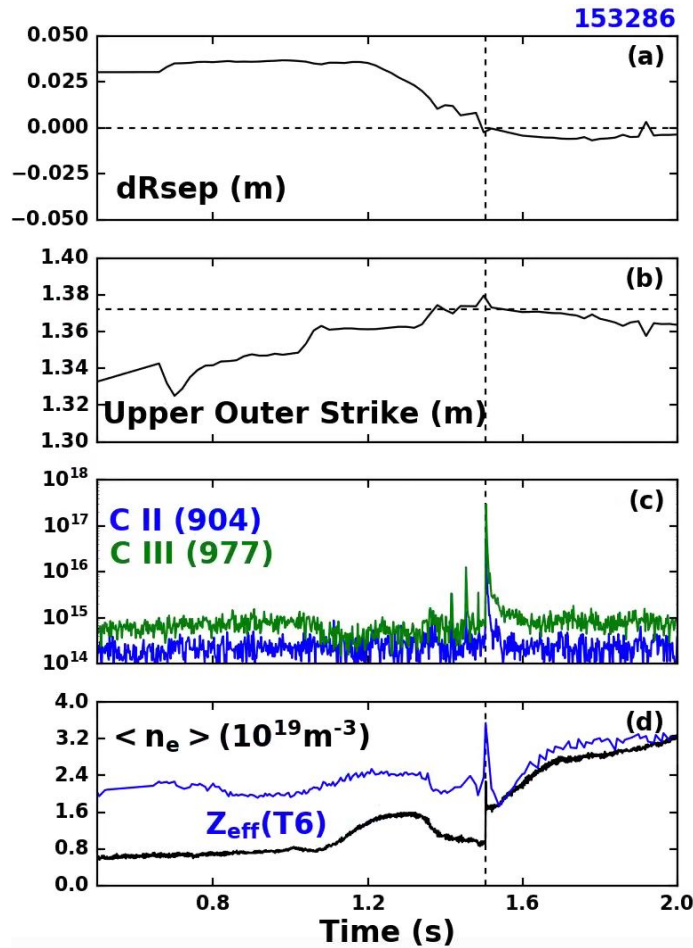


Fig 4.4.4. Time history of impurity sourcing as a QH-mode discharge that crosses magnetic balance and places strike point on the upper divertor bolt holes at $t=1.505$ seconds. (a) Magnetic balance dR_{sep} and zeroline denoting balanced DN. (b) Major radius of the upper outer strike point and $R=1.372$ m indicating the bolt pattern. (c) Carbon emission from SPRED (log scale). (d) Line averaged density and carbon Z_{eff}

Examining our database of QH-mode experiments, the trend with upper outer strike point is difficult to determine due to the high occurrence of discharges and time slices operating in this position. However, there is a reasonable variation in the magnetic balance. A histogram of the QH-mode operating space is shown in Figure 4.4.5 which displays the occurrence of outer strike line major radius (r_{vsou}) and magnetic balance dR_{sep} ($drsep$) in the database. QH-mode operation is intensely populated with balanced double null ($drsep \sim 0$) with the outer strike point placed on the upper divertor tile bolt holes ($r_{vsou} \sim 1.37$).

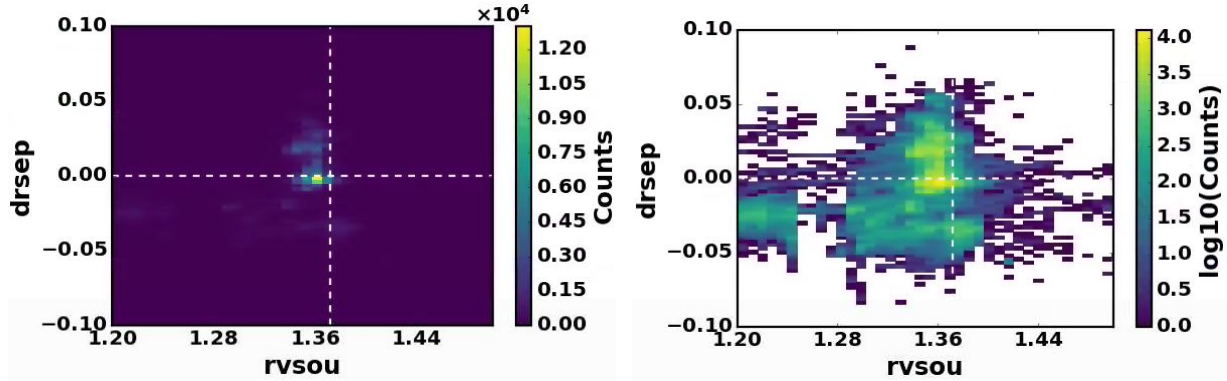


Fig. 4.4.5: Histogram of entire operating space of dr_{sep} and upper outer strike point radius (color scale is linear and \log_{10} of counts in the database). Positive dr_{sep} is upper-biased DND to USN. The database is dominated by balanced double null with strike point 1-2 cm inside of the bolt pattern. The vertical dashed line is the bolt radius.

In order to explore the potential of extracting the impact of the bolt holes on the carbon content of QH-modes, we view the carbon Z_{eff} database with both rv_{sou} and dR_{sep} parameters. Shown in Figure 4.4.6 are both histograms. First, although the data covers a relatively narrow range in outer strike point, there is a tendency of the maximum observed Z_{eff} to reduce as the strike point and 1-2 cm heat and particle flux width is pulled inside of the bolt pattern. A dedicated survey maintaining strong cryopumping in the lower divertor, along with active wall conditioning with boron, may alleviate the carbon source at the plate. Second, if balanced double null and quiescent HFS SOL is influencing the carbon contamination, a trend with dr_{sep} should be revealed. Indeed, it appears that operation at balanced double null, controlling dr_{sep} within 1 cm of zero, appears to produce the highest carbon Z_{eff} .

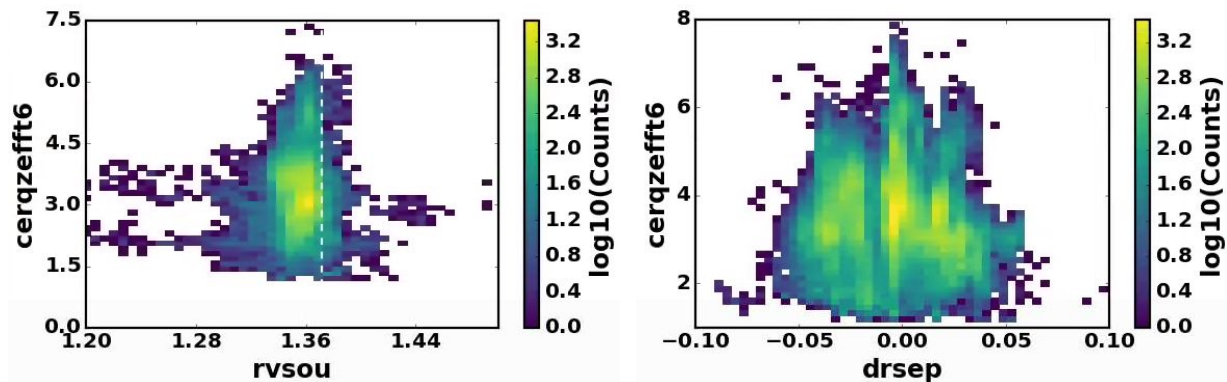


Fig. 4.4.6: Histogram of rv_{sou} for upper-biased and USN $dr_{sep} > 0.005$ m, and values of Z_{eff} . Color scale is \log_{10} of counts in the database.

Impact on Confinement

Collection of such a large database of QH-mode experiments permits us to expose trends in pedestal and overall confinement, and examine the operating points that achieve the best

performance. Detailed assessment of the pedestals of QH-mode plasmas have frequently placed the operating point on the kink/peeling boundary. In “peeling-limited” pedestals it is expected based on the EPED model that raising the density will increase the pressure, contrary to “ballooning limited” pedestals where the pressure will decrease. Our database reinforces this picture that QH-modes operate on the peeling limit with an observed correlation in Figure 4.4.7 between the pedestal pressure with density, and the highest pedestal pressures occur near the upper range of density explored. We also find that values of confinement $H_{98(y,2)}$ in excess of 1.0 can be observed over a wide range of pedestal pressure between 2-8 kPa, while showing the expected tendency of increased confinement with higher pedestal pressure.

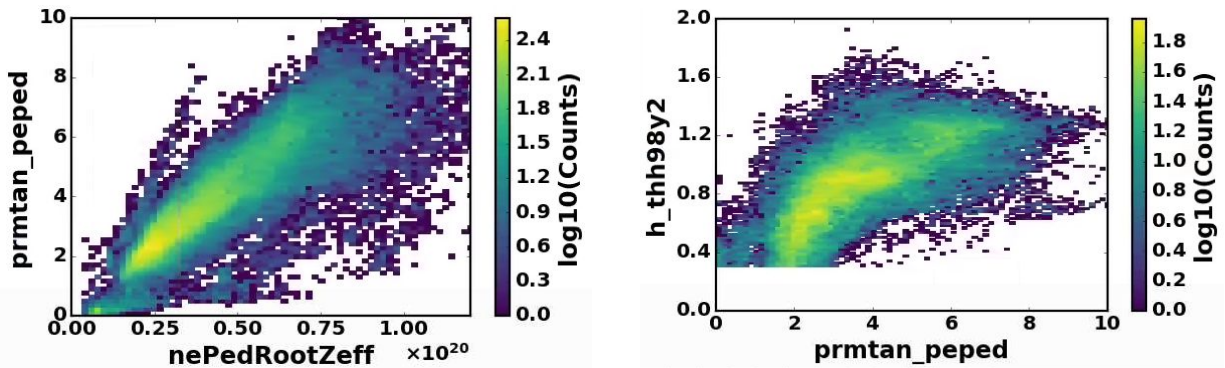


Fig. 4.4.7: (left) pedestal pressure vs. density times square root of Z_{eff} and (right) global confinement vs. pedestal pressure.

Previous studies have shown that QH-modes tend to have increased confinement as the amount of counter-current neutral beam torque is reduced towards zero. This massive database is also revealing in this trend over a very wide range of conditions. By viewing the confinement $H_{98(y,2)}$ we see that indeed this trend is robust, with high counter-current torque plasmas rarely achieving $H_{98(y,2)} > 1$, but this regime is readily observed at low counter-current or zero torque. Note that this low torque operation is also where the carbon content tends to be highest. To complete the database exploration, we also show confinement as a function of carbon Z_{eff} in Figure 4.4.8. While the trend of confinement with impurity content is less well correlated than confinement with torque, the database does reveal a scarcity of high confinement operation above convention H-mode confinement ($H_{98(y,2)} > 1$) for values of Z_{eff} less than approximately 2.5. Therefore, this reinforces the importance of understanding the role of carbon content on the performance of QH-mode experiments to break the operational correlation and expose the underlying physics.

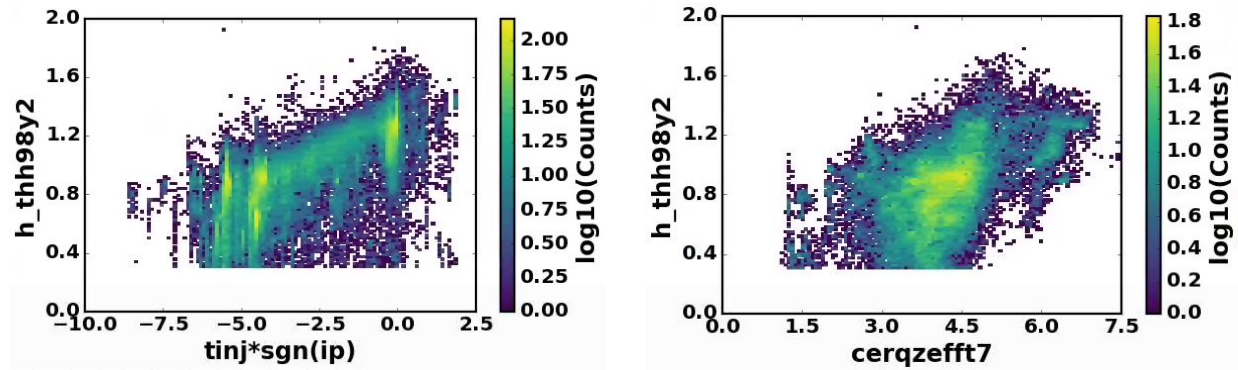


Fig. 4.4.8: (left) Confinement vs. signed torque with respect to plasma current and (right) confinement as a function of carbon Z_{eff}

For upcoming QH-mode experiments, high priority is placed on breaking the simultaneous occurrence of outer strike positioning on the bolt pattern together with balanced double null operation to isolate the roles of the source and magnetic topology on the impurity content of QH-mode plasmas.

References for Section 4

- [Abrams 2017] T. Abrams, et al., “The inter-ELM tungsten erosion profile in DIII-D H-mode discharges and benchmarking with ERO+OEDGE modeling,” Nucl. Fusion, vol. 57, pp. 056034, 2017
- [Abrams 2020] T. Abrams et al., “Measurements of Tungsten Net Erosion in the DIII-D Divertor via WI and WII Spectroscopy and Comparison to Re-deposition Models,” Nucl. Mater. Energy in preparation.
- [Bortolon 2019] A. Bortolon et al., “Real-time wall conditioning by controlled injection of boron and boron nitride powder in full tungsten wall ASDEX Upgrade,” Nucl Mater Energy, vol. 19, pp. 384–389, May 2019
- [Bortolon 2020] A. Bortolon, R. Maingi, M. Umansky, “Impurity Powder Dropper Workshop”, <https://sites.google.com/pppl.gov/ipdws2020>, 2020
- [Brezinsek 2015] S. Brezinsek and JET-EFDA contributors, “Plasma-surface interaction in the Be/W environment: Conclusions drawn from the JET-ILW for ITER,” J. Nucl. Mater. vol. 463, pp. 11-21, 2015
- [Burrell 2005] K.H. Burrell, et. al., “Advances in understanding quiescent H-mode plasmas in DIII-D”, Phys. Plasmas 12, 056121, 2005

- [Buzhinskij 1997] O. I. Buzhinskij and Y. M. Semenets, "Review of in Situ Boronization in Contemporary Tokamaks," *Fusion Technol*, vol. 32, no. 1, pp. 1–13, Aug. 1997
- [Chen 2020] X. Chen, et. al., "Expanding the parameter space of the wide-pedestal QH-mode towards ITER conditions", *Nucl. Fusion* 60 092006, 2020
- [Donovan 2018] D.C. Donovan et al., "Utilization of outer-midplane collector probes with isotopically enriched tungsten tracer particles for impurity transport studies in the scrape-off layer of DIII-D," *Rev. Sci. Instrum.* vol. 89, pp. 101115, 2018
- [Effenberg 2017] F. Effenberg et al., "Numerical investigation of plasma edge transport and limiter heat fluxes in Wendelstein 7-X startup plasmas with EMC3-EIRENE," *Nucl Fusion*, vol. 57, no. 3, p. 036021, Mar. 2017
- [Elder 2019] J.D. Elder et al., "Evidence of near-SOL tungsten accumulation using a far-SOL collector probe array and OEDGE modelling in the DIII-D metal rings L-mode discharges," *Nucl. Mater. Energy* vol. 19, pp. 287–294, 2019
- [Grierson 2014] B.A. Grierson, et. al., "Response of impurity particle confinement time to external actuators in QH-mode plasmas on DIII-D", *Nucl. Fusion* 54 114011, 2014
- [Grierson 2015] B.A. Grierson et. al., "Impurity confinement and transport in high confinement regimes without edge localized modes on DIII-D", *Phys. Plasmas* 22 055901, 2015
- [Johnson 2019] C.A. Johnson et al., "Advances in neutral tungsten ultraviolet spectroscopy for the potential benefit to gross erosion diagnosis" *Plasma Phys. Control. Fusion* vol. 61, pp. 095006, 2019
- [Kirscher 2019] A. Kirschner, S. Brezinsek, A. Huber, A. Meigs, G. Sergienko, D. Tskhakaya, D. Borodin, M. Groth, S. Jachmich, J. Romazanov et al., "Modelling of tungsten erosion and deposition in the divertor of JET-ILW in comparison to experimental findings" *Nucl. Mater. Energy* vol. 18, pp. 239–244, 2019
- [Lipschultz 2005] B. Lipschultz, D.G. Whyte and B. LaBombard, "Comparison of particle transport in the scrape-off layer plasmas of Alcator C-Mod and DIII-D" *Plasma Phys. Control. Fusion*. vol. 47, pp. 1559–1578, 2005
- [Nagy 2018] A. Nagy et al., "A multi-species powder dropper for magnetic fusion applications," *Rev Sci Instrum*, vol. 89, no. 10, p. 10K121, Oct. 2018
- [Pitts 2019] R.A. Pitts et al., "Physics basis for the first ITER tungsten divertor" *Nucl. Mater. Energy* vol. 20, pp. 100696, 2019

[Putterich 2010] T. Putterich et al., “Calculation and experimental test of the cooling factor of tungsten” *Nucl. Fusion* vol. 50, pp. 025012, 2010

[Rudakov 2005] D.L. Rudakov et al., “Far SOL transport and main wall plasma interaction in DIII-D” *Nucl. Fusion* vol. 45, pp. 1589–1599, 2005

[Senichenkov 2019] I.Y. Senichenkov et al., “On mechanisms of impurity leakage and retention in the tokamak divertor,” *Plasma Phys. Control. Fusion*, vol. 61, pp. 045013, 2019

[Stangeby 2011] P.C. Stangeby and A.W. Leonard, “Obtaining reactor-relevant divertor conditions in tokamaks,” *Nucl. Fusion*, vol. 51, pp. 063001, 2011

[Unterberg 2020] E.A. Unterberg et al., “Localized divertor leakage measurements using isotopic tungsten sources during edge-localized mode-y H-mode discharges on DIII-D,” *Nucl. Fusion*, vol. 60, pp. 016028, 2020

[Wampler 2017] W.R. Wampler et al., “Measurements of tungsten migration in the DIII-D divertor,” *Phys. Scr.*, vol. T170, pp. 014041, 2017

[Winter 1996] J. Winter, et. al., “Wall conditioning in fusion devices and its influence on plasma performance,” *Plasma Phys. Control Fusion*, vol. 38, no. 9, pp. 1503–1542, Sep. 1996

[Wong 1992] C.P.P. Wong, et. al., “Divertor materials evaluation system at DIII-D”, *J. Nucl. Mat.* vol. 196-198, 1992

[Zamperini 2020] S.A. Zamperini et al., “Reproduction of collector probe deposition profiles using the far-SOL impurity transport code 3DLIM,” *Nucl. Mater. Energy* submitted

Acknowledgements

This report was only possible due to the many contributions of the DIII-D, NSTX-U and Alcator C-Mod teams. This material is based upon work supported by the U.S. Department of Energy, Office of Science, Office of Fusion Energy Sciences, using the DIII-D National Fusion Facility, a DOE Office of Science user facility, under Award DE-FC02-04ER54698; using Alcator C-Mod, a DOE Office of Science user facility, under Award DE-FC02-99ER54512; and using NSTX and NSTX-U, a DOE Office of Science user facility, under Award DE-AC02-09CH11466. Additional work was supported under DOE grants DE-SC0014264, DE-AC05-00OR22725, DE-SC0019256. Portions of this research were performed under the auspices of the US DOE by Lawrence Livermore National Laboratory under Contract DE-AC52-07NA27344. This research used resources of the National Energy Research Scientific Computing Center (NERSC), a U.S. Department of Energy Office of Science User Facility operated under Contract No. DE-AC02-05CH11231. Part of the data analysis was performed using the OMFIT integrated

modeling framework, O. Meneghini, et. al, "Integrated modeling applications for tokamak experiments with OMFIT", Nucl. Fusion 55, 083008, 2015.

Disclaimer

This report was prepared as an account of work sponsored by an agency of the United States Government. Neither the United States Government nor any agency thereof, nor any of their employees, makes any warranty, express or implied, or assumes any legal liability or responsibility for the accuracy, completeness, or usefulness of any information, apparatus, product, or process disclosed, or represents that its use would not infringe privately owned rights. Reference herein to any specific commercial product, process, or service by trade name, trademark, manufacturer, or otherwise does not necessarily constitute or imply its endorsement, recommendation, or favoring by the United States Government or any agency thereof. The views and opinions of authors expressed herein do not necessarily state or reflect those of the United States Government or any agency thereof.

Supplement to the FY20 JRT : Core to Edge Investigation of Impurity Transport in Tokamak Plasmas

Direct Contributions to JRT Supplement from: N. Howard¹, T. Abrams², F. Scotti³, B. Grierson⁴, A. Bortolon⁴, B. Wilcox⁵, F. Sciortino¹, T. Rhodes⁶, G. Wang⁶

Contributed to Mini-Proposal and Experiment: T. Odstrcil², F. Effenberg⁴, C. Lasnier³, C. Paz-Soldan⁷, A. Mclean³, E. Hinson⁸, G. Mckee⁸, B. Victor³

¹MIT Plasma Science and Fusion Center, Cambridge, Massachusetts, USA

²General Atomics, San Diego, California, USA

³Lawrence Livermore National Lab, Livermore, California, USA

⁴Princeton Plasma Physics Lab, Princeton, New Jersey, USA

⁵Oak Ridge National Laboratory, Oak Ridge, Tennessee, USA

⁶University of California - Los Angeles, Los Angeles, California, USA

⁷Columbia University, New York, New York, USA

⁸University of Wisconsin - Madison, Madison, Wisconsin, USA

FY20 Joint Research Target: Milestone Statement

Accumulation of impurities, ranging from light ions (helium ash) to high-Z (such as tungsten) can adversely impact the reactivity of the fusion core through fuel dilution and excessive radiation. To inform operation of ITER and beyond, transport of impurities from the divertor to the core will be studied, particularly as parameters that are expected to impact the relative balance of turbulent versus neoclassical impurity transport are varied. Experiments will introduce a wide range of low to high Z impurities, while turbulence and transport properties are documented. Integrated modeling tools will be used to validate theoretical models and interpret the physical mechanisms of transport in the core, divertor, and scrape-off layer.

JRT Supplement Introduction:

The JRT report submitted at the end of FY20 included the analysis of 9 distinct datasets obtained from 3 major US facilities, DIII-D, NSTX/U, and Alcator C-Mod. The report was organized by distinct plasma regions spanning the core, pedestal, and SOL/Divertor region. As with most present day experiments, analysis of impurities in this report focused on particular plasma regions and used a limited set of impurity measurements to draw conclusions. However, as discussed in the JRT report, we recognize that impurity transport in fusion devices needs to be investigated with a more holistic approach that **simultaneously** considers impurity transport and sources spanning from the core to the edge/divertor. As part of the FY20 JRT, two run days on the DIII-D tokamak were allocated to perform experiments aimed at simultaneously studying impurity transport in both the core and edge of ITER relevant plasmas.

Due to delays in DIII-D operation, these experiments were pushed until September of 2020 and as a result, none of the data obtained in these experiments were included in the JRT report submitted at the end of FY20. This supplement is meant to complement the submitted report and describes the current state of the analysis of these experiments. The results presented here should not be viewed as final but represent a glimpse into ongoing analysis that will be included in part at the 2020 IAEA Fusion Energy Conference presentation on the FY20 JRT.

Section 1.

Description of Experiments and Identification of Datasets

JRT Experiment Objectives

As stated above, the objective of the JRT experiments was to simultaneously collect impurity transport data that spanned from the core to the divertor in ITER-relevant plasma conditions to enable validation of core and edge transport models and to provide an integrated look at impurity transport across the plasma. Two run days were allocated for these experiments and two target conditions were selected for study. The target conditions were an ITER similar shape (ISS) plasma operated with RMP ELM suppression and Electron Cyclotron Heating (ECH) and the Steady State Hybrid discharge. Experimental targets were based on discharges 175696 (ISS) and 161409 (SS-Hybrid) and were chosen due to their relevance to the future operation of ITER. The high level goals of this experiment were to:

1. Collect validation quality impurity transport data in the core/pedestal representing a scan of impurity Z from He to W.
2. Collect fluctuation data to enable multi-channel, multi-field model validation in the core/pedestal.
3. Collect simultaneous impurity measurements and 2-D n_e and T_e data in the SOL/divertor to enable edge modeling.

To achieve these goals, the approach of these experiments was to establish a target discharge and repeat that condition a sufficient number of times to gather different datasets. Since these repeat discharges would be (ideally) statistically identical, the data obtained in all repeat shots could be viewed as representative of the target condition. This approach allowed us to introduce different impurities shot to shot and to collect a wide range of unique datasets that were impossible to assemble in a single plasma discharge. In the short term, these data will allow for the validation of leading models of impurity transport in ITER relevant conditions. A longer term goal of this data is to enable studies focused on core-edge integration (coupling of core and edge models) of impurity transport analysis and eventual predictive capability.

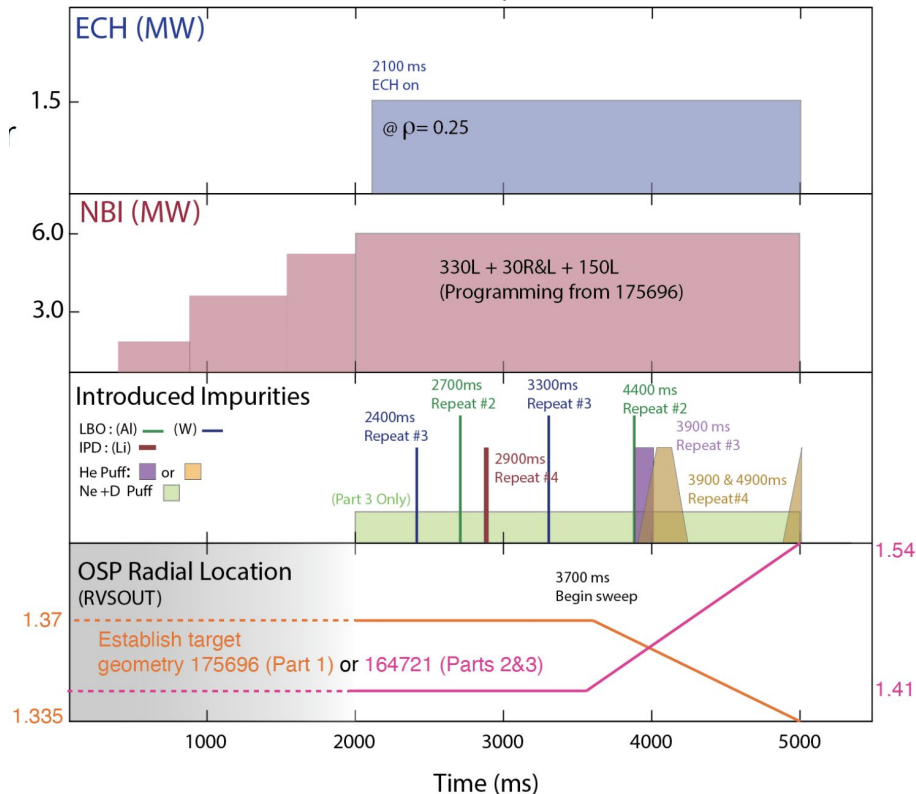


Figure 1.1 Diagram used during experimental planning to demonstrate the programming for 4 repeat discharges of the target ISS condition.

Experimental Data Obtained

A brief overview of key measurements obtained in these experimental conditions is listed here:

1. CER documented: He, Li, C (C-VI, C-IV), F, Al, Ca, and main ion (D) densities
2. SPRED (VUV) measured lines from all of the introduced impurities
3. BES measured n_e fluctuation in the range $\rho = [0.5 \text{ to } 1.0]$
4. DBS performed a multi-point k scan from low to intermediate k
5. MDS and TangTV measured partially stripped carbon emission in edge
6. SXR arrays (64 chords) measured Al, Ca, and W injections
7. Probe data, IRTV, 2-D Divertor Thomson data collected
8. Wide range of other measurements that enable accurate equilibrium reconstruction and power balance collected

The experiment was originally planned for 5 target conditions, 3 in ISS and 2 in SS-hybrid but machine conditions limited our scope to fully documenting a single condition, with the addition of a complementary dataset also being collected. A comprehensive dataset was obtained in ITER Similar Shape (ISS) with RMP ELM suppression, ECH, and an Outer Strike Point (OSP) sweep that enabled measurement of 2-D profiles with the divertor Thomson Scattering system. Due to time constraints, we decided to collect a complementary dataset that was operated with

identical conditions (ISS with RMP and OSP sweep) but with ECH disabled to demonstrate the effect of electron heating on impurity transport. This data will not be discussed in detail in this report but will be analyzed in future work. Using the impurity powder dropper (Li), gas puffing (He), and laser blow-off injection (F, Al, Ca, W), impurities with a wide range of impurity Z were introduced into the target condition and were measured using a combination soft X-ray, a VUV spectrometer, and charge exchange recombination (CER) spectroscopy tuned shot to shot to measure the specific impurity that was introduced. This combination of diagnostics measured He, C, F, Al, Ca, and W emission in the discharge conditions. Reproduction of the discharge conditions shot to shot also enabled the assembly of fluctuation profiles from repeated discharges. Beam Emission Spectroscopy (BES), Doppler Backscattering (DBS), and Correlation Electron Cyclotron Emission (CECE) data were collected that span the core ($\rho \sim 0.5$) to the top of the pedestal. Examples of preliminary analysis of the measured DBS density fluctuations and the CECE measured profile of the electron temperature fluctuations are shown in Figures 1.2 and 1.3. These measurements will be compared directly with modeling in future studies and will provide invaluable modeling constraints when simulating turbulence in the core of the discharge.

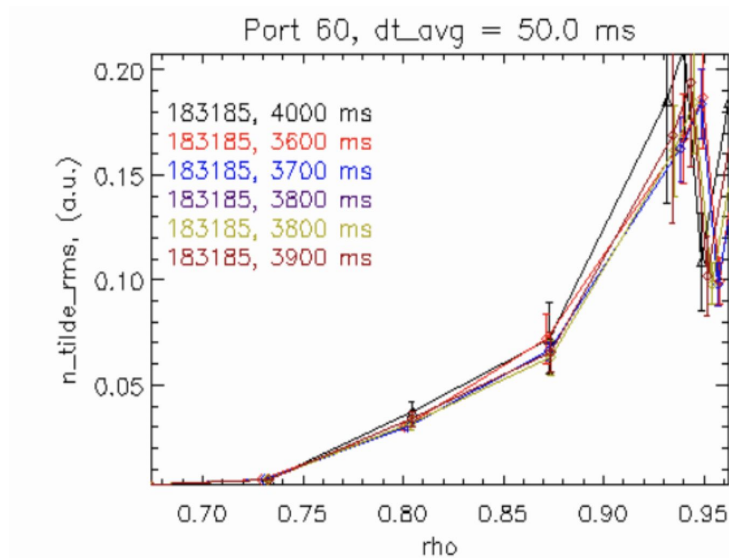


Figure 1.2 - Preliminary analysis of the DBS measured density fluctuation level from $\rho = 0.65$ to 0.95 is plotted. Different time slices of analysis are overplotted to demonstrate the steady nature of the discharge studied.

3550-3850 ms, 40-500 kHz cece8+cece2
Two different analysis methods used and shown as black and red power spectra. Red spectra are believed to be the more accurate and those are used in the profiles.

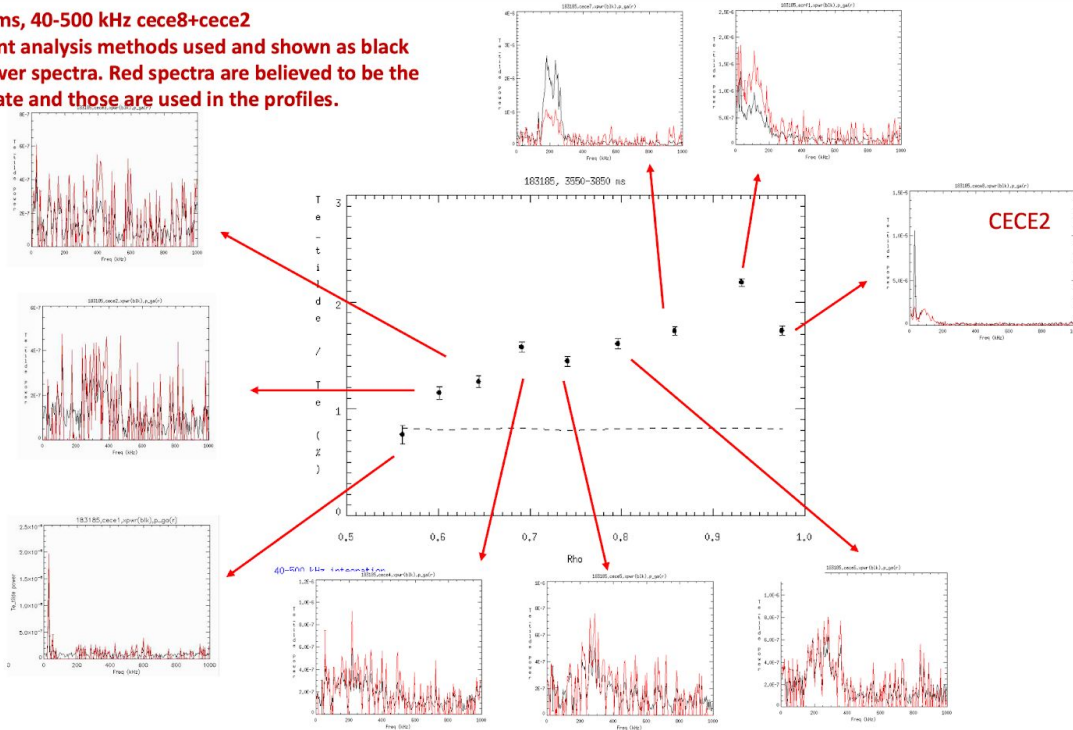


Figure 1.3 - (center) A profile of the CECE temperature fluctuation level data obtained during the experiment is shown spanning from $\sim\rho= 0.5$ to 1.0 . The power spectra corresponding to different measurement locations are shown in the corresponding plots

In the divertor region, the Tangential TV (TangTV) cameras and the MDS spectrometers were used to measure visible emission from different charge states of carbon and deuterium (CD band, C II, C III, C IV, D- α) shot to shot, providing calibrated divertor impurity emission. Furthermore, the OSP sweep across the divertor floor enabled a 2-D measurement of n_e and T_e using the divertor Thomson system. The quality of the divertor Thomson data is still under evaluation but it is expected that, combined with the spectroscopic measurements, these data will provide important constraints for future divertor modeling in these conditions.

Identification of Repeat Discharges for Study and the Target Condition for Analysis

Following the completion of the JRT experiments, a more comprehensive investigation of the discharges and data collected was performed. Fourteen discharges were found to have high quality data that warrants further analysis and therefore form the dataset documenting the ITER Similar Shape (ISS) with RMP ELM suppression, ECH, and an Outer Strike Point (OSP) sweep. The large number of repeats were primarily needed to ensure proper documentation of the introduced impurities. An additional five discharges were identified as having high quality data and representing the “no ECH version” of the base dataset. From these datasets, shot 183185 was selected as the target for analysis covered in the remainder of this supplement. Details of this discharge are provided in the following section.

Section 2.

Description of Experimental Data: Equilibrium, Profiles, and Power Balance Analysis of the Reference Discharge

Discharges executed for the JRT in the ITER-like scenario provided variations around a nominal target set of lower single null conditions in the ITER shape with the $\mathbf{B} \times \nabla B$ drift direction into the lower divertor; -2.05 T, 1.62 MA, $q_{95} \sim 3.4$ with approximately 4.3 MW feed-forward neutral beam heating and 1.5 MW of ECH producing $\beta_N \sim 1.5$. RMP ELM suppression is provided by n=3 I-coil at 4 kA amplitude. These discharges are sawtoothing, with various amounts of n=3 and n=2 tearing mode activity. The representative discharge that will serve as a reference condition for variations around this operating point was executed with diagnostics in their standard configuration; all CER spectrometers tuned to their nominal ion (carbon, deuterium), no perturbative impurity injections, and relatively long stationary conditions. This reference discharge is shown in Figure. 2.1, where long periods of ELM suppression are achieved. Early in the discharge before 3.0 seconds, an n=2 tearing mode is dominant, but then transitions to a weaker n=3 mode. The period of time between 3.5-4.0 seconds has stationary ELM suppression and the weakest core MHD. Later in time after 4.0 seconds, sporadic ELMs return concomitant with sawtooth crashes. The time period between 3.5-4.0 seconds is chosen as the stationary time window for more detailed profile, equilibrium and transport analysis using TRANSP [TRANSP].

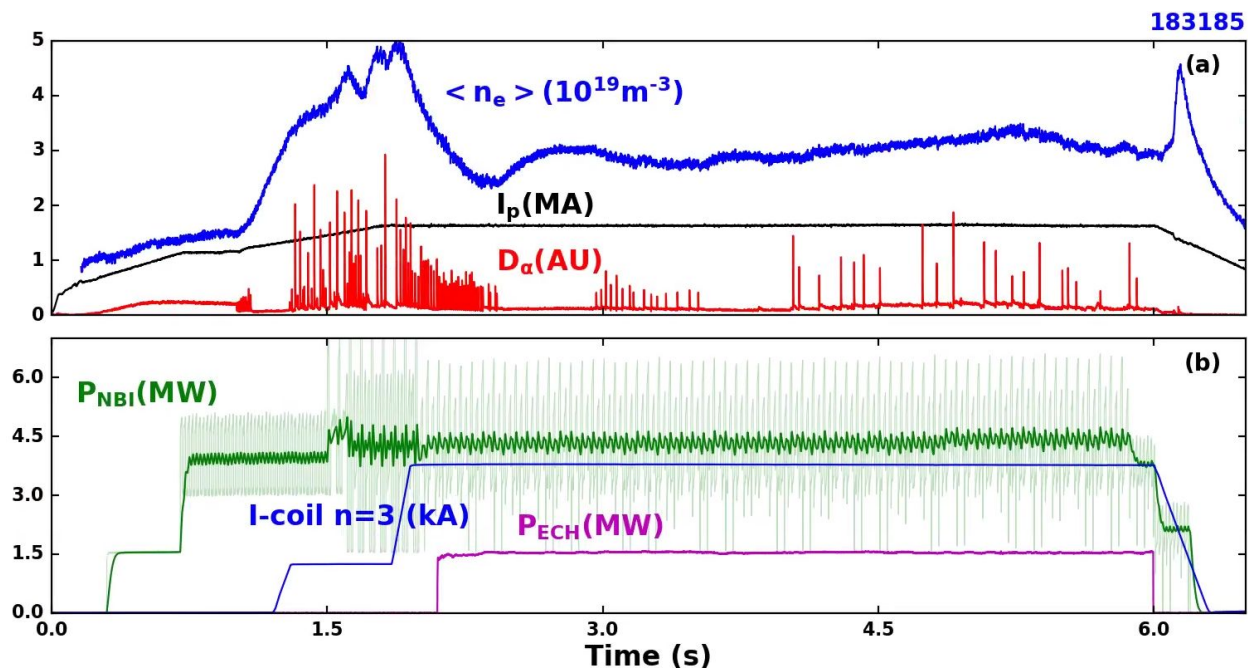


Figure. 2.1: Time history of key quantities for reference discharge displaying H-mode at 1.0 second, density pump-out due to n=3 RMP at 2.0 seconds, and

stationary periods of ELM suppression. Analysis will focus on the period of ELM suppression from 3.5-4.0 seconds.

Plasma profile fitting has been performed during the period of stationary ELM suppression shown in Figure. 2.1 using the available profile data acquired using multiple diagnostics. Electron density measured with Thomson scattering, normalized by the CO2 interferometer, and the UCLA profile reflectometer, were all combined. Thomson is currently undergoing a back calibration and thus the profile reflectometer was favored for the near-axis density profile. The selected toroidal field ($B_T = -2.05$ T) and low density well below cutoff provides high quality electron cyclotron emission (ECE) measurements spanning the full radial profile and crossing the magnetic axis. Neutral beam voltage selection, programming and modulation pattern provides high quality charge-exchange recombination (CER) spectroscopy and motional stark effect (MSE) polarization for magnetic field pitch angle measurements. Radiation was measured by the DIII-D foil bolometer system. Representative experimental data and profiles used in subsequent equilibrium constraints and transport analysis are shown in Figure 2.2. Measurements acquired provide a validation-quality data set for detailed analysis.

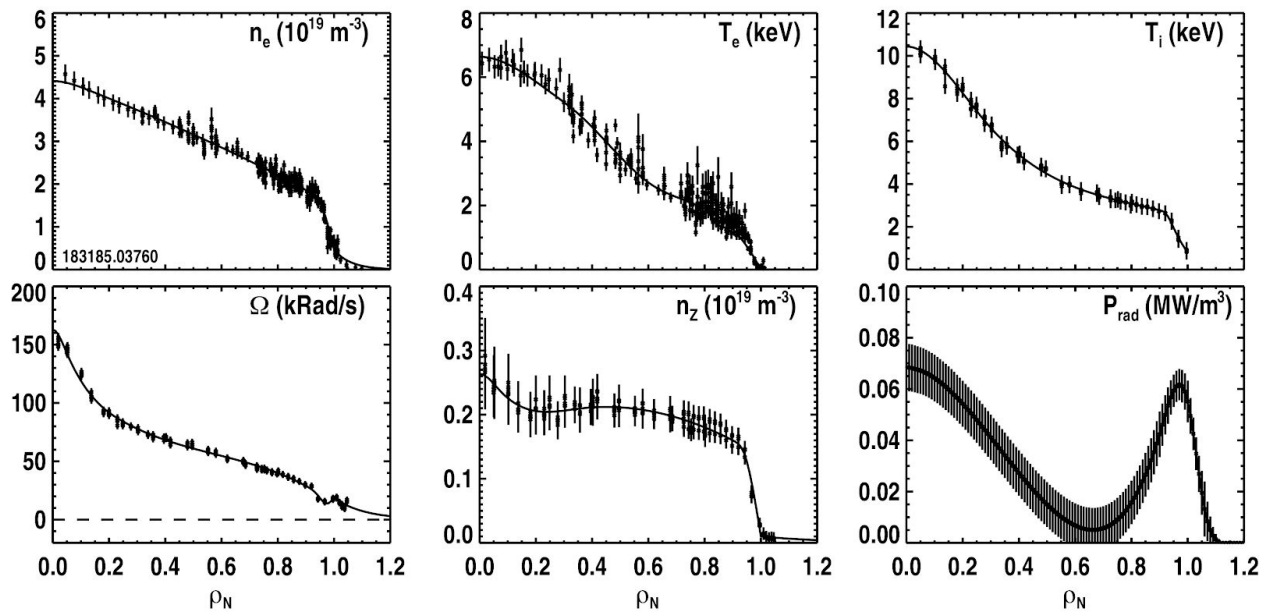


Figure. 2.2: Plasma kinetic profiles determined by multiple diagnostics for reference discharge shown in Figure. 2.1 at 3.5-4.0 sec. Electron density: Thomson scattering and profile reflectometer. Electron temperature: Thomson scattering and ECE. Ion temperature, rotation and carbon density (n_z): carbon CER. Radiated power: foil bolometer.

Kinetic equilibrium reconstruction was performed to assess the agreement between the kinetic profile reconstructions, fast particle content and EFIT reconstructions using only magnetics (EFIT01) and magnetics+MSE (EFIT02). Plasma profiles were fit and input to TRANSP simulations of the neutral beam injection, fast particle content and resistive current diffusion using Sauter resistivity and bootstrap current [Sauter 1999] in order to derive the total

(fast+thermal) pressure and relaxed current profile. The plasma rotation was used to correct the MSE pitch angles for the known effects of the radial electric field on determining the q-profile. TRANSP simulation 183185Z02 was used to constrain kinetic EFITs. This TRANSP simulation matches neutrons within 10% and EFIT01 stored energy within 1-2 %, shown in Figure. 2.3.

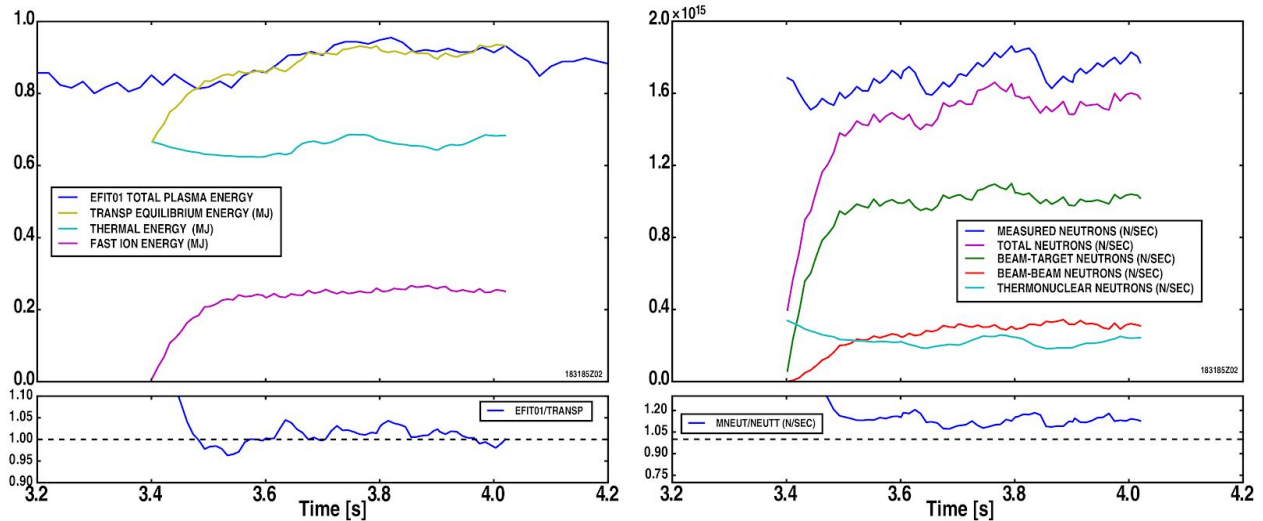


Figure. 2.3: Result of TRANSP simulations covering 3.5-4.0 seconds of stationary ELM suppressed phase. Following brief (100 ms) neutral beam build-up a good match between magnetics EFIT stored energy and neutron rate is seen.

Knotted spline basis functions for P' and FF' were used and well converged equilibria were obtained with low magnetics, MSE, pressure and current χ^2 as well as low Grad-Shafranov error. The results of a representative kinetic equilibrium is shown in Figure 2.4 and Figure 2.5. With this equilibrium we revisit the observation of an n=3 tearing mode in this reference discharge to identify the mode number and spatial location. Based on magnetics analysis, the toroidal and poloidal mode number of the 27.25 kHz fluctuation appears to be (m,n) = (4,3). Additional information is provided by fourier analysis of the ECE data, and indicates that the ECE fluctuation amplitude peaks near $\rho=0.4-0.5$. Therefore transport analysis should consider the impact of a magnetic island on profile structure in this region.

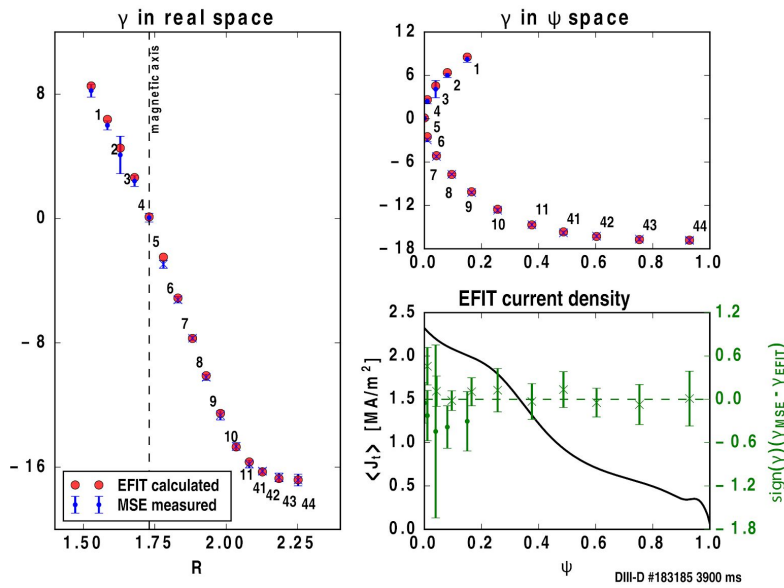


Figure 2.4: Er-corrected MSE pitch angles used to determine the magnetic axis and equilibrium q profile in the kinetic EFIT reconstruction. Good agreement is seen across the profile contributing to a low MSE χ^2 .

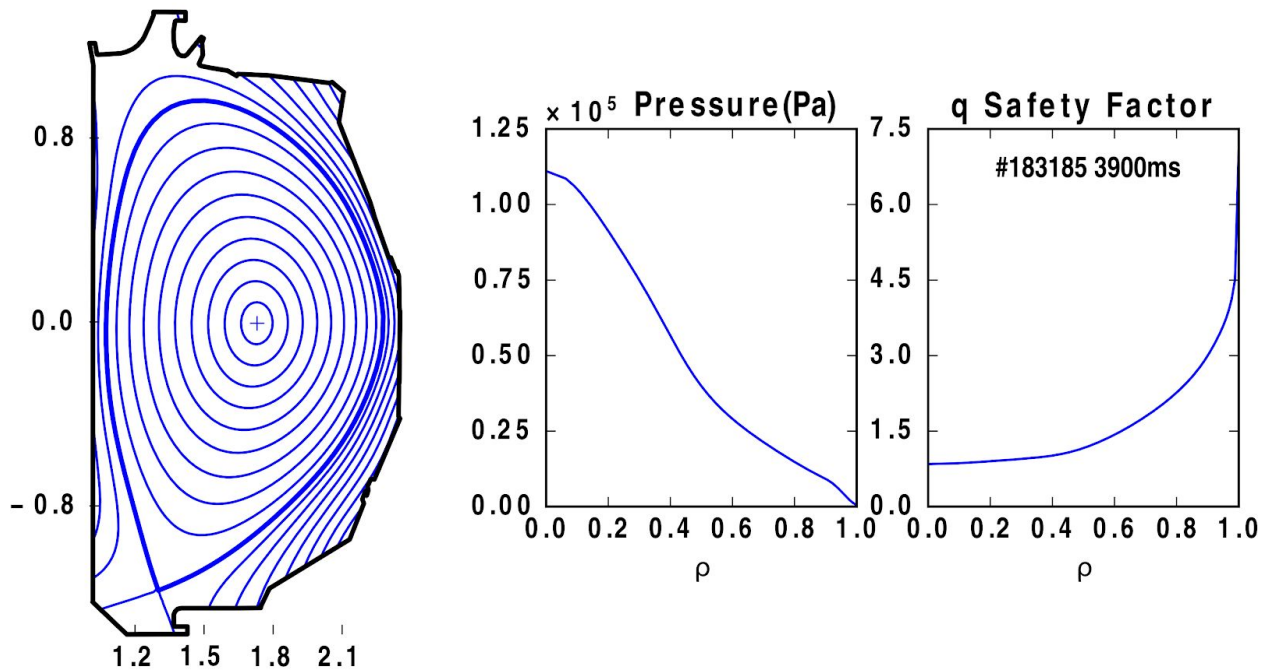


Figure 2.5: Kinetic equilibrium flux surface shape, pressure and q profile.

Having verified consistency between the measured kinetic profiles with the TRANSP neutron rates and stored energy, evaluation of power balance and assessment of the degree to which transport models capture the measured profiles can begin. TRANSP was re-run in the higher

fidelity analysis mode to improve the accuracy of the NUBEAM [Pankin 2004] Monte-Carlo statistics in the power, particle and momentum balance calculations. The results of the TRANSP simulations averaged over the stationary phase of the reference discharge are shown in Figure 2.6. As designed, these ITER-like discharges successfully produce a radial power flow profile that achieves nearly equal ion and electron power flows. Near the axis, neutral beam heating is dominant, while ECH aiming near $\rho \sim 0.3$ increases the electron heating outside of this radius, creating similar ion and electron power flow profiles. In this relatively low density DIII-D discharge, neutral beam fueling is an important component to total particle flow, which was computed with a $\tau_p = 200$ ms particle confinement time. Neutral beam torque is also shown to be significant for these conditions, as was required for achieving ELM suppression, which has an approximate (0D) $T_{inj} \sim 3.8$ Nm of injected torque, and is consistent with the radial momentum flow from NUBEAM. These radial profiles of power, particle and momentum flow are all sufficiently well behaved to continue analysis with gyrokinetic simulations and transport modeling.

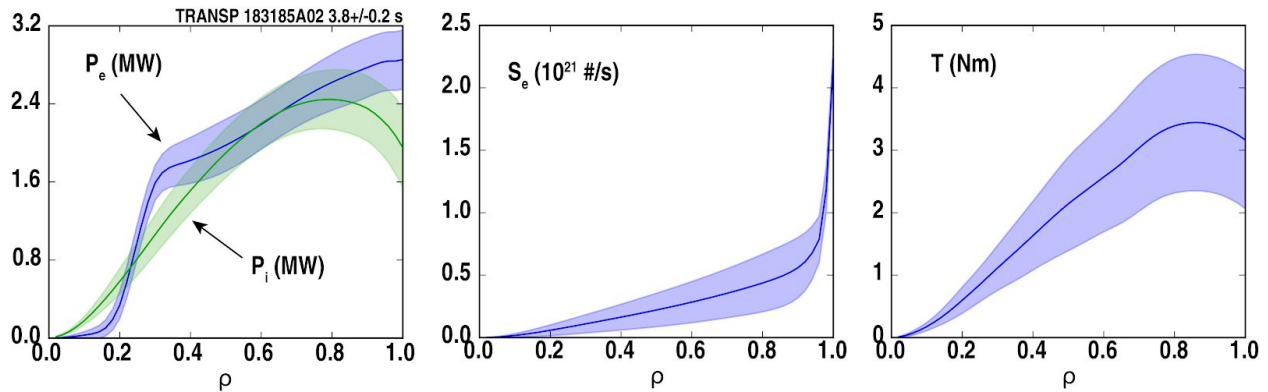


Figure 2.6: Power, particle and momentum flows determined from TRANSP analysis. Combination of NBI and ECH produces nearly equal ion and electron power flows across most of the plasma radius.

The TRANSP analysis has been extracted and converted to the uniform input for the GACODE modeling tools via the `profiles_gen` utility, resulting in an `input.gacode` file. This file contains all required parameters to perform local neoclassical, gyrokinetic and gyrofluid simulations. A graphical representation of the input profiles, scale lengths and derived quantities important for gyrokinetic simulations are shown in Figure 2.7. Here the rotation quantities $\gamma_E = -(r/q)d\omega_0/dr$ and $\gamma_p = -R_0 d\omega_0/dr$ are the EXB and rotation shearing rates, respectively. The profiles and derived scale lengths obtained in this discharge are near analytic thresholds for many of the instabilities expected to be active in ITER; across the mid-radius from $\rho \sim 0.3-0.8$ these profiles are near threshold for ETG, ITG and TEM. Of note is that even when achieving equal power flows across most of the plasma volume, sustained $T_i/T_e > 1$ exists across the radial profile. This was anticipated due to the requirement for low collisionality and RMP ELM suppression. Future studies when increased ECH power becomes available are expected to simultaneously reduce the ion/electron temperature ratio while also producing equal power flows. The use of these profiles in theory-based simulations is described in Sec. 3.

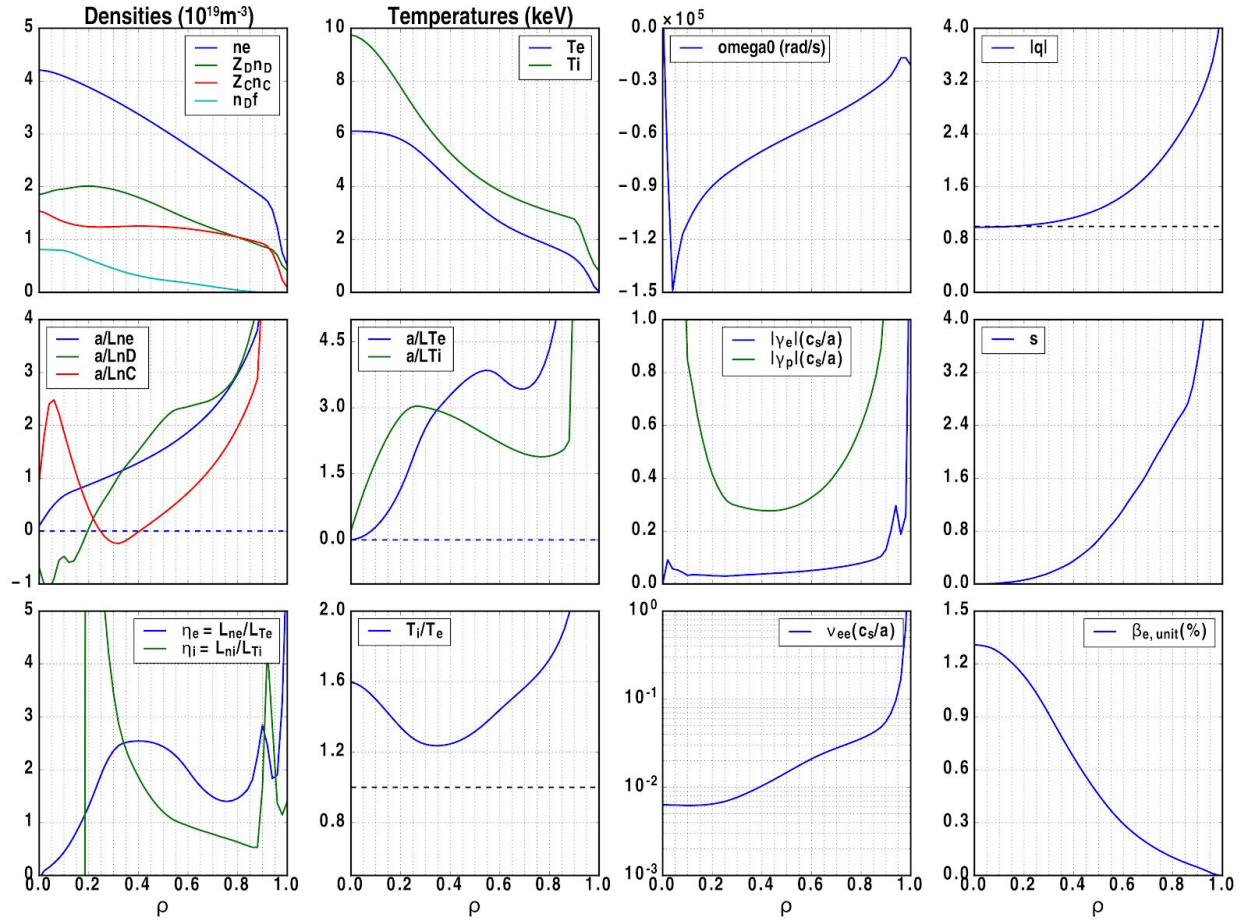


Figure 2.7: Input profiles (*input.gacode*) to the GACODE tools CGYRO, NEO and TGYRO.

Section 3.

Preliminary Experimental Analysis and Simulation Results

Edge/Divertor Measurements and Analysis

All the discharges were carried out in high triangularity shape with strike point on the floor in proximity of the entrance to the cryo pump plenum. Due to the limited diagnostic coverage at the outer strike point at this radial location, at the end of each discharge (4600-5100ms) a small strike point sweep (from 1.37 m to 1.33 m) was performed to allow for better coverage by infrared thermography, spectroscopy, and spectral imaging, as well as for the measurements of divertor profiles from the tile-mounted Langmuir probes. While ELMs were not fully suppressed in this phase, shorter intervals of ELM suppression were observed and were utilized to extract the divertor profiles. Perpendicular ion saturation current densities measured by the tile

mounted Langmuir probes (over the interval 4550-5100 ms) are plotted in Figure 3.1 for the outer and for the inner strike point as a function of normalized poloidal flux. Plasma parameters inferred from the Langmuir probe analysis also indicated both strike points to be well attached.

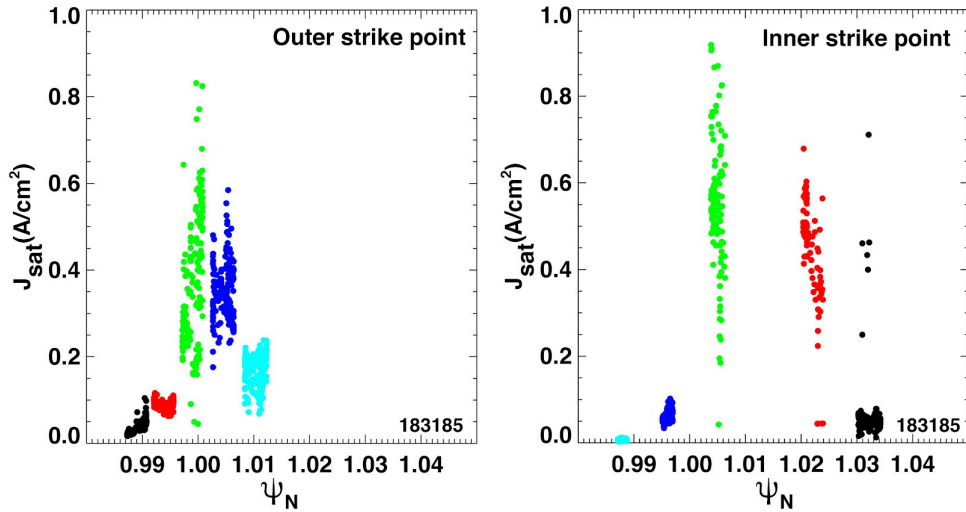


Figure 3.1: Radial profiles of perpendicular ion saturation current densities measured by the tile-mounted Langmuir probes as a function of normalized poloidal flux at outer (left) and inner (right) strike points. Values measured by different Langmuir probes are plotted in different color.

Perpendicular divertor heat flux profiles were determined from infrared thermography data analyzed with the heat transport solver THEODOR and plotted in Figure 3.2 as a function of distance from the outer and inner strike points.

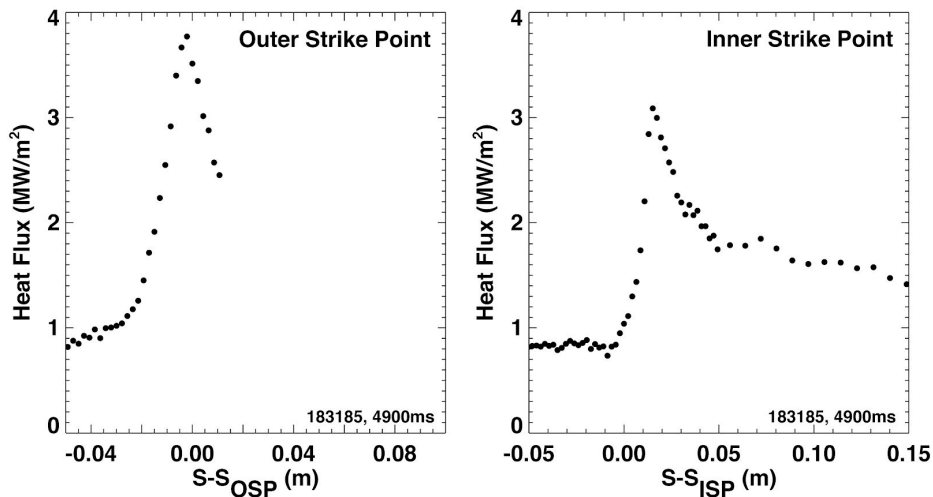


Figure 3.2: Radial profiles of perpendicular heat flux calculated from infrared thermography as a function of distance from outer (left) and inner (right) strike points for discharge 183185 at $t=4900\text{ms}$.

2D brightness measurements were performed with the TangTV cameras and 2D emissivities were reconstructed for all the lower carbon charge states: CD (Gerö band, 430 nm), C II (514 nm), C III (465 nm) and C IV (580 nm) visible emission together with deuterium Balmer α emission. An example of the reconstructed 2D emissivities for D- α , C II, C III and C IV is shown in Figure 3.3 overlaid onto an equilibrium reconstruction. As expected under these well attached divertor conditions, emissivities for all the measured carbon charged states are peaked close to the strike point. These measurements were also complemented by spectrally-resolved line-integrated brightness at each of these wavelengths acquired in repeated discharges with the MDS spectrometer shown in Figure 3.4. These measurements will be used as boundary constraints in future interpretive modeling exercises using edge physics codes such as SOLPS [Braams 1987], UEDGE [Rognlien 1994], and DIVIMP [Krieger 1995]. Initial efforts are described at the end of this section.

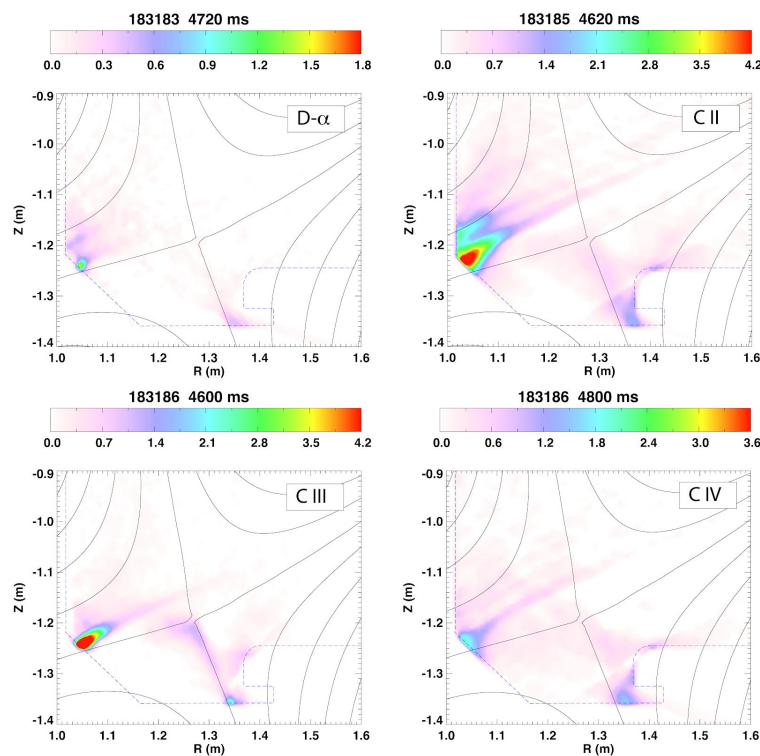


Figure.3.3.Reconstructed visible emissivities (D- α , C III, C II, C IV) from TangTV cameras overlaid to EFIT01 equilibrium reconstruction (uncalibrated units).

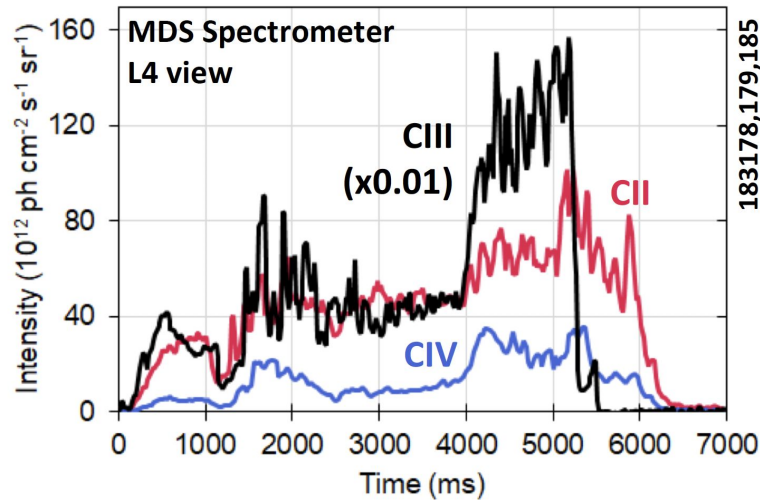


Figure 3.4: Line integrated brightness for C II, C III and C IV as measured by the MDS spectrometer in repeated discharges. Note that the OSP sweep occurred from 4000-5000ms corresponding to the abrupt change in emission.

Evaluation of Impurity Confinement Times

Comprehensive analysis of the JRT datasets will include analysis of the inferred experimental impurity transport using codes such as STRAHL to determine impurity diffusion and convection in the core/pedestal, as well as comparison of measurements with SOL and divertor codes such as UEDGE/SOLPS. This analysis is out of the scope of this supplemental but is planned in future analysis of the JRT datasets. However, a “first cut” into the impurity transport in this discharge can be obtained by a comparison of the measured impurity confinement times for each of the introduced impurities. A preliminary look at impurity transport is provided by fitting an exponential to the decay of the brightness data obtained from measurements such as VUV line emission (SPRED) or via charge exchange. In Figure 3.5. we plot the impurity confinement times obtained from introduction of Li, Al, Ca, and W into the target plasma conditions, using repeat discharges. It should be noted that the Li was introduced via the impurity powder dropper, while the other impurities were introduced via laser blow-off injection. Despite the wide range of Z studied here ($Z=3$ to $Z=74$), the impurity confinement times obtained via this analysis show very similar impurity confinement times as a function of Z. As neoclassical transport might be expected to exhibit a strong Z dependence, this observation suggests it does not play a dominant role in setting the impurity transport in this discharge. However, this is preliminary analysis and it is important to note that more detailed analysis is required to confirm this statement and to investigate how much the impurity confinement times are affected when analyzing ELM-suppressed versus small ELM periods of the discharge. The evaluation of impurity confinements is a crude 0-D estimate of the transport. A detailed description of the future analysis can be found in Sec 4.

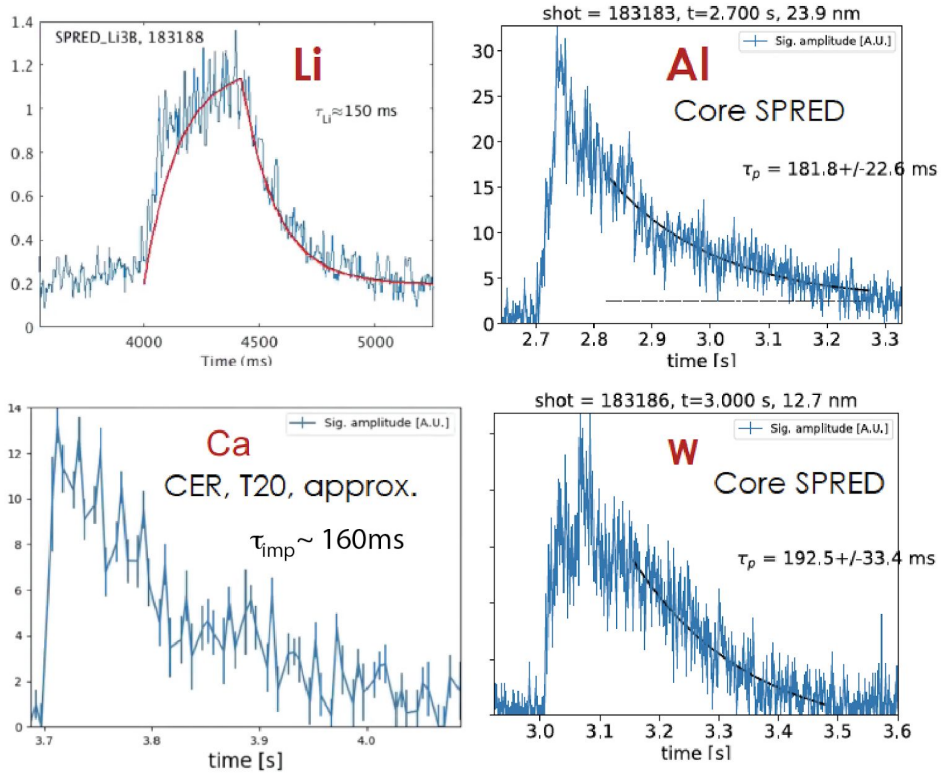


Figure 3.5. Impurity confinement times measured for Li, Al, Ca, and W are shown.

Linear CGYRO Simulations

Using the power balance analysis presented in Section 2 (TRANSP run 183185A02), linear and nonlinear gyrokinetic simulations were performed using the CGYRO code [Candy 2016] across the core profile of the target discharge. These simulations begin to provide some insight into the nature of the turbulence and transport that may be present in the plasma core and represent a starting point for future analysis. Linear CGYRO simulations were performed at $\rho = 0.4, 0.6,$ and 0.8 that span from $k_{\theta}\rho_s = 0.1$ through the electron scales ($k_{\theta}\rho_s > 20.0$). All of these simulations include 3 gyrokinetic species, capture electro-magnetic fluctuations, and use the Sugama collision operator, experimental profiles, and realistic plasma geometry. The results from these linear stability analyses are plotted in Figure 3.6. The general observations from these simulations are that ion temperature gradient turbulence is the dominant instability at long wavelengths with high-k TEM and ETG unstable at shorter wavelengths ($k_{\theta}\rho_s > 1.0$). At the innermost radii the turbulence is found to be weakly unstable at both the ion and electron scales, consistent with the generally smaller driving gradients in this region. Traditionally this region would exhibit smaller impurity diffusion and convection as result of the weaker long wavelength, ITG turbulence but this will be investigated further in future analysis.

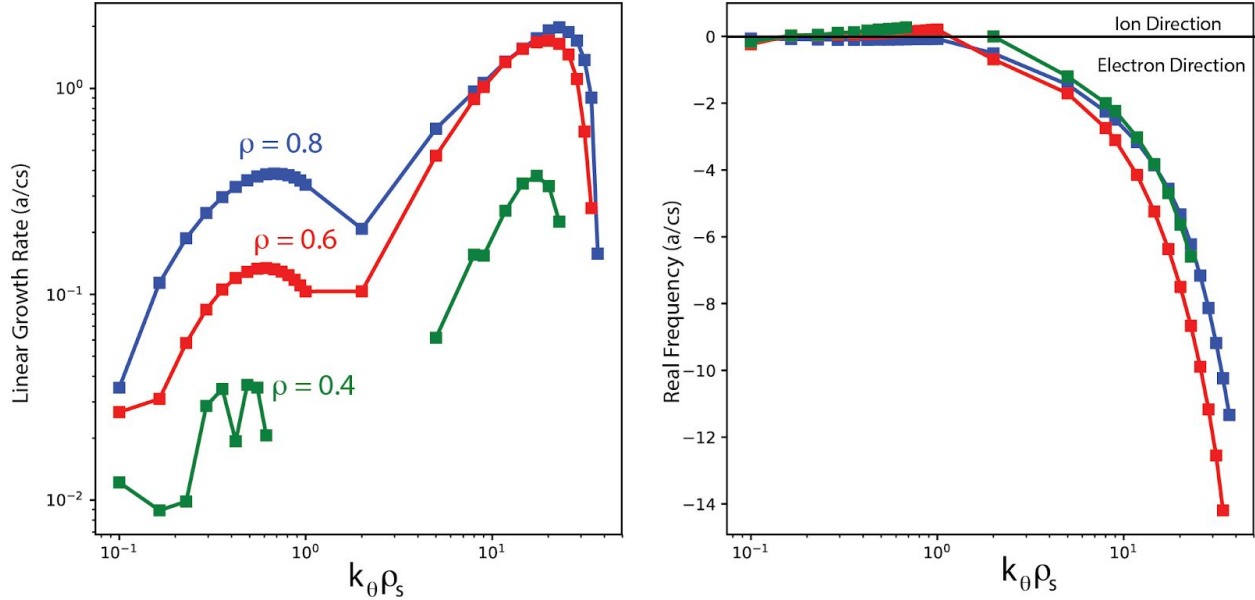


Figure 3.6. Linear growth rates (left) and real frequencies (right) at 3 radial locations, $\rho = 0.4, 0.6, 0.8$ spanning low and high- k . Missing values indicate modes that were found to be stable.

At $\rho = 0.6$ and 0.8 , with no modification to the experimental profiles, the linear growth modes are robustly unstable. Long wavelength ITG dominates at low- k at $\rho = 0.6$ which would generally be linked to larger impurity diffusion and inward impurity convection in this region. In contrast, the low- k turbulence at $\rho = 0.8$ is dominated by trapped electron modes, which have little response to ITG drives but respond strongly to changes in a/L_{Te} . Interestingly the ratio of the maximum high to low- k linear growth rates is highest in the $\rho = 0.6$ radial location, which suggests that multi-scale interactions are most likely to play a role in this region. However, it should be noted that this ratio would still be considered rather low ($\max \gamma_{\text{high-}k} / \max \gamma_{\text{low-}k} \sim 20.0$) and therefore multi-scale turbulence may play only a marginal role [Howard 2016] [Creely 2019]. The general observation from these results is that ITG turbulence will play the major role in setting heat and particle transport in this plasma and the transport in the confinement region while TEM will play a more dominant role in the near-edge. It is notable that the electron and ion power flows from TRANSP at $\rho = 0.6$ indicate $Q_e/Q_i \sim 1.0$, whereas Q_e/Q_i begins to significantly exceed 1.0 near the edge, as ITG turbulence often drives similar levels of heat fluxes in the ion and electron channels, whereas TEM more commonly drives more electron than ion heat flux. A more detailed look at the predicted heat fluxes is covered in the next section describing nonlinear simulation.

Nonlinear CGYRO Simulations

While linear simulation can provide insight into what modes are unstable in the plasma, to study the saturated turbulence state and the resulting transport, nonlinear simulations are required. To probe the transport in these discharges and provide an initial comparison with experimental heat fluxes, 3 nonlinear CGYRO simulations were performed at $\rho = 0.4, 0.6, 0.8$. These simulations have not been run in a manner that examines the sensitivity of results within experimental

uncertainties and therefore do not represent a rigorous validation effort, as such activities will be left to future work. Instead, these simulations provide a “first look” at the transport predicted by high fidelity ion-scale simulations. These runs capture the ion and electron heat transport generated by long wavelength turbulence (up to $k_{\theta}\rho_s \sim 1.1$) in this plasma condition. Each simulation was run with 3 gyrokinetic species (D, C, and e-), electro-magnetic turbulence ($\delta\Phi$ and δA_{\parallel}) rotation effects (ExB shear, etc.), Sugama collisions, all experimental input profiles, and realistic geometry. Each simulation domain was performed with $\sim 100 \times 100\rho_s$ simulation domains represented by 18 toroidal modes and 400 radial modes, more than capable of properly resolving long wavelength turbulence that are typically found, and exhibit correlation lengths of $5-10\rho_s$. Figure 3.7 demonstrates results from these 3 preliminary nonlinear simulations. All simulations were averaged for 200 - 400 a/c_s . Although these are not particularly long time averages for a nonlinear simulation, they average over a large enough number of turbulence decorrelation times, to enable relatively accurate time averages of the simulated heat fluxes. It should be noted that these simulations were started up with ExB shear disabled. After the simulation had started to reach a saturated state, the ExB shear was enabled. Averages are only performed after the simulation has settled following the ExB shear being enabled.

The simulated heat fluxes are compared directly with the experimental values in Figure 3.7. We can see that there is not a very consistent picture from these simulations. At $\rho = 0.4$, the ion heat flux underestimates the power balance value with an even more significant underprediction of the electron heat flux. At $\rho = 0.6$ and 0.8 the simulated ion heat fluxes significantly exceed the experimental values. It is notable that the electron to ion heat fluxes ratios, particularly at $\rho = 0.4$ and 0.8 differ significantly from the power balance values. Despite these disagreements, the stiff nature of core turbulence likely means these fairly large disagreements are easily resolved within experimental uncertainties in the input profiles. A more comprehensive analysis will need to use nonlinear simulation to probe within uncertainties to determine if simulated and experimental heat fluxes can agree within uncertainties.

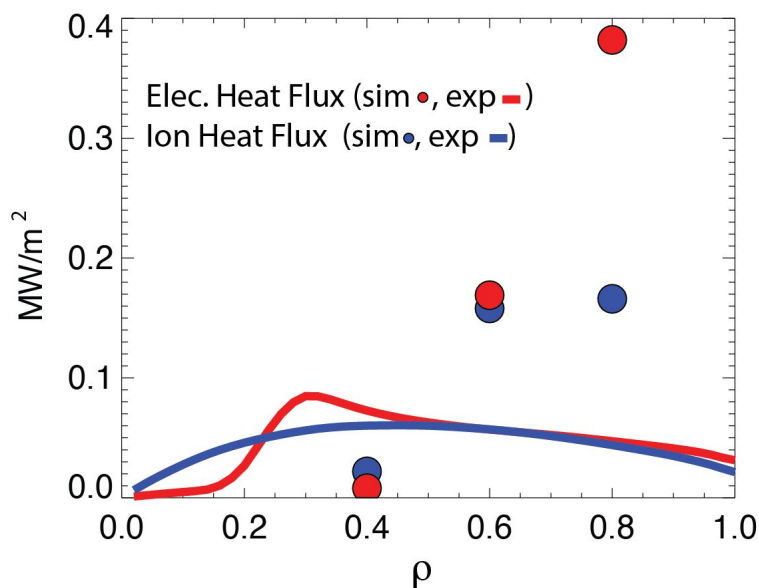


Figure 3.7 The ion and electron heat fluxes from nonlinear simulation are compared with experimental values

TGYRO Prediction of Experimental Profiles Based on TGLF+NEO

Integrated, self-consistent quasilinear transport simulations were performed within GACODE's transport solver TGYRO [Candy 2009]. Unlike in the nonlinear CGYROs described above, this workflow iteratively adjusts local normalized inverse scale lengths, reconstructs profiles, and re-evaluates the ion-electron energy exchange flux to arrive at a self-consistent prediction of plasma profiles that matches the input powers. For this study, we are using NEO [Belli 2008] for the neoclassical flux and electrostatic (due to low β_e) quasilinear TGLF [Staebler 2007] with **E×B** quench rule for the turbulent transport model. Three sets of simulations have been performed at seven flux tubes from $\rho=0.2-0.8$, solving for the heat transport channels first, and then adding particle and momentum transport. The reason for this approach is that the dominant ion and electron heat channels are on the diagonal of the transport matrix and the ion and electron profile scale length produce the fundamental instabilities (ITG, TEM, ETG) that drive significant off-diagonal fluxes in particles and momentum.

Shown in Figure 3.8 are the results of the three simulations. When solving for only thermal energy transport (Q_e, Q_i), we find that the temperatures are generally over-predicted, and especially for the ions. When temperatures separate in low density plasmas, ITG becomes stabilized and the process bootstraps up to form an ion ITB. The same process observed experimentally also occurs in iterative simulations here as well. Adding the particle transport channel can reduce this temperature overshoot effect producing modest increases in a/L_{ne} , bringing the profiles into good agreement with relatively minor adjustments of the electron density scale length. However, improved agreement in the deep core is challenged by the need for a significant increase in the flux-matching ion temperature gradient at larger radii that is likely outside of error bars given the high quality of the data. While the central electron density appears over-predicted and can impact the evaluation of the impurity transport, at this time, density profiles measured by Thomson are undergoing recalibration. Changes associated with recalibration of Thomson data will be integrated into future analysis to determine whether TGYRO continues to over-predict the electron density within measurement uncertainties.. Solving for the momentum transport in this case has a relatively minor effect on the profiles when using the quench rule in a condition with near unity Prandtl number ($\chi_e/\chi_i \sim 0.5-1.5$ from TRANSP). Overall, TGLF is able to broadly capture the observed plasma transport, and exploration of more subtle considerations will be explored in future work.

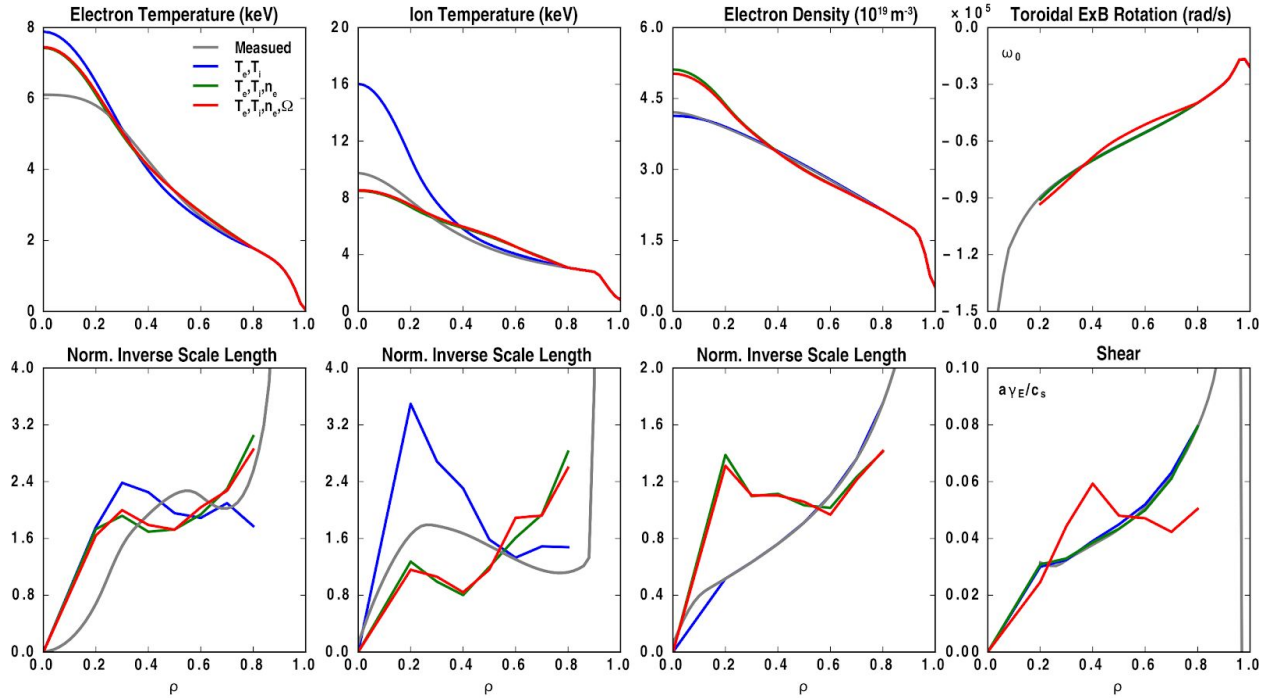


Figure 3.8: Measured profiles and three TGYRO (TGLF+NEO) simulations of flux-matching scale lengths and profiles achieved by simulating (T_e+T_i) , $(T_e+T_i+n_e)$ and $(T_e+T_i+n_e+\omega_\theta)$.

Having matched the power, particle, and momentum fluxes from TRANSP, the final step in profile prediction is to evaluate the intrinsic impurity density profile by determining the zero-flux ($\Gamma=0$) normalized inverse scale length (a/L_{nC}) at each radius, and then integrating inwards from the experimental boundary condition. Here the assumption is that the impurity density does not have a core source (as carbon is fully stripped) and not evolving ($d/dt=0$) which creates a zero-flux constraint. The results of this procedure are shown in Figure 3.9. Here we compare the experimentally measured carbon density profile (with data and uncertainties indicated Figure 2.2) to the predicted carbon density profile. Overall the agreement is quite good and the predicted carbon density profile is quite flat, as observed. It is noteworthy that the measured and predicted carbon density profile is significantly flatter than the electron density profile, which indicates that diffusion is large compared to any impurity pinch. Peaked electron and main-ion density profiles in the presence of a flat impurity density profile is favorable for high fusion performance, and continued validation of transport models in these conditions is essential to understand the balance of diffusion and pinch.

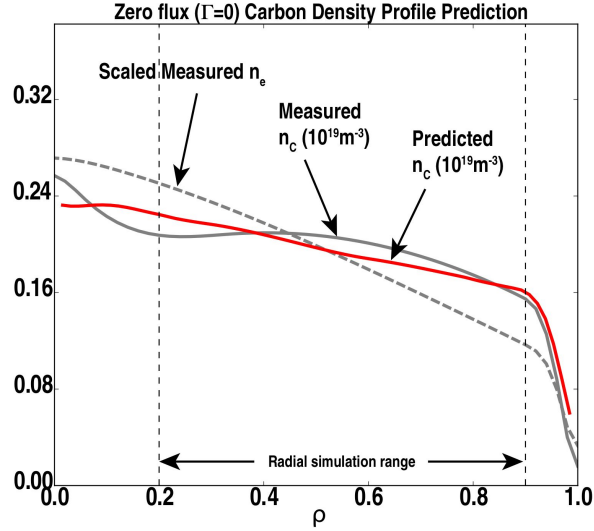


Figure 3.9: Simulation of the stationary source-free intrinsic carbon density profile using the power, particle and momentum flux-matched profiles in Figure 3.8. The scaled electron density profile is included in the figure to assess the relative peaking of the electron and impurity density profiles.

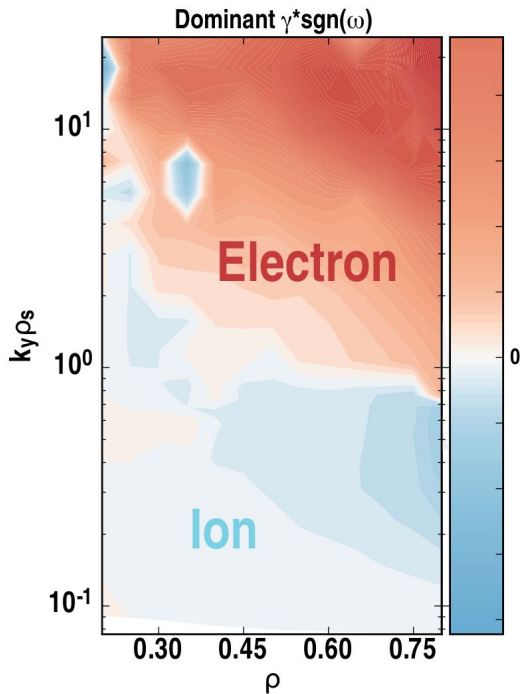


Figure 3.10: Dominant turbulence instability associated with flux-matched simulations shown in Figure 3.8 as a function of radius and wavenumber determined by TGLF

With flux matched simulations completed, the fundamental linear instabilities that underlie the quasilinear transport fluxes are investigated to gain insight into the nature of the modes, shown in Figure 3.10, that produce the turbulent transport. TGLF eigenvalues and quasilinear fluxes near $\rho=0.7$ indicate that the conditions achieved possess three turbulent instabilities. In the low wavenumbers ($k_y \rho_s \sim 0.1-1.0$) ITG modes that produce outward ion and electron energy, particle and momentum fluxes are dominant. There is a band of intermediate wavenumber modes ($k_y \rho_s \sim 1.0-3.0$) that produce both energy and particle flux that may be temperature gradient driven TEMs. TEMs produce both outward electron thermal flux, and inward electron particle flux. In the higher wavenumbers ($k_y \rho_s > 3.0$) TGLF indicates that ETG modes are present that produce solely electron energy flux. These instability hallmarks from TGLF simulations are to be compared with higher fidelity gyrokinetic simulations for confidence in the conclusions from the modeling.

UEDGE Simulation Progress

2D edge fluid transport simulations were started with the multi-fluid edge transport code UEDGE [Rognlien 1994] to study parallel impurity transport and to connect impurity content in the confined plasma with divertor and wall sources. A simulation grid based on EFIT01 equilibrium reconstruction for discharge 183185 at $t=4800\text{ms}$ was generated covering normalized poloidal flux $\psi_N=[0.9-1.06]$. Simulations are underway with the charge state resolved impurity model and inclusion of cross field drifts. Core boundary conditions and radially-varying transport coefficients are being adjusted to provide a match to experimental parameters and upstream plasma profiles. Once a solution consistent with experimental conditions is obtained, divertor impurity sources will be more closely constrained by carbon spectroscopic measurements from TangTV and the MDS spectrometer.

Section 4. Summary and Future Work

Summary

In the previous sections, we provided a description of the experiments performed for the FY20 JRT and the current state of analysis of the data collected. These experiments were performed with the primary goal of simultaneously documenting impurity transport spanning from the core to the edge using repeat discharges on DIII-D. Although data were only collected in one of the desired conditions (ISS with RMP ELM suppression and ECH), the dataset gathered likely represents the most comprehensive impurity transport data collected to date. A wide range of impurities (He to W) were measured in steady discharge conditions and are complimented by a range of other measurements that will enable validation of core and edge impurity transport models, as well as the eventual coupling of core and edge analyses. In the divertor region, absolutely calibrated visible emission from different carbon charge states was measured by the TangTV cameras and the MDS spectrometer. Divertor spectroscopy together with divertor profiles from Langmuir probes and infrared thermography will be used to constrain 2D edge fluid simulations.

The analysis presented here focuses on a well documented discharge 183185. Analysis of the kinetic profiles was described in details along with evaluation and refinement of the plasma equilibrium. This enabled reliable power balance analysis using the TRANSP code [TRANSP], which in turn opened the door for more advanced modeling. A quick evaluation of the scale lengths obtained from the kinetic profile measurements suggests that ITG, TEM, and ETG instabilities may be marginally stable across a large portion of the profile (outside of $\rho = 0.3$). The power flows calculated via power balance suggest that approximately equal levels of ion and electron heat flux are found from $\rho = 0.3$ to 0.75 with a slightly increased Q_e/Q_i ratio occurring outside of this region. The linear stability was calculated at $\rho = 0.4, 0.6,$ and 0.8 over a range of k that spans ion and electron scales. This analysis suggests that ITG is the dominant instability at 0.4 and 0.6 while TEM may play a more dominant role at $\rho = 0.8$. Although ETG is unstable, simple rule of thumb arguments used to estimate the role of multi-scale turbulence,

suggest its role is likely small in the regions investigated. These observations are largely consistent with a naive interpretation of the power balance heat fluxes where ITG would likely drive similar levels of ion and electron heat flux while TEM may drive high Q_e/Q_i ratios.

Three nonlinear CGYRO [Candy 2016] simulations were performed to further investigate the transport in these discharges. These discharges demonstrate that without any modification to the input profiles, the heat fluxes from simulation are within a factor of $\sim 2-4$ of experiment. Such disagreements will likely be resolved within experimental uncertainties in the input profiles but this will be the subject of future work. Unlike the CGYRO simulations which were performed using only the experimental values of the input profiles, the TGYRO code [Candy 2009] was used to self consistently evolve the profiles to match the fluxes found in experiment. This analysis was done using TGLF [Staebler 2007] as the turbulence model and NEO [Belli 2008] to calculate neoclassical contributions. It was found that when all channels are evolved self consistently (T_e , T_i , n_e , and rotation), the profiles predicted by TGYRO are in broad agreement with those measured experimentally. It was noted that some density profile discrepancy in the deep core may be the result of missing Thomson data. This possibility will be the source of future work. From the flux matched profiles, zero-impurity-flux profiles were calculated across the radius to provide a prediction of the steady state carbon profiles in the discharge conditions. These predicted carbon profiles are also found to be in relatively good agreement with those measured via CER with a relatively flat carbon profile observed. It is noteworthy that the measured and predicted carbon density profile is significantly flatter than the electron density profile, which indicates that diffusion is large compared to any impurity pinch. Peaked electron and main-ion density profiles in the presence of a flat impurity density profile is favorable for high fusion performance.

Future work

This document presents the current state of the analysis of the JRT experiments. Additional analysis is planned that will be presented at upcoming conferences, including a post-deadline oral presentation at the 2021 IAEA-FEC, and in subsequent publications. As a first step, calibrated Thomson scattering density data will be added to the analysis presented here to improve the density profile measurements presented. At the time of writing this data had just become available. The impact of this new data will be assessed and propagated through the power balance and modeling analysis. Additional impurity transport analysis is also planned. The Bayesian impurity transport inference framework described in the JRT will be applied to analyze impurity transport data obtained in these experiments. This should allow for the determination of the experimental impurity transport coefficients D and V from the measured VUV, SXR, and CER data, along with an estimate of their uncertainties.

Inferred experimental values of these transport coefficients will be compared with cutting edge, neoclassical, gyro-fluid, and gyrokinetic modeling as part of ongoing work. The codes NEO, TGLF and CGYRO will be used to calculate impurity transport coefficients that can be compared directly with inferred values. This will serve two purposes 1.) enable a comparison of the fully gyrokinetic impurity transport with the reduced model implemented in TGLF and 2.) represent an important validation of the impurity transport models believed to be able to accurately model

core transport. This exercise will be completed along with a rigorous comparison with fluctuation measurements, as well as inferred heat and particles fluxes, representing a comprehensive multi-channel validation of transport models. In the edge and divertor region, codes such as UEDGE [Rognlien 1994] /SOLPS [Braams 1987] will leverage the 2-D Thomson data and spectroscopic measurements and probe data to validate models in this region of the plasma cross-section. Successful validation exercises in these distinct plasma regions will enable the longer term goal of coupling edge impurity transport models with core codes to provide a holistic picture of core to edge impurity transport, with the ultimate aim of predictive capabilities.

References:

[Belli 2008] E.A. Belli and J. Candy “Kinetic calculation of neoclassical transport including self-consistent electron and impurity dynamics”, Plasma Physics and Controlled Fusion 50 (9), 095010 (2008)

[Braams 1987] B.J. Braams “A multi-fluid code for simulation of the edge plasma in tokamaks” Technical report, FOM Instituut voor Plasmafysica, Postbus 1207, 3430 BE Nieuwegein, The Netherlands (1987)

[Candy 2016] J. Candy *et al.* “A high-accuracy Eulerian gyrokinetic solver for collisional plasmas”, Journal of Computational Physics 324, 73-93 (2016)

[Candy 2009] J. Candy *et al.* “Tokamak profile prediction using direct gyrokinetic and neoclassical simulation”, Physics of Plasmas 16 (60), 060704 (2009)

[Creely 2019] A. Creely *et al.* “Criteria for the importance of multi-scale interactions in turbulent transport simulations” Plasma Physics and Controlled Fusion 62 (8), 085022 (2019)

[Howard 2016] N.T Howard *et al.* “Multi-scale gyrokinetic simulations: Comparison with experiment and implications for predicting turbulence and transport”, Physics of Plasmas 23 (5), 056109 (2016)

[Krieger 1995] K. Krieger *et al.* “Modelling of impurities in the ASDEX-Upgrade divertor with DIVIMP “ Journal of Nuclear Materials, 221: 548 (1995)

[Pankin 2004] A. Pankin *et al.* “The tokamak Monte Carlo fast ion module NUBEAM in the National Transport Code Collaboration library “ Computer Physics Communications 159, (3) 157 (2004)

[Rognlien 1994] T.D. Rognlien *et al.* “2-D fluid transport simulations of gaseous/radiative divertors” *Contr. To Plasma Physics* 34, 362-367 (1994)

[Sauter 1999] O.Sauter and C.Angioni, “Neoclassical conductivity and bootstrap current formulas for general axisymmetric equilibria and arbitrary collisionality regime” *Phys of Plasmas* 6(7), 2834 (1999)

[Staebler 2007] G.M. Staebler *et al.* “A theory-based transport model with comprehensive physics”, *Physics of Plasmas* 14(5), 055909 (2007)

[TRANSP] J. Breslau, M. Gorelenkova, F. Poli, J. Sachdev, and X. Yuan. TRANSP. Computer Software. USDOE Office of Science (SC), Fusion Energy Sciences (FES) (SC-24). 27 Jun. 2018. Web. doi:10.11578/dc.20180627.4.

Acknowledgements

This material is based upon work supported by the U.S. Department of Energy, Office of Science, Office of Fusion Energy Sciences, using the DIII-D National Fusion Facility, a DOE Office of Science user facility, under Award DE-FC02-04ER54698. Additional work was supported under DOE grants DE-SC0014264, DE-AC05-00OR22725, DE-SC0019256, DE-SC0017992 . Portions of this research were performed under the auspices of the US DOE by Lawrence Livermore National Laboratory under Contract DE-AC52-07NA27344. This research used resources of the National Energy Research Scientific Computing Center (NERSC), a U.S. Department of Energy Office of Science User Facility operated under Contract No. DE-AC02-05CH11231. Part of the data analysis was performed using the OMFIT integrated modeling framework, O. Meneghini, *et. al.*, “Integrated modeling applications for tokamak experiments with OMFIT”, *Nucl. Fusion* 55, 083008, 2015.

Disclaimer

This report was prepared as an account of work sponsored by an agency of the United States Government. Neither the United States Government nor any agency thereof, nor any of their employees, makes any warranty, express or implied, or assumes any legal liability or responsibility for the accuracy, completeness, or usefulness of any information, apparatus, product, or process disclosed, or represents that its use would not infringe privately owned rights. Reference herein to any specific commercial product, process, or service by trade name, trademark, manufacturer, or otherwise does not necessarily constitute or imply its endorsement, recommendation, or favoring by the United States Government or any agency thereof. The views and opinions of authors expressed herein do